

Development of Iron-based Compounds as Effective Catalysts for Lactide Polymerization and Redox-regulated Molecular Tweezers

by

© FATMA TAKFA

A thesis submitted to the School of Graduate Studies in partial fulfilment of
the requirements for the degree of
MSc

Department of Chemistry
Memorial University of Newfoundland

December 2024

St. John's

Newfoundland

Abstract

This Master's thesis encompasses two distinct research projects in the field of organoiron chemistry. The first project focuses on addressing the global plastic waste problem through the synthesis of biodegradable polymers using non-toxic, abundant metals. Four iron complexes with tetradentate substituted-amino-bis(phenolato) ligands were prepared and characterized. These complexes were studied for their catalytic activities in the ring-opening polymerization (ROP) of *rac*-lactide under various conditions, including catalyst loading, temperature, co-catalysts, and initiators. The complexes demonstrated moderate to good activity for ROP of *rac*-lactide, with controlled and living polymerizations observed in the presence of propylene oxide. The resulting polymer products were characterized by gel permeation chromatographic, MALDI-TOF MS, and thermal analyses to evaluate their quality. Moreover, the kinetic behavior of the polymerization reactions catalyzed by the iron complexes was investigated. The experimental results showed that the type of iron complex has potential in the production of polylactides.

The second project involves the design and synthesis of a novel class of redox-active molecular triads. These systems consist of two electron-donating dithiafulvene (DTF) groups connected to a central ferrocene (Fc) hinge unit via phenylene linkers. Three structural isomers of the (DTF)₂-Fc system were synthesized using Suzuki-Miyaura cross-coupling and phosphite-promoted olefination reactions. The compounds' molecular and solid-state properties were investigated through X-ray single-crystal crystallography, while their electronic and electrochemical properties were examined using UV-Vis spectroscopy and cyclic voltammetry. The studies

revealed multi-stage redox activities influenced by substitution patterns and steric factors. Density functional theory (DFT) and molecular dynamics (MD) simulations were carried out to provide further insights into the compounds' conformational and electronic properties in various oxidation states. Notably, the *para*-substituted (DTF)₂-Fc exhibited controllable conformational switching through redox reactions and supramolecular interactions with γ -cyclodextrin.

Acknowledgements

First and foremost, I am deeply grateful to my supervisor, Prof. Yuming Zhao, the most humble supervisor I've ever met, for spending time meeting with me and reviewing my poster, presentations, paper, and thesis chapters, and for providing me the opportunity to attend The ISNA conference and to communicate with other scientists and peers. His mentorship has been a cornerstone of my academic and personal growth. I am always indebted to him for everything he has taught me during my Master's program.

I would not have reached this point without the decision of the senate committee which helped me come back to my graduate program. I am so grateful for their insights and support of my case.

I extend my appreciation to my supervisory committee members, Prof. Huck Grover and Prof. Erika Merschrod. Their expertise, feedback, and constructive discussions have greatly enriched the quality of this work.

I want to express my sincere appreciation to Dr. Jian-bin Lin at the C-CART. His expertise and guidance in crystallography have been invaluable in enhancing the quality of this research.

My heartfelt appreciation goes to my husband, Monther, for his support, encouragement, and insightful discussions. He was my mentor in the lab, teaching me all organic synthesis techniques, spending days and nights in the lab trying to make my time productive, and babysitting our toddler Sally. and with the arrival of our baby boy, Montaser, our hearts have been filled with more joy than we ever imagined. Without him, this journey would never be possible. To my family in Gaza,

Dad, Mom, and my siblings, who were always supporting me even at the time of war. They are the real meaning of strength and persistence.

I extend my gratitude to my colleagues, Fatemeh Salami and Liam Britt, as well as all organic graduate students in the office. Their camaraderie and collaboration have enriched my research experience.

I sincerely acknowledge the support of Memorial University of Newfoundland, NSERC, and Compute Canada for funding this research, enabling me to pursue my academic aspirations.

Lastly, to everyone who played a role, big or small, in my academic and personal journey, their contributions are cherished and appreciated beyond words. Thank you.

Contents

Abstract	ii
Acknowledgements	iv
List of Figures	ix
List of Schemes	xvi
List of Tables	xvii
List of Abbreviations and Symbols	xviii
1 Introduction	1
1.1 Introduction to Iron Chemistry	1
1.2 Lactide and Polylactic Acid	3
1.3 Stereoselectivity in the ROP of Lactide	7
1.4 Physical Properties of Polylactide	8
1.5 Metal Complexes for Lactide Polymerization	10
1.6 Iron(III) Catalyzed Polymerization Reactions	12
1.7 Objectives of this Thesis	14

2	Iron Amino-bis(phenolate) Complexes for Lactide Polymerization	21
2.1	Introduction	21
2.2	Synthesis of Tetradentate Amino-bis(phenolate) Ligands	24
2.3	Synthesis of Iron(III) Amino-bis(phenolate) Complexes	26
2.4	Characterization	26
2.4.1	Computational Modeling of 1a–d	27
2.5	Ring-Opening Polymerization of Lactide under the Catalysis of Iron Amino-Bis(phenolate) Complexes	28
2.5.1	Results of Polymerization and Kinetic Studies	30
2.6	Characterizations of the polymer products	34
2.6.1	NMR Spectroscopic Analysis	34
2.6.2	Gel Permeation Chromatographic Analysis	34
2.6.3	MALDI-TOF MS Analysis	35
2.6.4	Differential Scanning Calorimetric Analysis	36
2.6.5	Homonuclear decoupled ¹ H NMR Analysis	38
2.7	Conclusion	39
2.8	Experimental Section	40
2.8.1	Materials	40
2.8.2	Experimental Methods	40
3	Phenyldithiafulvene-substituted Ferrocene Derivatives as Redox- regulated Molecular Switches	49
3.1	Introduction	50
3.2	Results and Discussion	54

3.2.1	Synthesis of (DTF) ₂ -Fc Compounds	54
3.2.2	Crystallographic Properties of 5a and 5c	56
3.2.3	Conformational Properties of 5a-c	58
3.2.4	Electronic Absorption Properties of 5a-c	66
3.2.5	Electrochemical Redox Properties of 5a-c	67
3.2.6	Supramolecular Interactions of 5a with γ -Cyclodextrin	74
3.3	Conclusions	82
3.3.1	Experimental Section	84
4	Conclusions and Future Work	98
5	Appendixes	102
5.1	Appendix A: Supporting Information for Chapter 2	102
5.2	Appendix B: Supporting Information for Chapter 3	120

List of Figures

1.1	Polymer stereochemistry	5
1.2	Metal complexes used by the Spassky group (1), the Coates group (2), and the Williams group (3) as catalysts for the stereocontrolled synthesis of PLA.	10
1.3	Iron complexes designed by the Byers group for polymerization of lactide.	13
1.4	Iron complexes used by the Lamberti group.	14
2.1	General structure of an amino-bis(phenolate) ligand coordinating with a metal center.	22
2.2	Optimized geometries of complexes 1a–b by DFT calculations.	27
2.3	Atomic charges of Fe and selected bond lengths in 1a–d	28
2.4	Plot of $\ln[\text{LA}]_0/[\text{LA}]_t$ versus time at 22 °C for the ROP of <i>rac</i> -lactide catalyzed by complex 1c ($[\text{LA}]:[\mathbf{1c}] = 100:1$, $[\text{LA}] = 0.133$ g/mL in PO). The dashed lines are the linear regression fits.	32
2.5	Plot of $\ln[\text{LA}]_0/[\text{LA}]_t$ versus time at 80 °C for the ROP of <i>rac</i> -lactide catalyzed by complex 1c ($[\text{LA}]:[\mathbf{1c}] = 100:1$, $[\text{LA}] = 0.133$ g/mL in PO). The dashed lines are the linear regression fits.	32
2.6	Plot of $\ln[\text{LA}]_0/[\text{LA}]_t$ versus time at different catalyst loading.	33

2.7	Plot of the correlation of $\ln(K)$ versus $\ln[\mathbf{1c}]$ for the ROP of <i>rac</i> -lactide catalyzed by complex 1c in PO at 80 °C. The dashed line in the bottom plot is the linear regression fit.	33
2.8	¹ H NMR (300 MHz, CDCl ₃) spectrum of a representative PLA product.	35
2.9	Representative GPC results for the ROP of LA with 1c ($M_w = 5.90$ kDa, $D = 1.06$).	36
2.10	MALDI-TOF MS spectrum of a PLA product (DMPA used as co-catalyst).	37
2.11	DSC thermogram of the PLA obtained under the conditions of entry2, Table 2.1.	37
2.12	[¹ H] ¹ H NMR spectrum of PLA from 1c (80 °C, 4 hours, Et ₃ NH ⁺ Cl ⁻ , PO, $P_r = 0.48$).	38
3.1	Ferrocene-hinged molecular switches containing two redox-active arene side arms as conformational modulators.	51
3.2	(A) ORTEP drawings (at 50% ellipsoid probability) of the molecular structure of 5a viewed from different perspectives. (B) Crystal packing diagram of 5a viewed along the <i>a</i> -axis of the unit cell (hydrogen atoms are omitted for clarity).	56
3.3	(A) ORTEP drawings (at 50% ellipsoid probability) of the molecular structure of 5c viewed from different perspectives. (B) Crystal packing diagram of 5c viewed along the <i>b</i> -axis of the unit cell (hydrogen atoms are omitted for clarity).	58

3.4	(A) and (B) Plots of optimized geometry of 5a view from different perspectives with selected torsion angles and inter-centroid distances highlighted. (C) NCI analysis of 5a showing the RDG isosurface (isovalue = 0.40 a.u.). (D) Plot of RDG vs $\text{sign}(\lambda_2)\rho$	60
3.5	^1H NMR (300 MHz, DMF- d_6) spectra of 5a showing its phenylene and vinylic proton signals measured at different temperatures.	61
3.6	(A)–(D) Distances between the centroid positions of the two phenylene groups (D_1) and two dithiole groups (D_2) of 5a as a function of MD simulation time at different temperatures. (E) Molecular structure of 5a with the inter-ring distances D_1 and D_2 illustrated. (F) Simulation snapshot of 5a taken at time = 8 ps, temperature = 398 K.	62
3.7	Optimized molecular structures of (A) <i>cis</i> 5b and (B) <i>cis</i> 5c . Inter-centroid distances between adjacent arene rings are highlighted.	63
3.8	^1H NMR (300 MHz, DMF- d_6) spectra of (A) 5b and (B) 5c showing their phenylene and vinylic proton signals measured at different temperatures.	64
3.9	Normalized UV-Vis absorption spectra of 5a–c measured in CH_2Cl_2 at room temperature.	67
3.10	Cyclic voltammograms of (A) 5a , (B) 5b , and (C) 5c measured in DMF at room temperature. Experimental conditions: glassy carbon as the working electrode, Ag/AgCl as the reference electrode, Pt wire as the counter electrode, Bu_4NPF_6 (0.1 M) as the electrolyte, and scan rate = 0.20 V/s.	68

3.11 (A) ESP map of monocationic <i>cis</i> - 5a . (B) Isosurface map of the spin density (0.001 a.u.) distribution of monocationic <i>cis</i> - 5a . (C) Reaction scheme of the single-electron transfer taking place on <i>cis</i> - 5a . Colored text boxes give the total atomic charges (ΣQ) of the central Fc unit and two phenylene-DTF arms, respectively.	69
3.12 (A) ESP map of dicationic <i>cis</i> - 5a and (B) its schematic drawing of charge distribution in the singlet ($S = 1$) state. (C) ESP map of dicationic <i>cis</i> - 5a and (D) its schematic drawing of charge distribution in the triplet ($S = 3$) state. Colored text boxes give the total atomic charges (ΣQ) of the central Fc unit and two phenylene-DTF arms, respectively.	71
3.13 Isosurface map of the spin density (0.001 a.u.) distribution of <i>cis</i> dicationic 5a ($S = 3$).	71
3.14 ESP maps of (A) <i>cis</i> tricationic 5a ($S = 2$) and (B) <i>trans</i> tricationic 5a ($S = 4$). Isosurface maps of the spin density (0.001 a.u.) distribution of (C) <i>cis</i> tricationic 5a ($S = 2$) and (D) <i>trans</i> tricationic 5a ($S = 4$).	72
3.15 Proposed binding modes between 5a and γ -CD.	75
3.16 (A) Expanded ^1H NMR (300 MHz, $\text{DMSO-}d_6$) spectra of 5a and a mixture of 5a and γ -CD at 1:1 mole ratio. (B) MALDI-TOF mass spectrum measured from a mixture of 5a and γ -CD. Mass peaks assigned to the molecular ions due to the 1:1 complex of 5a and γ -CD are highlighted by red and cyan colors.	77

3.17	(A) RMSD plots of the 1:1 complexes of 5a and γ -CD in DMF at 298 K. Snapshots taken during the MD simulations of the complexes in the (B) Fc-inclusion mode and (C) DTF-inclusion mode.	80
3.18	(A) Multi-cycle CV scans of 5a in DMF. (B) Cyclic voltammograms monitoring the titration of 5a (0.10 mM) with γ -CD (from 0 to 4.0 mole equiv) in DMF. (C) Current responses of the cathodic peak at +0.61 V (vs Ag/AgCl) to the addition of CD. I_0 and I are the current intensities before and during the titration. (D) Formation of a 2:1 complex of γ -CD and 5a under oxidative conditions. (E) MALDI-TOF mass spectrum showing the molecular ion of the 2:1 complex of γ -CD and 5a (highlighted by red color).	82
5.1	^1H NMR (300 MHz) spectrum of $\text{H}_2\text{L}_1\text{a}$ in CDCl_3	103
5.2	^1H NMR (300 MHz) spectrum of $\text{H}_2\text{L}_1\text{b}$ in CDCl_3	104
5.3	^1H NMR (300 MHz) spectrum of $\text{H}_2\text{L}_1\text{c}$ in CDCl_3	105
5.4	^1H NMR (300 MHz) spectrum of $\text{H}_2\text{L}_1\text{d}$ in CDCl_3	106
5.5	MALDI-TOF mass spectrum (negative mode) of complex 1a showing experimental (a) and theoretical isotopic distribution patterns.	107
5.6	MALDI-TOF mass spectrum (negative mode) of complex 1b	108
5.7	MALDI-TOF mas spectrum (negative mode) of complex 1c showing experimental (a) and theoretical isotopic(b) distribution patterns.	109
5.8	MALDI- TOF spectrum in negative mode of complex 1d	110

5.9	MALDI-TOF mass spectrum (negative mode) of complex 1c with PPnCl in PO showing the formation of alkoxide species at $m/z = 606.1$	111
5.10	MALDI-TOF mass spectrum of PLA derived (CHO used as initiator and solvent).	112
5.11	MALDI-TOF mass spectrum of PLA derived (DMAP used as co-catalyst).	113
5.12	MALDI-TOF mass spectrum of PLA derived (with no co-catalyst used).	114
5.13	^1H NMR (300 MHz) spectrum of crude polymer(PLA, CDCl_3).	115
5.14	^1H NMR (300 MHz) spectrum of PLA from complex 1c (80 °C, 4 hours, $\text{Et}_3\text{NH}^+\text{Cl}^-$, PO, $P_r = 0.48$).	115
5.15	^1H NMR (300 MHz) spectrum of complex 1c for LA polymerization (at 22 °C, $t = 0\text{--}25\text{h}$).	116
5.16	Representative GPC for ROP of LA with complex 1c ($M_w = 6.30$ KDa, $D = 1.06$).	117
5.17	Representative GPC for ROP of LA with 1c ($M_w = 5.70$ KDa, $D = 1.08$).	118
5.18	Differential scanning calorimetric thermogram of PLA (entry 7).	119
5.19	^1H NMR (300 MHz) spectrum of 3a in CDCl_3	120
5.20	^{13}C NMR (75 MHz) spectrum of 3a in CDCl_3	121
5.21	^1H NMR (300 MHz) spectrum of 3b in CDCl_3	121
5.22	^{13}C NMR (75 MHz) spectrum of 3b in CDCl_3	122
5.23	^1H NMR (300 MHz) spectrum of 3c in CDCl_3	122
5.24	^{13}C NMR (75 MHz) spectrum of 3c in CDCl_3	123
5.25	^1H NMR (300 MHz) spectrum of 5a in CDCl_3	123

5.26	^{13}C NMR (75 MHz) spectrum of 5a in CDCl_3	124
5.27	^1H NMR (300 MHz) spectrum of 5b in CDCl_3	124
5.28	^{13}C NMR (75 MHz) spectrum of 5b in CDCl_3	125
5.29	^1H NMR (300 MHz) spectrum of 5c in CDCl_3	125
5.30	^{13}C NMR (75 MHz) spectrum of 5c in CDCl_3	126
5.31	^1H NMR (300 MHz, DMSO-d_6) spectrum of a mixture of 6a and β -CD (ca. 1:2 mole ratio) in comparison with those of pure 5a and β -CD.	127
5.32	CV of 5b with CD measured in DMF. Experimental conditions: electrolyte: $n\text{-Bu}_4\text{NBF}_4$, 0.1 M, working electrode: glassy carbon, reference electrode: Ag/AgCl, counter electrode: Pt wire. Scan rate = 200 mV/s.	128
5.33	CV of 5c with CD measured in DMF. Experimental conditions: electrolyte: $n\text{-Bu}_4\text{BF}_4$, 0.1 M, working electrode: glassy carbon, reference electrode: Ag/AgCl, counter electrode: Pt wire. Scan rate = 200 mV/s.	129
5.34	Plots of MOs involved in vertical electronic transitions of <i>para</i> - 5a (isovalue = 0.03 a.u.).	130

List of Schemes

1.1	(A) Production of lactide from biomass. (B) Three isomers of lactide.	3
1.2	Microstructures of PLA obtained from stereocontrolled ROP of (A) L-lactide and D-lactide, (B) meso-lactide, and (C) <i>rac</i> -lactide.	9
1.3	alkoxide metal formation mechanism	13
2.1	Catalytic cycle of iron-oxide promoted PLA synthesis proposed by Shaver <i>et al.</i>	24
2.2	Synthesis of a) amino-bis(phenolate) ligands and b) their complexes with iron(III).	25
2.3	Polymerization of LA to PLA	29
3.1	(A) Interaction of neutral DTF and its radical cation. (B) Reaction of two DTF radical cations to form a tetrathiafulvalene vinylogue (TTFV) product.	53
3.2	Synthetic routes to (DTF) ₂ -Fc 5a-c	55

List of Tables

2.1	Polymerization data of rac-LA with complexes 1a-1d in PO.	31
2.2	The effects of co-catalysts on the tacticity of PLA product, Reaction Parameters:(1% 1c , 1% Co-catalyst, LA = 400 mg, PO = 3ml, t= 4 h, 80 °C)	39
5.1	Summary of Experimental UV-Vis absorption data of 3a-c and 5a-c (measured in CH ₂ Cl ₂)	126
5.2	Summary of TD-DTF results for <i>para</i> - 5a (transitions with $f < 0.001$ are omitted)	129
5.3	Summary of TD-DTF results for <i>meta</i> - 5b transitions with $f < 0.003$ are omitted	130
5.4	Summary of TD-DTF results for <i>ortho</i> - 5c (transitions with $f < 0.0005$ are omitted)	131
5.5	Crystal data and structure refinement for 5a	132
5.6	Crystal data and structure refinement for 5c	133

List of Symbols, Nomenclature and Abbreviations

Å	Angstrom unit (a unit of length, equal to 10^{-10} meters)
aq	aqueous
BPh ₃	Triphenylborane
calcd	calculated
CD	cyclodextrin
CHCl ₃	chloroform
-CHO	aldehyde
cm	centimeter(s)
-CN	nitrile
-COMe	acetyl
-COOH	carboxylic acid

Cat.	catalyst
^{13}C NMR	carbon nuclear magnetic resonance
Conv.	conversion
Co-cat.	co-catalyst
CHO	cyclohexene oxide
CV	cyclic voltammetry
DCTB	<i>Trans</i> -2-[3-(4- <i>tert</i> -butylphenyl)-2-methyl-2-propenylidene] malononitrile
d	doublet (NMR)
D	dextrorotatory
\bar{D}	molecular weight dispersity, = M_w/M_n
DHBA	2,5-dihydroxybenzoic acid
DMAP	4-dimethylaminopyridine
DCM	dichloromethane
DSC	differential scanning calorimetry
DFT	density functional theory
DMF	<i>N,N</i> -dimethylformamide
DMSO	dimethylsulfoxide

DTF	1,4-dithiafulvene
ϵ -CL	ϵ -caprolactone
EDG	electron-donating group
Et	ethyl
EtOH	ethanol
Et ₃ N	triethylamine
EtOAc	ethyl ethanoate (ethyl acetate)
eV	electron volt
FTIR	Fourier transform infrared
Fc	Ferrocene
Fc-DTF	Ferrocene substituted 1,4-dithiafulvene
GPC	gel permeation chromatography
g	gram(s)
¹ H ¹ H NMR	homonuclear decoupled nuclear magnetic resonance
¹ H NMR	proton nuclear magnetic resonance
h	hour(s)
J	Joule(s)

J	coupling constant
in situ	in the reaction mixture
k	rate constant
kHz	kilohertz
kcal mol ⁻¹	kilocalories per mole
k_{obs}	apparent first-order rate constant
L	levorotatory
LA	lactide
LUMO	lowest unoccupied molecular orbital
rac-LA	racemic-lactide
m	multiplet (NMR)
M	molar
m_e	mass of an electron
M_A	mass of the nucleus of atom A
MALDI-TOF	matrix-assisted laser desorption/ionization-time of flight
Me	methyl
mg	milligram(s)

min	minute(s)
mL	milliliter(s)
mmol	millimole(s)
mM	milimolar
M_n	number average molecular weight
M_w	weight average molecular weight
mol	mole(s)
m.p.	melting point
MS	mass spectrometry
mV	millivolt(s)
m/z	mass-to-charge ratio
-NH ₂	amine
nm	nanometer(s)
<i>p</i>	<i>para</i>
<i>o</i>	<i>ortho</i>
<i>m</i>	<i>meta</i>
PCL	poly(caprolactone)

PPNCl	bis(triphenylphosphoranylidene)iminium chloride
PDLA	poly-D-lactide
PLA	polylactide
PLLA	poly-L-lactide
P_m	the probability of isotactic linkages between monomer units
ppm	parts per million
PP_3	Triphenylphosphine
P_r	the probability of racemic linkages between monomer units
-OMe	methoxy
ppm	parts per million
PO	propylene oxide
ROP	ring-opening polymerization
TBAB	tetrabutylammonium bromide
t	tertiary
t	time
t	triplet (NMR)
t Bu	<i>tert</i> -butyl

Temp	temperature
<i>tert</i>	tertiary
T_g	glass transition temperature
TD-DFT	time-dependent density functional theory
TFA	trifluoroacetic acid
THF	tetrahydrofuran
TLC	thin-layer chromatography
TS	transition state
TTF	tetrathiafulvalene
UV	ultraviolet
UV-Vis	ultraviolet-visible
V	volt(s)
VT-NMR	variable temperature proton nuclear magnetic resonance
Vis	visible
v/v	volume-to-volume ratio
XRD	X-ray diffraction
δ	chemical shift
λ_{max}	maximum absorption wavelength

Chapter 1

Introduction

1.1 Introduction to Iron Chemistry

Iron (Fe) is a transition metal (element 26) that abundantly pervades in our everyday lives. As the fourth most-abundant element in Earth's crust, iron constitutes more than 30% of the Earth's mass.^{1,2} In human history, iron has played a critical role in the development of technology and civilization. Between 1200 B.C. and 600 B.C., human history entered into the so-called Iron Age, when the use of iron became widespread after people learned how to prepare steel.¹ In ancient eras, iron was mainly used for making tools and weapons. It was a valuable trade commodity that significantly influenced the power and wealth of nations. In modern days, iron and steel were essential to the Industrial Revolution, facilitating the construction of machinery, ships, railways, buildings, and more.

In the biological world, the role of iron is also highly important. For example, iron is a key component in proteins such as hemoglobin and myoglobin,³ which are

essential for the transport and storage of oxygen in living organisms. Iron-sulfur (Fe-S) clusters are key co-factors that mediate electron transfer within the mitochondrial respiratory chain and play a critical role in the pathogenesis of disease. Iron also acts as a co-factor for many metabolic enzymes in nature.³

Chemically pure iron can be obtained through the reduction of iron oxide with hydrogen.⁴ As a soft silver-white metal, pure iron rusts very quickly when exposed to moisture and air. It therefore has little use in material applications. Addition of carbon and other transition metals into pure iron produces steels with improved hardness, tensile strength, and resistance to wear and corrosion. Iron is also ferromagnetic up to 1041 K.

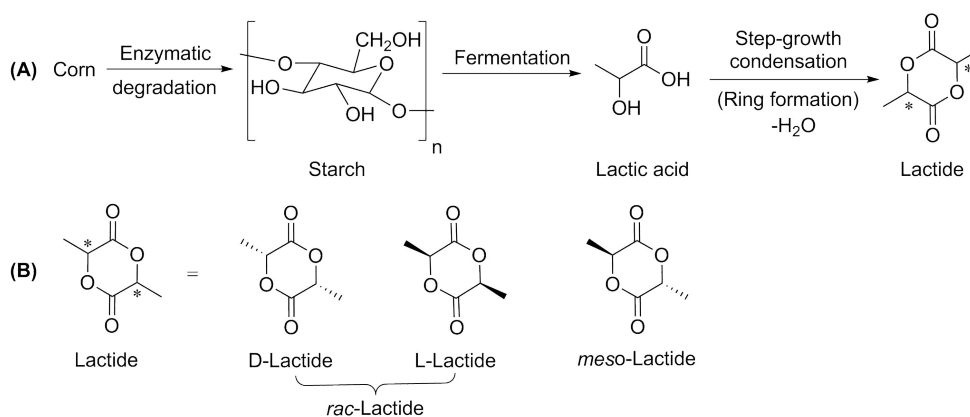
The atom of Fe(0) has an electronic configuration of $[\text{Ar}]3d^64s^2$. The oxidation states of iron range from -2 (d^{10}) to $+6$ (d^0).⁵ Among them, Fe^{2+} and Fe^{3+} are the most common, while iron species in the other oxidation states are also important. Iron in a low-oxidation state is known to show nucleophilicity. In a high-oxidation state, it becomes electrophilic and Lewis acidic.

Iron can form salts and complexes with various anions and ligands. In 1891, ironpentacarbonyl $\text{Fe}(\text{CO})_5$ was discovered independently by Mond⁶ and Berthelot.⁷ later in 1941, $\text{Fe}(\text{CO})_5$ was used for the first time as a catalyst in the Reppe process of hydroformylation of ethylene to produce propionaldehyde and 1-propanol in basic solutions.⁸ Iron oxide was used as a catalyst for the production of ammonia in 1914. In 1951 an important milestone in iron chemistry was made by the discovery of ferrocene,⁹ followed by the preparation of $\text{Na}_2\text{Fe}(\text{CO})_4$ in 1959.¹⁰ In the early 1990s, Fe(II) catalyst precursors, $[(\text{PP}_3)\text{FeH}(\text{N}_2)]\text{BPh}_4$ and $[(\text{PP}_3)\text{FeH}(\text{H}_2)]\text{BPh}_4$, were first used in the reduction of alkenes and alkynes by Bianchini et al.¹¹ Since then, several

impressive achievements have been made, demonstrating increased potential of iron as a catalytic system in reducing organic compounds.

1.2 Lactide and Polylactic Acid

Lactide or 3,6-dimethyl-1,4-dioxane-2,5-dione is the cyclic dimer of lactic acid (LA), which is commonly used as a starting material for the production of polylactic acid (PLA). LA can be prepared from renewable biomass such as corn, sugar and beet through fermentation.¹² As illustrated in Figure 1.1A, enzymatic degradation of starch produces LA, which then undergoes fermentation to yield Lactic acid.^{13,14} Condensation reactions of LA give oligomeric lactic esters, which are subsequently depolymerized through internal transesterification to yield lactide. There are two stereogenic carbon centers in the cyclic ester structure of lactide. Hence, lactide consists of three stereoisomers, namely L-lactide (L-LA), D-lactide (D-LA) and *meso*-lactide (Figure 1.1A).



Scheme 1.1: (A) Production of lactide from biomass. (B) Three isomers of lactide.

PLA has been widely recognized as an eco-efficient and sustainable solution

to the pollution crisis caused by traditional petroleum-based plastics, owing to its biodegradability, renewable origins, and reduced environmental impact.¹⁵ PLA can decompose in industrial composting facilities within a few months, significantly reducing landfill wastes. Furthermore, the production of PLA generates much less greenhouse gases compared to the production of traditional plastics. Upon decomposition, PLA only yields water and CO₂, which can be reused by plants in their photosynthetic processes. These properties align well with the global efforts to combat climate change. In recent years, the market of PLA has grown considerably, driven by government policies, growing awareness and increasing demand from the Asia Pacific region. For example, the global PLA market in 2023 was valued at USD 1.5 billion and is projected to reach USD 3.3 billion by the year of 2028. Commercially produced PLA has already been used in packaging, agriculture and special medical products.

PLA can be generated by two major synthetic routes: direct polycondensation of LA and ring-opening polymerization (ROP) of lactide. Polycondensation of LA needs harsh reaction conditions, such as high temperature and pressure environments, to achieve a high degree of polymerization. The ROP of lactide, however, can readily produce high-molecular mass polylactides with a low degree of molar mass distribution (dispersity) under relatively mild reaction conditions.¹⁶ Several mechanisms have been proposed for the ROP of lactide, including cationic, anionic, and coordination pathways.¹⁷ The cationic mechanism can result in undesirable side reactions or racemization due to possible nucleophilic attack on the activated monomer or growing chains. In the mechanism of anionic ROP, unwanted reactions such as racemization, back-biting, and other side reactions may happen due to the highly reactive anionic

species.¹⁷ Coordination ROP of lactide relies on the use of metal complexes, and the molecular weight and tacticity of the resulting polymers can be much better controlled. It is worth noting that molecular weight and tacticity are two crucial factors for the physical properties of polymers. Tacticity is an important factor that refers to the arrangement of adjacent stereocenters like in lactide, as defined by the Bovey formalization, where "i" denotes iso (same) and "s" denotes syndio (different)(Figure1.1.¹⁸ The relationship between two stereocenters is called a diad, while the relationship among three is termed a triad, and four is referred to as a tetrad, and so forth. The detectability of tacticity in polymers varies depending on their structural characteristics.

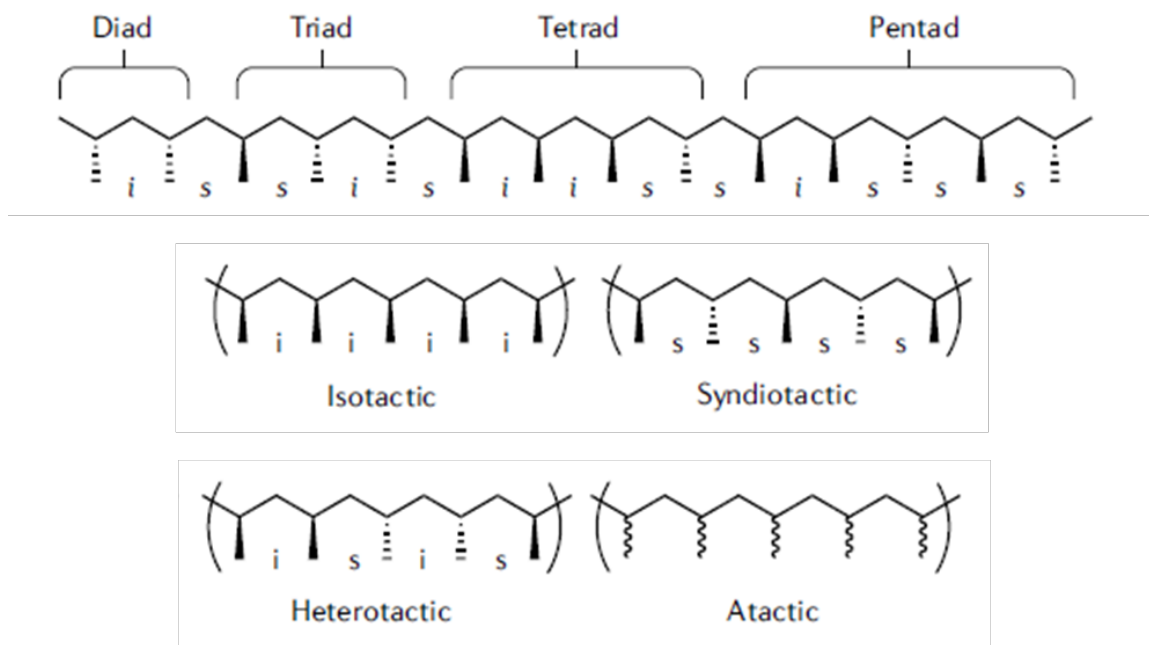


Figure 1.1: Polymer stereochemistry

In industrial production of polylactides, tin(II) bis(2-ethylhexanoate)(Sn(Oct)₂) is used as a standard catalyst.¹⁹ For materials used in food packaging and medical

applications, low- or non-toxicity is a critical requirement for health and food safety. Tin-based catalysts somehow present a negative image in this regard, since they can be easily tied to toxicity without careful consideration. In some literature reports, tin catalysts such as $\text{Sn}(\text{Oct})_2$ were categorized as having toxic or cytotoxic effects without actual toxicity data cited.¹⁵ A recent review by Kricheldorf and Weidner thoroughly discussed the toxicity issues of tin catalysts in comparison with other organic catalysts used for polylactide synthesis.²⁰ It is interesting to learn that tin(II) salts show much lower toxicity than many amine-based catalysts developed for lactide polymerization in recent years. For example, the LD_{50} (canine) of $\text{Sn}(\text{Oct})_2$ is $> 2000 \text{ mg kg}^{-1}$, but for pyridine the value is 1200 mg kg^{-1} . It is therefore important to have detailed toxicity data in hand before claiming a new catalyst(s) as being safe and environmentally friendly. Organotins such as alkyltins are indeed considerably more toxic than tin(II) salts. However, the use of alkyltins as catalysts is rare in industrial synthesis of polylactides.

There are many catalysts other than tin(II)-based compounds that have been investigated for the ROP of lactides. Some of them have shown high performance in terms of polymerization rate, stereo-selectivity and redox control. Unfortunately, up to date none of the new catalysts can serve as viable replacement of tin(II) catalysts in industrial production of PLA.¹⁵

The discussion made above should not be regarded as a reason for stopping the search for alternative catalytic systems to $\text{Sn}(\text{Oct})_2$ for the ROP of lactide. On the contrary, it is still a highly meaningful topic of research. First, the discovery of new catalysts can cast deeper insights into the fundamental reactivity for lactide polymerization and therefore guide better control over the properties of the polymer

product. Second, they may also help to reduce the costs and circumvent some side effects of the current production technologies. These considerations are the main drivers of the first research project conducted in this thesis work. Our development of new catalysts for the ROP of lactide is aimed at catalysts that are biocompatible and highly active under industrial conditions. In particular, the catalysts are desired to induce polymerization under solvent-free conditions with a low catalyst loading. From practical points of view, the catalysts must be air-stable, tolerant to moisture and the small amounts of impurities in technical grade LA. In this regard, iron complexes appear to be ideal candidates for this type of study, owing to the advantageous features of iron briefly reviewed in the previous section. Presently, the studies of iron-based catalysts have been actively carried out in polymer chemistry. The following section describes important advancements in this area made over the past years.

1.3 Stereoselectivity in the ROP of Lactide

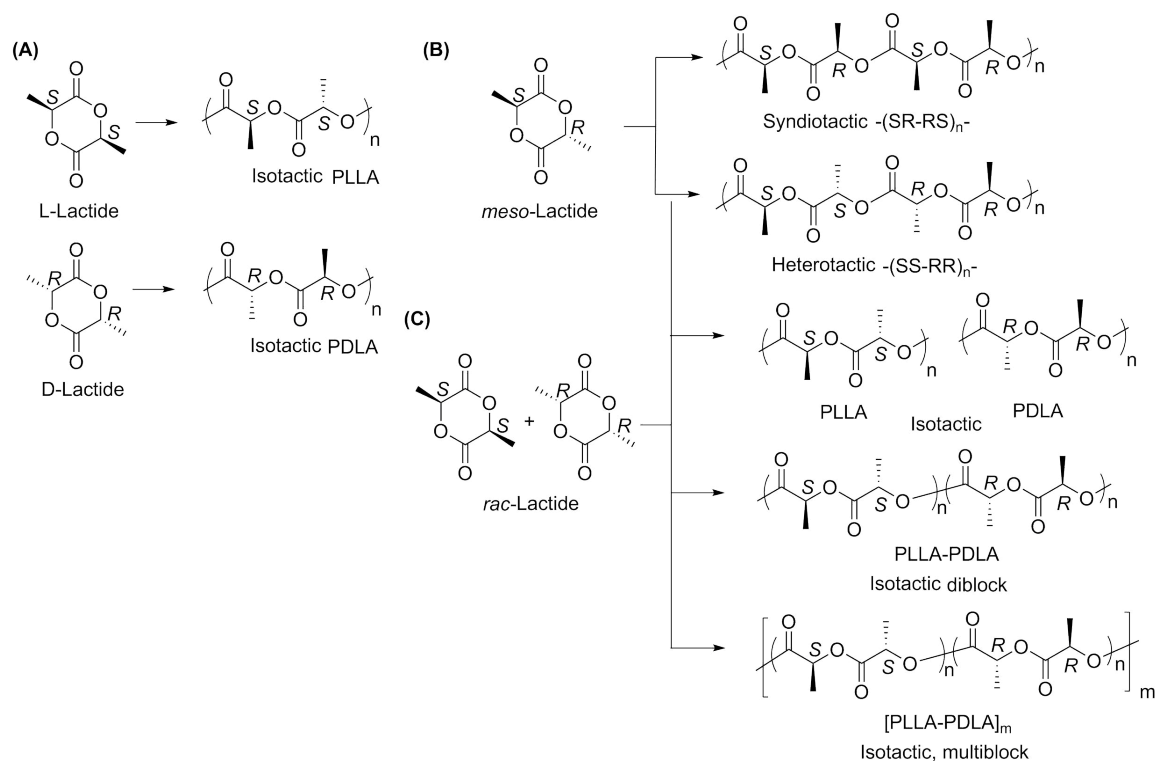
The stereoselectivity of the ROP of *rac*-lactide can be achieved by two approaches: (i) a chain-end control mechanism and (ii) an enantiomorphic site control mechanism. In the chain-end control mechanism, the configuration of the incoming lactide is determined by the configuration of the last inserted lactide type. The catalyst in this case usually is coordinated with bulky and achiral ligands. In the enantiomorphic site control mechanism, the catalyst shows a certain type of chirality that dictates which lactide monomer to be inserted first. In the ROP of enantiopure L-lactide or D-lactide, the resulting products are stereoregular isotactic polymers (Scheme 1.2A). In the ROP of *rac*-lactide, a heterotactic PLA with repeating units of -SS-

RR- can be generated by insertion of L- and D-lactide alternatively via a chain-end control mechanism (Scheme 1.2B). The ROP of *rac*-lactide using a non-stereoselective catalyst results in atactic polymers, the polymer chain structures of which contain stereogenic centers with random chirality. The ROP of *meso*-lactide can result in syndiotactic polymer with opposite stereochemistry in each of the two neighboring stereogenic centers. Their repeating units attain a -SRSR- configuration via a chain-end-control mechanism when the chain end favors the exact configuration or via an enantiomorphic site control mechanism. It can also generate heterotactic PLA with repeating units in an -SRRS- configuration via a chain-end control mechanism that favors a monomer having an opposite configuration of the last inserted monomer.

The microstructure (tacticity) of PLA can be determined by NMR spectroscopic analysis. For example, through the homodecoupled ^1H NMR technique, the protons of the methine groups of most PLAs are detected as singlet signals. Each peak is expressed in terms of probability. Assigning the integrated peaks is based on the values predicted by Bernoullian mathematical basis for tetrad stereosequences. The probability of PLA stereosequences evaluated by P_i or P_s , which stands for probability of finding iso diads enchainment, and P_r or P_m , which stands for the probability of finding meso diads.

1.4 Physical Properties of Polylactide

The physical properties of PLA are controlled by the stereochemistry of the polymer chains. Four PLA microstructures have been reported, namely isotactic, syndiotactic, heterotactic, and atactic (figure 1.1). The isotactic PLLA (Poly L-Lactide) has high



Scheme 1.2: Microstructures of PLA obtained from stereocontrolled ROP of (A) L-lactide and D-lactide, (B) meso-lactide, and (C) *rac*-lactide.

crystallinity with a melting point (T_m) of 180 °C and a glass transition temperature (T_g) of 50 °C. Isotactic diblock PLA generated from *rac*-lactide shows an increased melting point of $T_m = 230$ °C, due to the strong interactions between PLLA and PDLA chains. The atactic polymer is amorphous and does not have a melting point but has a glass transition temperature (T_g) of 50–60 °C. Heterotactic PLA has no T_g and melts at 130 °C. Recently, many studies have been reported to deal with the synthesis of stereoblock copolymers from *rac*-lactide to improve thermal and mechanical properties.

1.5 Metal Complexes for Lactide Polymerization

The ROP of lactide was first reported in 1932 by Carruthers et al.,²¹ who used different metal salts (i.e., zinc chloride and potassium carbonate) to promote the reaction. However, their method gave poor control over molecular weights. In 1996, Spassky's group for the first time achieved the synthesis of stereocopolymers of *rac*-lactide using a chiral-salen aluminum alkoxide (**1**, Figure 1.2) as the catalyst.²² The group has successfully obtained 80% isotactic of poly-D-Lactide at less than 40% conversion. The reaction was performed at 70 °C using [LA]/[Al]: 75/1 (mol/mol) in toluene. The reaction took 281 h to get 97% conversion. The polydispersity (D) (which is defined by the ratio of the weight-average molar mass M_w and the number-average molar mass M_n of the resulting polymers varied from 1.05 in 5 hours to 1.3 in 281 h. The increase in dispersity with reaction time was attributed to transesterification reactions that took place during long-time polymerization.

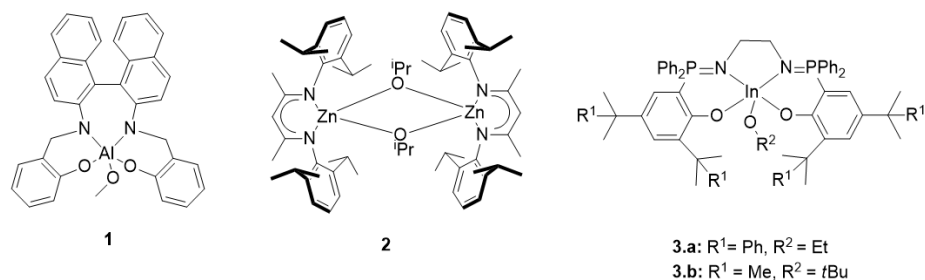


Figure 1.2: Metal complexes used by the Spassky group (**1**), the Coates group (**2**), and the Williams group (**3**) as catalysts for the stereocontrolled synthesis of PLA.

In 1999, zinc complexes with substituted β -diiminato ligands (**2**, Figure 1.2) were reported by Coates and co-workers as catalysts for the ROP of *rac*-lactide.²³ These catalysts exhibited selectivity in forming heterotactic PLA ($Pr = 0.97$) with

high molecular weight (up to 63.3 kg mol⁻¹). The selectivity was explained by a chain-end control mechanism. Since then, and many single-site metal catalysts have been developed to produce stereoregular PLA. The stereoselectivity in such catalyst systems arises from two possible mechanisms: the site control mechanism and the chain-end control mechanism. In the site control mechanism, such as Spassky's catalytic system, the structure of the inserted lactide monomer is determined by the chirality of the ligands surrounding the metal site. Alternatively, the chain-end control mechanism occurs when the configuration of the incoming inserted monomer is selected by the stereogenic centre of the last repeating monomer unit in the growing chain.

Recently, Williams and co-workers²⁴ made significant and interesting progress in stereoselective polymerization by using highly effective indium catalysts bearing tetradentate [N,N,O,O] Schiff base (**3**, Figure 1.2). They obtained isotactic PLA ($P_i = 0.92$) with a low catalyst loading (0.2 mol%) at 25 °C through the chain-end control mechanism. This catalytic system led to high control in stereoselectivity without the need for specific chirality in the complex structure. Other metal complexes such as lithium, magnesium, sodium, and scandium for the ROP of lactide were also reported.^{16,25-28} It is worth noting that upon metal selection, important parameters other than polymerization rate and stereocontrol come into account, including low cost, tolerance, abundance, lack of odor, and low toxicity.

1.6 Iron(III) Catalyzed Polymerization Reactions

Due to its low toxicity, biocompatibility, and abundance, iron could be a perfect metal candidate in the development of the catalytic polymerization of lactides.²⁹ In this section, examples of iron complexes used to catalyze the ROP of lactide will be highlighted.

Byers and co-workers³⁰ reported electrochemically switchable Fe(III)/Fe(II) systems for catalyzing the ROP of LA. The monomeric bis(alkoxide) iron(II) complexes (**4**, Figure 1.3) were obtained by reacting different alcohols with dialkyl iron(II) complex precursors. It was also found that the bis(alkoxide) iron(II) complexes generated in situ by reacting dialkyl iron(II) complex precursors with the suitable alcohols in the polymerization could achieved results similar to those using the purified complexes. Up to 15 sequential additions of lactide were introduced to the reaction to examine if the catalyst system has a living polymerization behavior. The results obtained actually confirmed that the reaction was a living polymerization system and the products attained high molecular weights and slightly changed dispersity. The authors also reported that when the Fe(II) center of the complex was oxidized to Fe(III), its catalytic effects on the polymerization completely vanished. The polymerization was only active when the complex is in the Fe(II) state. Their studies demonstrated the impact of the iron oxidation state in the polymerization reaction.

Several groups reported the formation of active alkoxide metal complexes using epoxides,(Scheme1.3). For example, Pang et al. used propylene oxide (PO) to generate salen-Fe(III) alkoxides for the ROP of rac-lactide.³¹ PO is known to be a necessary component for the initiation step of the polymerization. The coordination of PO to

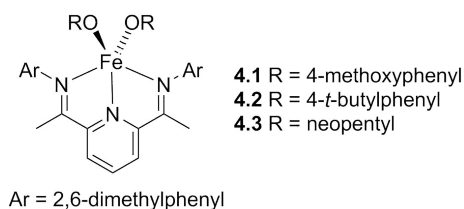
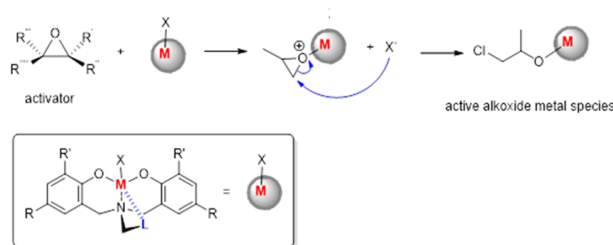


Figure 1.3: Iron complexes designed by the Byers group for polymerization of lactide.



Scheme 1.3: alkoxide metal formation mechanism

the metal center would activate the epoxide toward nucleophilic attack by chloride that is bonded to the metal or from an external source, resulting in the ring opening of the epoxide and the formation of an iron alkoxide. Reactions with less than 50% PO (v/v in toluene) were relatively slow. At concentrations above 50%, the reactivity reached a plateau. The activity of the catalyst was zero when PO was replaced with toluene.

Lamberti and co-workers reported an increase of conversion from 33% to 65% in 4 h when bis(triphenylphosphine)iminium chloride (PPNCl) was used as an external chloride source for the polymerization of L-LA using salen, salan and salalen iron(III) complexes (**5**, Figure 1.4).³² Moreover, their studies showed that catalyst **5.2**, which is less Lewis acidic than **5.1** and **5.3**, delivered the highest catalytic efficiency to the ROP of L-LA.

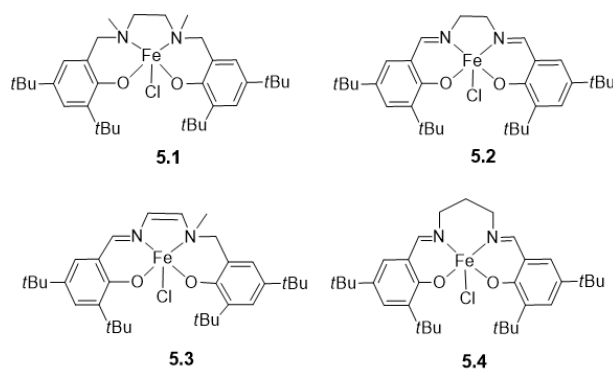


Figure 1.4: Iron complexes used by the Lamberti group.

1.7 Objectives of this Thesis

This MSc dissertation includes two complete research projects focusing on the study of iron-based complexes and organometallic compounds. My previous work in the Kozak group investigated a series of iron(III) amino-bis(phenolate) complexes, which feature different coordination geometries (both trigonal bipyramidal and square-based pyramidal). These complexes will be synthesized and characterized. Their catalytic effects on the formation of cyclic and polycarbonate products were examined previously.³³ The complexes in a trigonal bipyramidal geometry were found to be active in polycarbonate synthesis. The nature of the pendant donor on the ligand backbone along with the phenolate substituents of the ligand played critical roles in controlling product selectivity. So, the objectives of the first research project will focus on applying some of the previously prepared iron(III) amino-bis(phenolate) complexes as catalysts in *rac*-lactide polymerization. The results of this project will be reported and discussed. The parameters of each reaction will be optimized to locate optimal reaction time, catalyst loading, temperature, choice of co-catalyst (additive), and its loading.

The second research project will be done with the Zhao group. It will involve the development of new dithiafulvene (DTF) and ferrocene (Fc) derivatives for both fundamental studies and applications in optoelectronic devices (e.g., electrochemical sensors). This project aims to design a new type of tweezer-like compounds that contain a Fc central unit and two DTF end groups. These compounds' molecular structures and electronic properties will be studied using NMR, MS, IR, UV-Vis absorption, and cyclic voltammetry (CV) analyses. The aim also to be able to get crystals of the compounds to allow their solid-state structures and packing properties to be elucidated by X-ray single crystallographic analysis. we expect a redox behavior of the Fc and DTF groups. These compounds could show multi-stage redox activity and supramolecular interactions with cyclodextrins (CDs). The detailed properties will be investigated by CV analysis in combination with density functional theory (DFT) and molecular dynamics (MD) simulations. The results of this project disclose that this type of compound could have the potential to act as a conformationally switchable molecular device under redox control.

Bibliography

- [1] Della Monica, F.; Buonerba, A.; Capacchione, C. Homogeneous Iron Catalysts in the Reaction of Epoxides with Carbon Dioxide. *Adv. Synth. Catal.* **2019**, *361*, 265–282.
- [2] Morgan, J. W.; Anders, E. Chemical composition of Earth, Venus, and Mercury. *Proceedings of the National Academy of Sciences of the United States of America (Proc Natl Acad Sci U S A)* **1980**, *77*, 6973–6977.
- [3] Abbaspour, N.; Hurrell, R.; Kelishadi, R. Review on Iron and Its Importance for Human Health. *J. Res. Med. Sci.* **2014**, *19*, 164–174.
- [4] David, J. R. Iron and Its Alloys: A Comprehensive Study. *Mater. Sci. Eng.* **2006**, *25*, 245–260.
- [5] Housecroft, C. E.; Sharpe, A. G. *Inorganic Chemistry*, 3rd ed.; Pearson Education Ltd., 2008; p 714.
- [6] Mond, L. Preparation of Nickel Carbonyl. *J. Chem. Soc.* **1891**, *59*, 604.
- [7] Berthelot, M. Formation of Ethyl Alcohol by the Action of Water on Ethylene. *C. R. Hebd. Seances Acad. Sci.* **1981**, *93*, 1663–1664.
- [8] Reppe, W. V. Chemistry of Acetylenes. XVIII. Cyclization of Dialkynes with Cobalt Complexes. *Liebigs Ann. Chem.* **1953**, *582*, 13.
- [9] Kealy, T. J. P.; Pauson, P. L. A New Type of Organo-Iron Compound. *Nature* **1951**, *168*, 1039.

- [10] Collman, J. P. Organometallic Chemistry of Iron Carbonyls. *Acc. Chem. Res.* **1975**, *8*, 342.
- [11] Bianchini, C.; Meli, A.; Peruzzini, M.; Vizza, F.; Zanolini, F.; Frediani, P. A homogeneous iron(II) system capable of selectivity catalyzing the reduction of terminal alkynes to alkenes and buta-1,3-dienes. *Organomet.* **1989**, *8*, 2080.
- [12] Nampoothiri, K. M.; Nair, N. R.; John, P. J. An overview of the recent developments in polylactide (PLA) research. *Bioresour. Technol.* **2010**, *101*, 8493–8501.
- [13] Vaidya, A.; Pandey, R.; Mudliar, S.; Kumar, M. S.; Chakrabarti, T.; Devotta, S. A critical review on environmental implications of iron oxide reduction. *Crit. Rev. Environ. Sci. Technol.* **2005**, *35*, 429–467.
- [14] Mohapatra, A. K.; Mohanty, S.; Nayak, S. K. Thermal properties and degradation behavior of thermoplastic composites. *J. Thermoplastic Compos. Mater.* **2014**, *27*, 699–716.
- [15] Rittinghaus, R. D.; Schäfer, P. M.; Albrecht, P.; Conrads, C.; Hoffmann, A.; Ksiazkiewicz, A. N.; Bienemann, O.; Pich, A.; Herres-Pawlis, S. New Kids in Lactide Polymerization: Highly Active and Robust Iron Guanidine Complexes as Superior Catalysts. *ChemSusChem* **2019**, *12*, 2161–2165.
- [16] Platel, R. H.; Hodgson, L. M.; Williams, C. K. Biocompatible Initiators for Lactide Polymerization. *Polym. Rev.* **2008**, *48*, 11–63.

- [17] Masutani, K.; Kimura, Y. *Polymer Chemistry Series*; Royal Society of Chemistry: Cambridge, 2014; pp 1–36.
- [18] Worch, J. C.; Prydderch, H.; Jimaja, S.; others Stereochemical enhancement of polymer properties. *Nat. Rev. Chem.* **2019**, *3*, 514–535.
- [19] Jacobsen, S.; Fritz, H. G.; Degée, P.; Dubois, P.; Jerome, R. Polylactide (PLA)—a New Way of Production. *Polym. Eng. Sci.* **1999**, *39*, 1311–1319.
- [20] Kricheldorf, H. R.; Weidner, S. M. Syntheses of polylactides by means of tin catalysts. *Polym. Chem.* **2022**, *13*, 1618–1647.
- [21] Carothers, W. H.; Dorough, G. L.; Natta, F. J. v. Studies of Polymerization and Ring Formation. X. The Reversible Polymerization of Six-Membered Cyclic Esters. *J. Am. Chem. Soc.* **1932**, *54*, 761–772.
- [22] Spassky, N.; Wisniewski, M.; Pluta, C.; Le Borgne, A. Highly Stereoelective Polymerization of rac-(D,L)-Lactide with a Chiral Schiff's Base/Aluminium Alkoxide Initiator. *Macromol. Chem. Phys.* **1996**, *197*, 2627–2637.
- [23] Cheng, M.; Attygalle, A. B.; Lobkovsky, E. B.; Coates, G. W. Single-Site Catalysts for Ring-Opening Polymerization: Synthesis of Heterotactic Poly(Lactic Acid) from rac-Lactide. *J. Am. Chem. Soc.* **1999**, *121*, 11583–11584.
- [24] Myers, D.; White, A. J. P.; Forsyth, C. M.; Bown, M.; Williams, C. K. Phosphasalen Indium Complexes Showing High Rates and Iselectivities in Rac-Lactide Polymerizations. *Angew. Chem. Int. Ed.* **2017**, *56*, 5277–5282.

- [25] Wheaton, C. A.; Hayes, P. G.; Ireland, B. J. Complexes of Mg, Ca and Zn as Homogeneous Catalysts for Lactide Polymerization. *Dalton Trans.* **2009**, *25*, 4832–4846.
- [26] Dean, R. K.; Reckling, A. M.; Chen, H.; Dawe, L. N.; Schneider, C. M.; Kozak, C. M. Ring-Opening Polymerization of Cyclic Esters with Lithium Amine-Bis(Phenolate) Complexes. *Dalton Trans.* **2013**, *42*, 3504–3520.
- [27] Devaine-Pressing, K.; Lehr, J. H.; Pratt, M. E.; Dawe, L. N.; Sarjeant, A. A.; Kozak, C. M. Magnesium Amino-Bis(Phenolato) Complexes for the Ring-Opening Polymerization of rac-Lactide. *Dalton Trans.* **2015**, *44*, 12365–12375.
- [28] Devaine-Pressing, K.; Oldenburg, F. J.; Menzel, J. P.; Springer, M.; Dawe, L. N.; Kozak, C. M. Lithium, Sodium, Potassium and Calcium Amine-Bis(Phenolate) Complexes in the Ring-Opening Polymerization of rac-Lactide. *Dalton Trans.* **2020**, *49*, 1531–1544.
- [29] O’Keefe, B. J.; Monnier, S. M.; Hillmyer, M. A.; Tolman, W. B. Rapid and Controlled Polymerization of Lactide by Structurally Characterized Ferric Alkoxides. *J. Am. Chem. Soc.* **2001**, *123*, 339–340.
- [30] Biernesser, A. B.; Li, B.; Byers, J. A. Redox-Controlled Polymerization of Lactide Catalyzed by Bis(Imino)Pyridine Iron Bis(Alkoxide) Complexes. *J. Am. Chem. Soc.* **2013**, *135*, 16553–16560.
- [31] Pang, X.; Duan, R.; Li, X.; Chen, X. Bimetallic Salen–Aluminum Complexes: Synthesis, Characterization and Their Reactivity with rac-Lactide and ϵ -Caprolactone. *Polym. Chem.* **2014**, *5*, 3894.

- [32] Cozzolino, M.; Leo, V.; Tedesco, C.; Mazzeo, M.; Lamberti, M. Salen, Salan and Salalen Iron(III) Complexes as Catalysts for CO₂/Epoxide Reactions and ROP of Cyclic Esters. *Dalton Trans.* **2018**, *47*, 13229–13238.
- [33] Andrea, K. A.; Butler, E. D.; Brown, T. R.; Anderson, T. S.; Jagota, D.; Rose, C.; Lee, E. M.; Goulding, S. D.; Murphy, J. N.; Kerton, F. M.; Kozak, C. M. Iron Complexes for Cyclic Carbonate and Polycarbonate Formation: Selectivity Control from Ligand Design and Metal-Center Geometry. *Inorg. Chem.* **2019**, *58*, 11231–11240.

Chapter 2

Iron Amino-bis(phenolate)

Complexes for Lactide

Polymerization

The contents of this chapter were performed by Fatma Takfa, who conducted all the experimental work and data collection under the supervision of Dr. Chris Kozak.

2.1 Introduction

Amino-(bisphenolate)s are versatile and efficient ligands that have drawn significant attention in the development of transition metal complexes as catalysts for polymerization reactions.¹⁻⁵ Figure 2.1 illustrates the general structure of an amino-(bisphenolate) system which consists of two phenolate units tethered by an amine linker. The phenolate and the amine groups which work together to provide multiple

coordination sites for complexation with diverse metal ions.

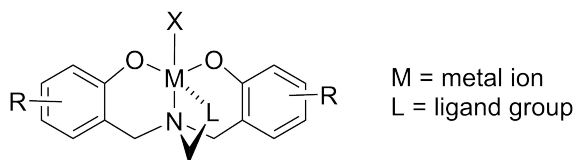
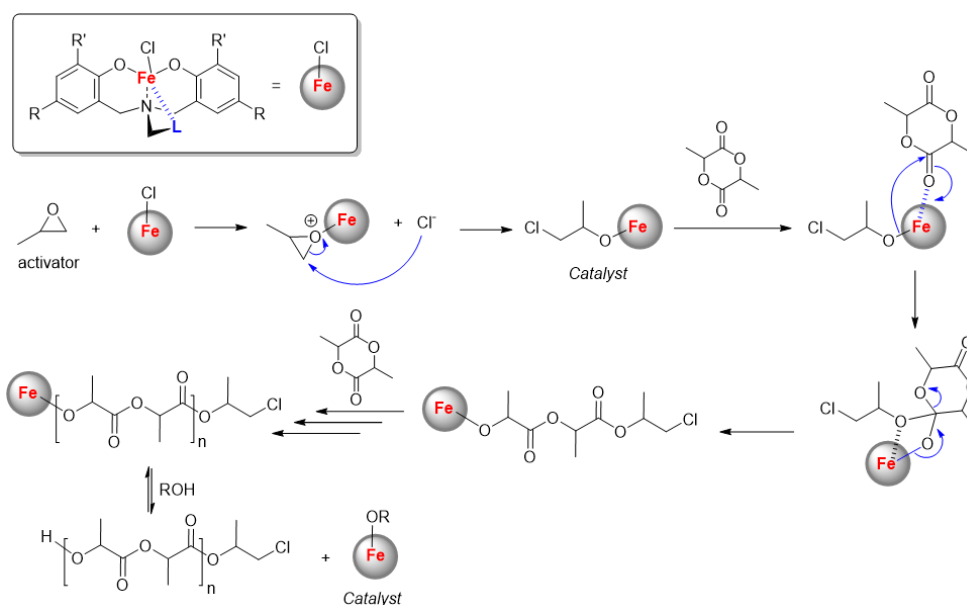


Figure 2.1: General structure of an amino-bis(phenolate) ligand coordinating with a metal center.

This type of ligand can be easily accessed through modular synthesis, which in turn allows for flexible electronic and steric controls over reactivity and catalytic performance. Iron-aminophenolate complexes have been recently investigated as catalysts for various important synthetic reactions, such as atom transfer radical polymerizations,⁶ hydrosilylation of ketones/aldehydes,⁷ and the formal hydroamination of olefins.⁸ These complexes can also serve as effective catalysts promoting the coupling of benzyl halides with aryl Grignard reagents.⁹⁻¹¹ In 2015, the first work of using iron amino-bis(phenolate) complexes to catalyze the copolymerization of CO₂ with cyclohexene oxide and aldehydes was reported.¹² Iron's abundance, low toxicity, and versatile redox chemistry make these catalysts sustainable alternative to traditional heavy metal-based catalytic systems.

In the field of lactide polymerization, iron amino-bis(phenolate) catalysts have demonstrated reasonable activity and potential in achieving stereocontrol. Nevertheless, this area of research remains relatively unexplored. and awaits continued efforts to fully disclose the scope and efficiency of iron amino-bis(phenolate) catalysts in lactide polymerization. In this work, we aimed to examine the catalytic performance of a series of functionalized iron amino-bis(phenolate) complexes in catalyzing the ROP

of lactide. As illustrated in Scheme 2.1, these catalysts were expected to promote polymerization of lactide through a proposed mechanism similar to that previously described by Shaver and co-workers,¹³ who used salen–iron complexes for stereoselective polymerization of lactide and caprolactone. In our work, we proposed that the iron amino-bis(phenolate) complexes would show tunable catalytic properties, since recent studies indicated that modification of the structure of amino-bis(phenolate) ligand and experimental conditions (e.g., solvents and additives) could result in diverse structures and reactivities.^{14–16} In our target system, the iron(iii) center is coordinated with a chloride anion, which is in line with the research of several groups, who utilized the chloride form of iron complexes instead of the alkoxide form.^{13,17,18} The alkoxide form can be formed *in situ* by using an epoxide as the initiator. This reaction serves as the first step (initiation) in the polymerization mechanism. As shown in Scheme 2.1, an epoxide first attacks the iron center to generate an active iron alkoxide *in situ* as the active species, while the Fe–Cl bond is cleaved. The occurrence of this step has been experimentally validated by MALDI-MS analysis. In the following propagation step, lactide monomers continuously approach the iron center and are incorporated into a metal–alkoxide bond, proceeding by a coordination–insertion mechanism. At the outset of this work, it was anticipated that incorporation of different substituent groups into the two phenolate units would deliver different steric and electronic effects on the iron center. Moreover, the geometry and reactivity of the iron center could be further modified by the nitrogen ligand in proximity to the bisphenolate. The following sections describe the detailed results of our synthesis and characterization of these catalysts along with the study of their catalytic properties.

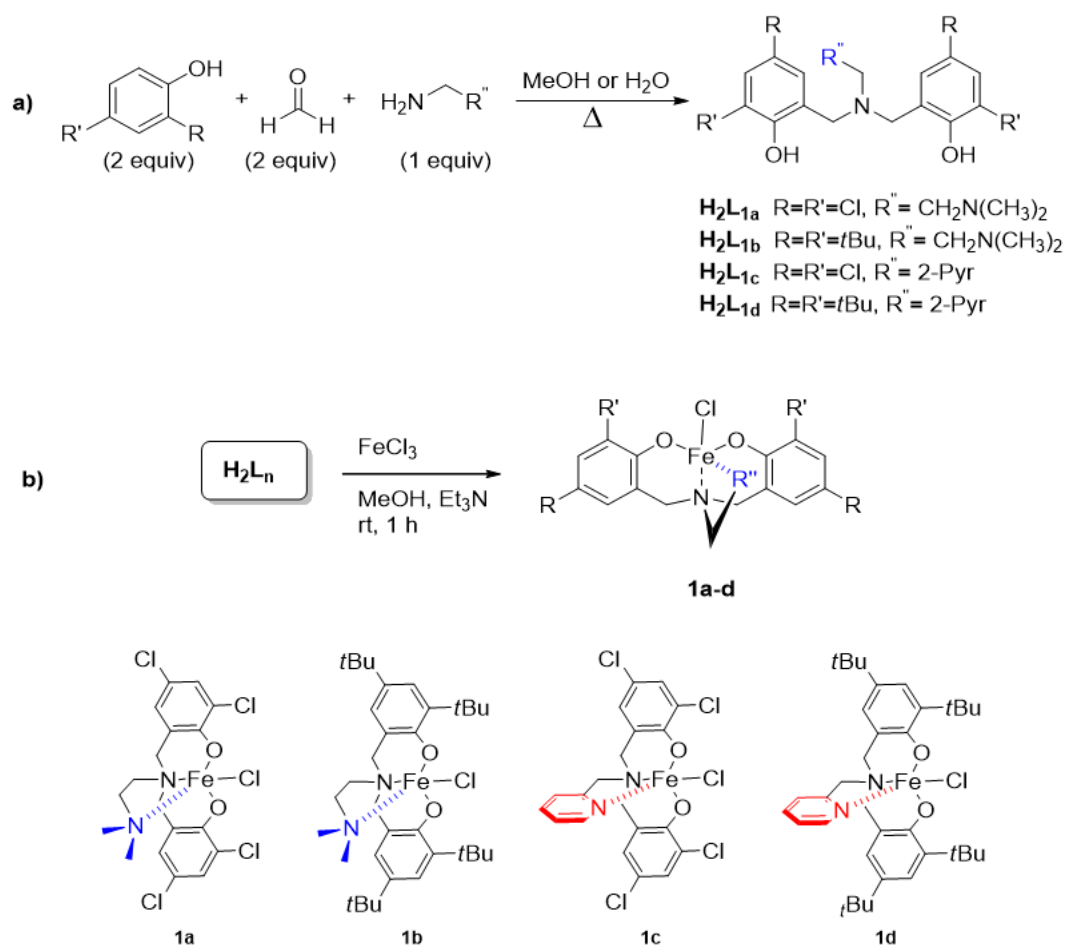


Scheme 2.1: Catalytic cycle of iron-oxide promoted PLA synthesis proposed by Shaver *et al.*

2.2 Synthesis of Tetradentate Amino-bis(phenolate) Ligands

A modified Mannich condensation was used to synthesize a variety of tetradentate amine-bis(phenolate) ligands (Scheme 2.2(a)).

At first, a solution of formaldehyde, the desired 2,4-disubstituted phenol, and amine was prepared in methanol or water. The reaction mixture was heated to reflux overnight. A total of four ligands, namely **H₂L-1a-d**, were acquired from this condensation approach. The yield of these ligands varied from 23 to 78%. In their molecular structures, electron-withdrawing chloro and bulky *tert*-butyl substituents were introduced for the purposes of enhancing the Lewis acidity of the metal center. This effect was previously reported to improve the ability of the metal to bind to



Scheme 2.2: Synthesis of **a**) amino-bis(phenolate) ligands and **b**) their complexes with iron(III).

epoxide,¹⁹ and hence was expected to deliver beneficial effects on their catalytic performance for lactide polymerization.

2.3 Synthesis of Iron(III) Amino-bis(phenolate) Complexes

The four obtained amino-bis(phenolate) ligands were used to form tetradentate complexes with iron(III) following previously reported procedures.²⁰ As shown in Scheme 2.2(b), the reactions occurred between anhydrous FeCl₃ and the **H₂L** ligands, respectively, in the presence of Et₃N in methanol. After the reactions, HCl was added to neutralize the reaction mixture, affording complexes **1a–d** (Scheme 2.2(b)) as purple solids, which were further purified by filtration and rinsed with toluene to yield pure products high yields (ca. 85%) except the case of **1b** (42%). The structures and purity of these complexes were confirmed by MALDI-TOF MS and CHN elemental analyses.

2.4 Characterization

The synthesized ligands **H₂L-1a–d** were characterized by ¹H and ¹³C NMR spectroscopy. The obtained NMR spectra were found to be consistent with the literature data,²¹ confirming their structures and purity (see Appendix A for details).

Due to their paramagnetic nature, iron–amino-bis(phenolate) complexes **1a–d** could not be characterized by NMR. We therefore chose elemental and MALDI-TOF MS analyses to confirm their structures and purity. In the elemental analysis, the iron complexes, after routine purification steps, were exhaustively dried under vacuum on a Schlenk line overnight to remove water, since water was found to readily coordinate to the metal center when the complexes were exposed to air.

We run the MS analysis on a matrix-assisted laser desorption/ionization (MALDI) mass spectrometer coupled with a time of flight (TOF) detector. The samples were prepared by dissolving the complexes in dichloromethane and then mixed with anthracene as a matrix at a 1:10 ratio. Anthracene served as an ideal matrix for these iron complexes primarily due to its absence of functional groups, allowing it to generate radical cations of each complex through electron abstraction. The isotopic distributions of the iron–amino-bis(phenolate) complexes were simulated and compared with the experimental data (see Appendix A for details).

2.4.1 Computational Modeling of 1a–d

To gain insights into the experimental data as well as to facilitate understanding of structure–catalytic property relationships for complexes **1a–d**, we carried out computational model studies by density functional theory (DFT) calculations.

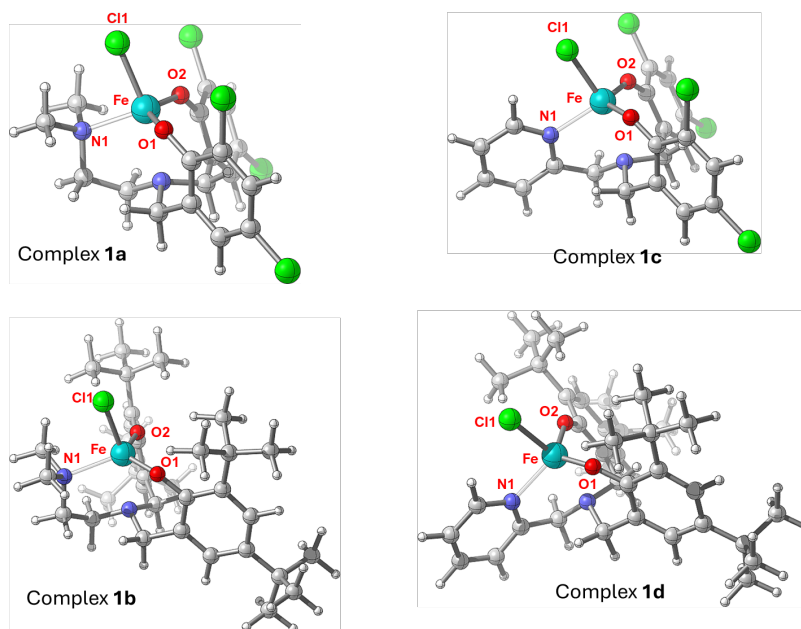


Figure 2.2: Optimized geometries of complexes **1a–b** by DFT calculations.

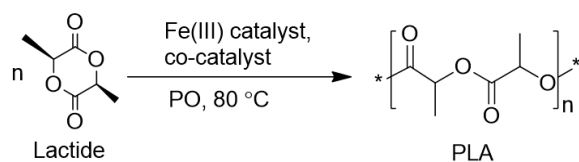
Figure 2.2 shows the geometries of **1a–d** optimized at the TPSSH/Def2-SVP level. The key charge and geometric parameters of these complexes are summarized in Figure 2.3. The modeling results show that complex **1c** shows the shortest Fe–Cl bond and the highest atomic (Mulliken) charge of Fe. These features suggest that **1c** possesses a high degree of Lewis acidity, which is beneficial for activating the catalyst in the initiation step. This can explain the better performance of this complex than the others in catalyzing the polymerization reaction (Results will be shown in the next section)

		Selected bond distances (in Å)			
		1a	1b	1c	1d
Mulliken charge of Fe					
1a	0.871				
1b	0.854				
1c	0.900				
1d	0.890				
		Fe-Cl1	Fe-N1	Fe-O1	Fe-O2
		2.25	2.29	2.24	2.27
		2.24	2.27	2.19	2.20
		1.87	1.86	1.86	1.86
		1.87	1.87	1.87	1.86

Figure 2.3: Atomic charges of Fe and selected bond lengths in **1a–d**.

2.5 Ring-Opening Polymerization of Lactide under the Catalysis of Iron Amino-Bis(phenolate) Complexes

The iron(III) complexes **1a–d** were used as the catalysts for the ROP of LA. Experimental parameters were chosen based on recent literature,¹⁷ so that our results can be compared with existing systems for evaluation of their applicability.



Scheme 2.3: Polymerization of LA to PLA

Polymerization screenings were initially performed in neat propylene oxide (PO) at 80 °C, (Scheme 2.3). For most of the solution polymerizations, a ratio of 100:1 [LA]:[Fe] was employed, where [LA] is the mole concentration of lactide and [Fe] is the mole concentration of the iron amino-bis(phenolate) complex used. PPNCI (bis(triphenylphosphor-onylidene)ammonium chloride) was chosen initially as a co-catalyst, as we considered that the bulky cation would exhibit low ion pairing to the chlorine atom, making it a better nucleophile for initiation processes. Experiments were run in duplicate to ensure reproducibility. The iron complexes with dichloro-substituted phenolate rings were anticipated to be the most active. This is because the dichloro substitution increases the Lewis acidity of the iron center, making it more electropositive and thus more prone to nucleophilic attack compared to the *t*Bu substituted analogues.

The polymerizations were monitored by performing ^1H NMR analysis of aliquots taken from the reaction mixtures at different times. The obtained data were used to establish the kinetic properties of the polymerization reactions. The resulting polymers were characterized by gel permeation chromatography (GPC), differential scanning calorimetry (DSC), and MALDI-TOF MS to assess the quality of the polymers. The experimental results have confirmed that all the four iron complexes show catalytic effects on the ROP of *rac*-lactide.

2.5.1 Results of Polymerization and Kinetic Studies

The results of polymerizations under the catalysis of complexes **1a–d** are summarized in Table 2.1. High conversions of lactide monomer were achieved under low catalyst loading (1mol % and 0.5 mol %). Catalyst loadings of 1% and 0.5% of complex **1c** gave nearly quantitative conversion of lactide after 60 minutes, but decreasing catalyst loading to 0.2% and 0.1% resulted in 61% and 49% conversion, respectively.

In comparing complexes' activity, one can see that the polymerization reaction rates were much faster under complex **1c** than the other complexes. The experimental data showed that in the absence of PPNCl, polymerization of LA using complex **1c** reached 85% conversion in four hours (entry 2, Table 2.1). This means the formation of PLA without adding an external co-catalyst can happen, but at a much slower rate. The use of Et₃NHCl, DMAP, and TBAB as co-catalysts showed similar effects under the same conditions (entries 8, 9, 11 and 12, Table 2.1). Polymerizations at 80 °C achieved the highest conversions for all complexes tested. When the temperature decreased from 80 °C to 40 °C, the conversion decreased (entry 14, Table 2.1). Polymerization at 80°C required shorter time to achieve higher conversion than at a lower temperature. To investigate the order of the polymerization reaction, A kinetic study was performed by ¹H NMR monitoring of the polymerization of 100 equiv. of LA catalyzed by complex **1c**. During the experiment, samples were taken and analyzed every 10 minutes. With the experimental data, the relationship of $\ln([LA]_0/[LA]_t)$ versus time was plotted. The kinetic plot reveals first-order dependence of the LA concentration at 22 °C (Figure 2.4) and at 80 °C (Figure 2.5, which can be described by $k_{app} = 0.0419 \pm 0.004 \text{ min}^{-1}$, $R_2 = 0.96$).

Table 2.1: Polymerization data of rac-LA with complexes **1a-1d** in PO.

Entry	Cat.	Co-cat.	[LA]/[I]	T(°C)	t (h)	Conv. ^b (%)	M _{wc} ^c (kg/mol)	D ^d
1	1c	PPNCl	100/1	80	1	93	3.9	1.02
2	1c	–	100/1	80	4	85	4.10	1.10
3 ^e	1c	PPNCl	100/1	80	4	0	–	–
4	1c	PPNCl	100/1	22	24	93	10.7	1.40
5	1c	PPNCl	200/1	80	4	92	5.90	1.06
6	1c	PPNCl	400/1	80	4	61	4.30	1.06
7	1c	PPNCl	800/1	80	4	49	3.40	1.05
8	1c	Et ₃ NHCl	100/1	80	4	93	5.40	1.10
9	1c	DMAP	100/1	80	4	91	4.00	1.07
10	1c	PPNCl	100/1	100	4	89	2.50	1.05
11	1c	TBAB	100/1	80	4	94	3.30	1.02
12 ^f	1c	PPNCl	100/1	80	4	94	3.2	1.07
13	1c	PPNCl	200/1	80	1	81	3.00	1.02
14	1a	PPNCl	100/1	80	4	89	3.7	1.06
15	1a	N/A	100/1	80	4	25	3.70	1.03
16	1d	PPNCl	100/1	40	4	46	N/A	N/A
17	1d	PPNCl	100/1	60	2	49	3.50	1.32
18	1d	PPNCl	100/1	80	2	88	4.50	1.09
19	1b	PPNCl	100/1	60	4	44	3.60	1.08

All the polymerization reactions were carried out in 3 mL of PO solution, [LA]₀ = 0.40 g,

[Cat.]/[Co-cat.] = 100 : 1. ^bMeasured by ¹H NMR. ^bDetermined in THF by GPC equipped with a multi-angle light-scattering detector. ^dDispersity (D) = M_w/M_n . ^epolymerizations were carried out in toluene. ^fPolymerizations were carried out in 3 mL of CHO

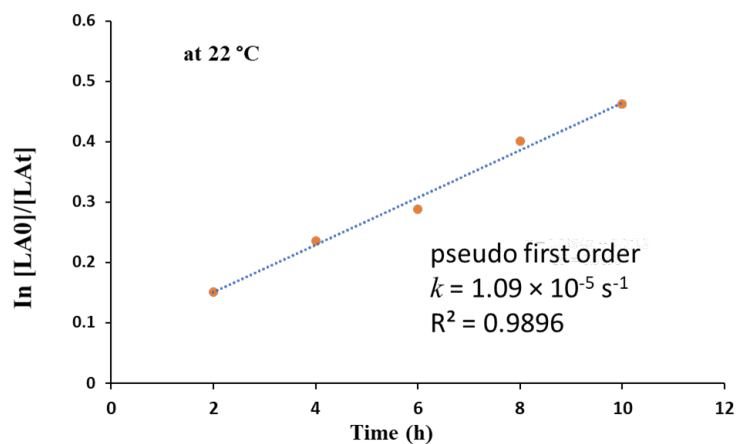


Figure 2.4: Plot of $\ln[\text{LA}]_0/[\text{LA}]_t$ versus time at 22 °C for the ROP of *rac*-lactide catalyzed by complex **1c** ($[\text{LA}]:[\mathbf{1c}] = 100:1$, $[\text{LA}] = 0.133$ g/mL in PO). The dashed lines are the linear regression fits.

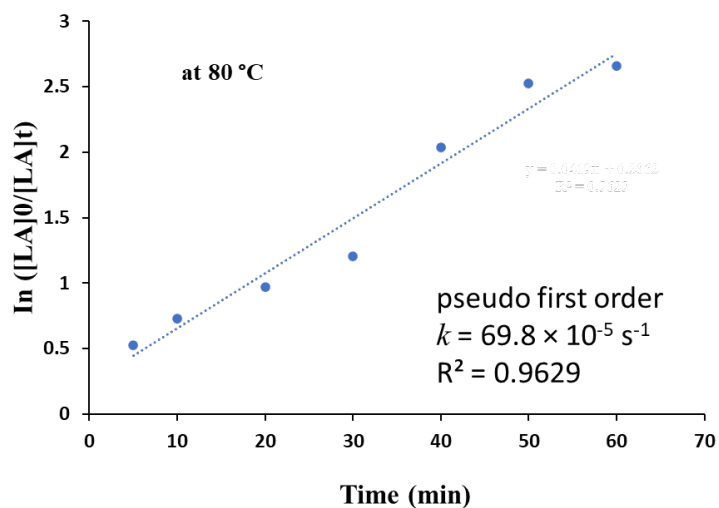


Figure 2.5: Plot of $\ln([\text{LA}]_0/[\text{LA}]_t)$ versus time at 80 °C for the ROP of *rac*-lactide catalyzed by complex **1c** ($[\text{LA}]:[\mathbf{1c}] = 100:1$, $[\text{LA}] = 0.133$ g/mL in PO). The dashed lines are the linear regression fits.

Kinetic plots for the ROP of *rac*-LA under the catalysis of **1c** (Figure 2.7) also

showed a first-order dependence of the catalyst at lower catalyst loading when applied from Figure 2.6.

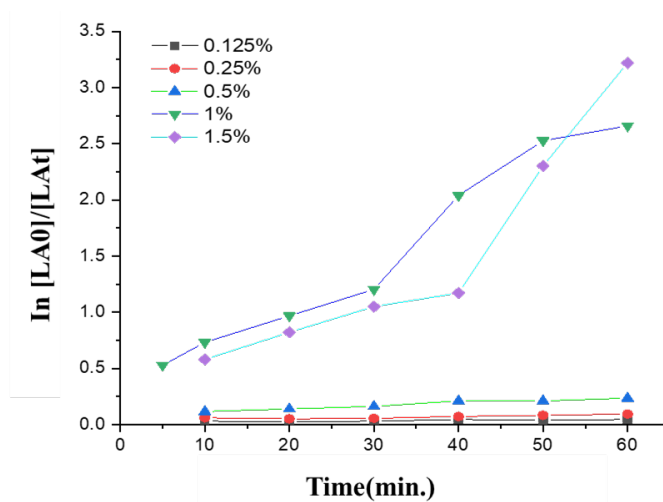


Figure 2.6: Plot of $\ln[LA]_0/[LA]_t$ versus time at different catalyst loading.

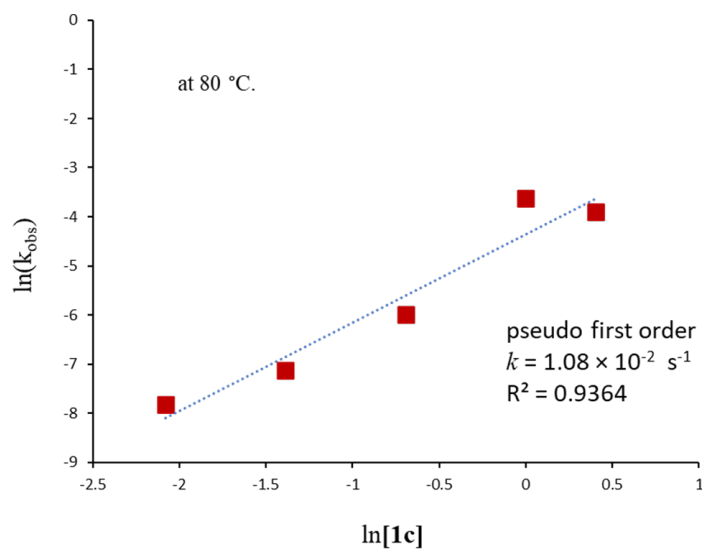


Figure 2.7: Plot of the correlation of $\ln(K)$ versus $\ln[1c]$ for the ROP of *rac*-lactide catalyzed by complex **1c** in PO at 80 °C. The dashed line in the bottom plot is the linear regression fit.

2.6 Characterizations of the polymer products

The conversion of lactide monomer to polymer was determined by NMR analysis of the crude products after removal of the PO. Experimentally, the crude product was purified by dissolving in dichloromethane followed by precipitation with acidified methanol. A colorless polymer was obtained upon removing the methanol by decantation. With this product, molecular weight, dispersity, end group properties, and glass transition temperature were measured.

2.6.1 NMR Spectroscopic Analysis

The ^1H NMR spectrum of a representative polymerization product is shown in Figure 2.8. The multiplet at $\delta = 5.12$ ppm corresponds to the methine proton of unreacted LA, and the multiplet at 5.17 ppm is due to the methine protons of PLA. Conversion of monomer to polymer can be calculated based on the integral ratio of the PLA peaks to the sum of LA and PLA peaks, i.e., $I_{PLA}/(I_{PLA+ILA})$.

2.6.2 Gel Permeation Chromatographic Analysis

The polymers were characterized by gel permeation chromatography (GPC) to determine the molecular weight (M_n) and molecular weight distribution (D). Figure 2.9 shows a representative chromatogram of the GPC analysis. The molecular weights of the polymers range from 2–6 kDa and the molecular weight distribution (M_w/M_n) was close to 1.0 (Table 2.1). The GPC determined molecular weights of isolated polymers were found to be lower than anticipated. MALDI-TOF MS analysis showed $(\text{C}_3\text{H}_4\text{O}_2)_n$ and $(\text{CH}_3\text{CHOCH}_2\text{Cl}$ -end group) which may be of adventitious water

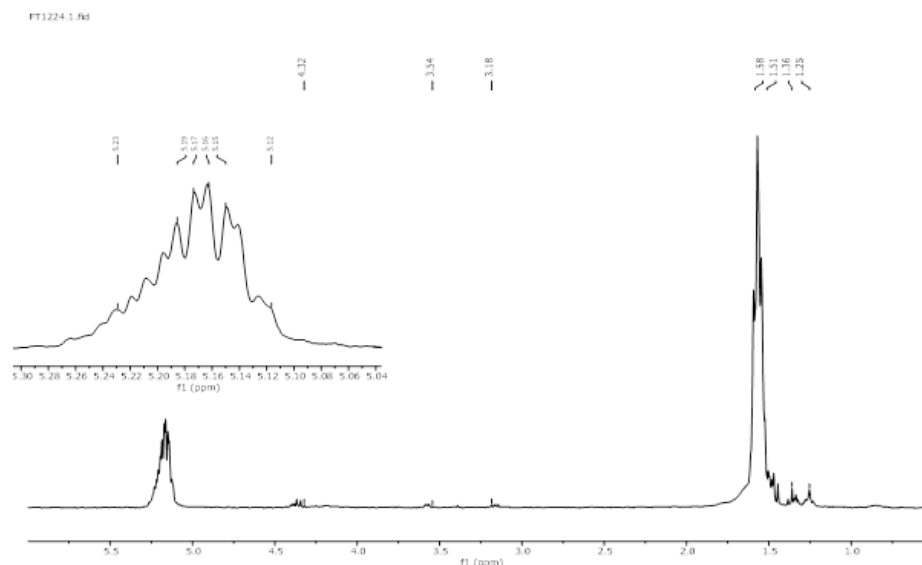


Figure 2.8: ^1H NMR (300 MHz, CDCl_3) spectrum of a representative PLA product.

causing chain transfer reactions. At $80\text{ }^\circ\text{C}$, the polymer obtained from shorter reaction times (entries 1 and 10, Table 2.1) showed slightly higher molecular weights than those run for a longer time. This outcome suggests the occurrence of transesterification at a longer reaction time. When the reaction was allowed to run at a longer time but at a lower temperature, the molecular weight of the polymer obtained was the highest (entry 4, Table 2.1).

2.6.3 MALDI-TOF MS Analysis

MALDI-TOF MS analysis provides a valuable tool for analyzing the repeating units and the end groups of polymers. In our MS studies, 2,5-dihydroxybenzoic acid (DHBA) was used as the matrix. The MD data for the polymers resulting from **1c** catalyzed reactions confirmed the role of PO. The fragment peaks observed at $144m + 94.5 + 23$ were assigned to $m(\text{C}_6\text{H}_8\text{O}_4)$, $m(\text{CH}_3\text{CHOCH}_2\text{Cl-end group})$ and $m(\text{Na}^+)$, respectively. Based on experimental observations, the reaction mechanism

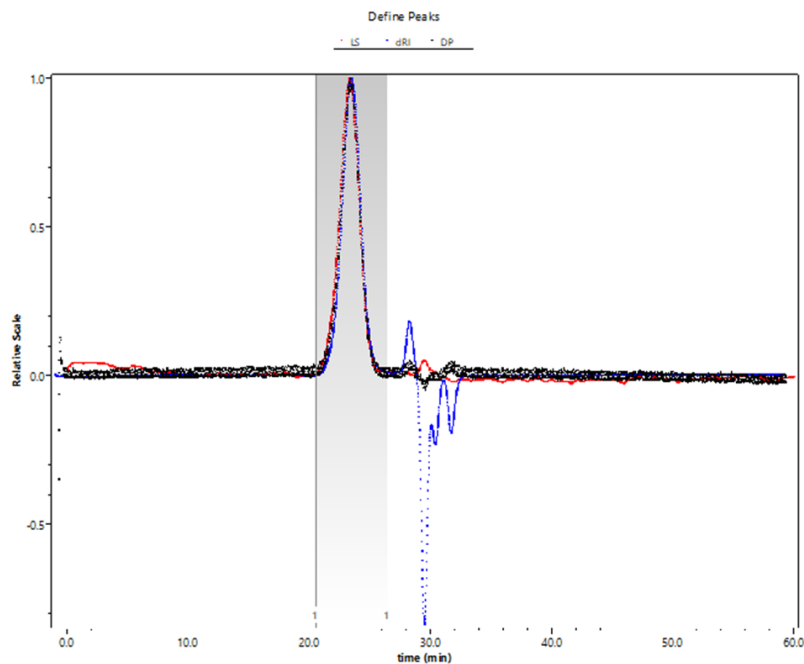


Figure 2.9: Representative GPC results for the ROP of LA with **1c** ($M_w = 5.90$ kDa, $D = 1.06$).

can be regarded as in consistence with that previously mentioned in Scheme 2.1. PO as the alkoxide source reagent is essential. when it was replaced with toluene, no polymerization was observed (entry 3, Table 2.1). when different co-catalysts were used in the polymerization, data showed their role in the structure of the end group.

2.6.4 Differential Scanning Calorimetric Analysis

Glass transition temperatures (T_g) were measured using Differential scanning calorimetric (DSC) analysis of the obtained polymers. The polymers showed T_g values in the range of 45–52 °C, agreeing with that reported in the literature. A representative DSC trace of PLA obtained by complex **1c** is shown in Figure 2.11.

2.6.5 Homonuclear decoupled ^1H NMR Analysis

The stereochemistry of the obtained polymers was studied using homonuclear decoupled ^1H NMR (Figure 2.12). The probability of racemic enchainment of monomer units (P_r) of the PLA was found to be 0.46, indicating the polymers are atactic. The P_r values were calculated by $P_r = 2I_1/(I_1 + I_2)$, with $I_1 = \delta$ 5.19–5.24, $I_2 = \delta$ 5.13–5.19. Data in Table 2.2 shows that the tacticity of the PLA is not influenced much by change of co-catalyst.

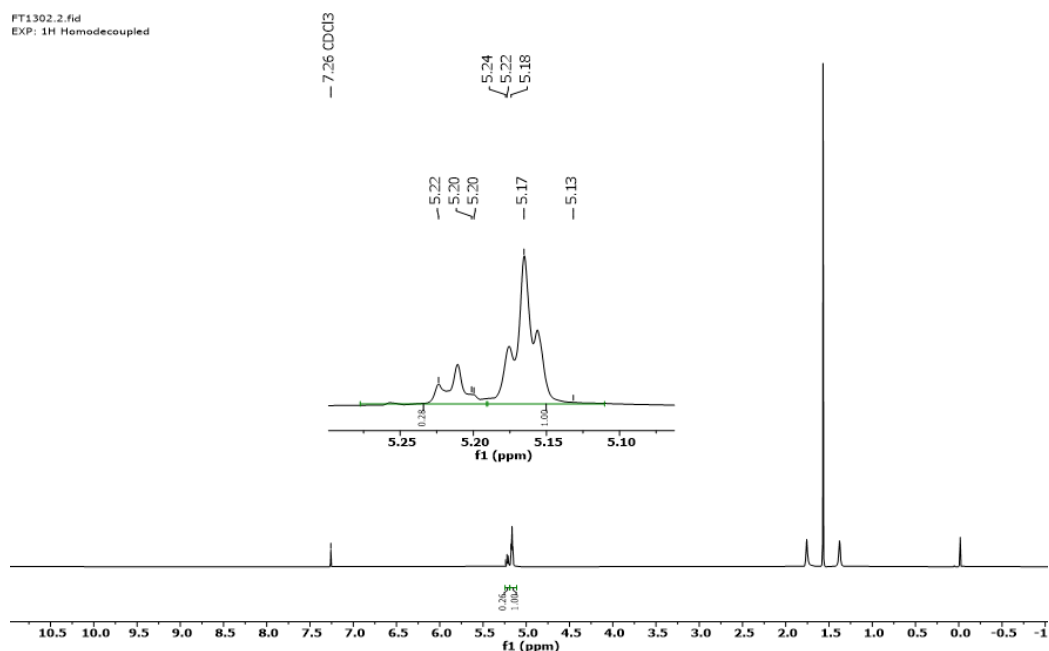


Figure 2.12: $[\text{H}]^1\text{H}$ NMR spectrum of PLA from **1c** (80 °C, 4 hours, $\text{Et}_3\text{NH}^+ \text{Cl}^-$, PO, $P_r = 0.48$).

Table 2.2: The effects of co-catalysts on the tacticity of PLA product, Reaction Parameters:(1% **1c**, 1% Co-catalyst, LA = 400 mg, PO = 3ml, t= 4 h, 80 °C)

Entry	co-cat.	Pr
1	PPNCl	0.46
2	Et ₃ NHCl	0.43
3	–	0.46

2.7 Conclusion

In this research project, four iron(III) amino-bis(phenolate) complexes (**1a–d**) were prepared and tested as catalysts for lactide polymerization reactions. Although these complexes were previously synthesized and reported, this is for the first time their catalytic application in lactide polymerizations was investigated. By varying the phenolate substituents, we were able to compare the effects of electron-withdrawing groups and sterically bulky groups on the ROP of *rac*-lactide. Our results indicate that the Lewis acidity of the metal center plays a key role in the catalytic performance. Variation of the pendant arm allowed us to evaluate whether bulky substituents hinder the polymerization process. All the complexes investigated here are effective catalysts for the ROP of *rac*-Lactide. Under various conditions, they give comparable results to the other iron(III) complexes reported in literature.^{13,17} Our current work points to optimal reaction parameters, which are reaction time 2 h, catalyst loading 1 mol%, and temperature (80 °C),

2.8 Experimental Section

2.8.1 Materials

All air- and moisture-sensitive compound manipulations were carried out using standard Schlenk-line techniques under a dry nitrogen atmosphere or a Braun Labmaster glove box. All solvents and reagents were obtained from commercial sources (Sigma-Aldrich). Anhydrous iron(III) chloride (FeCl_3 99.99% purity), tetrabutylammonium bromide (TBAB, 98% purity), bis(triphenylphosphoranylidene) ammonium chloride (PPNCl) (98% purity). Propylene oxide (PO) was purchased from Aldrich and freshly distilled from CaH_2 under reduced pressure and stored in a sealed flask in a glove box, *rac*-lactide was purified by recrystallization from chloroform. Glassware used in the reactions was dried in an oven at 120 °C overnight and exposed to vacuum–nitrogen cycles three times. Other chemicals were commercially available and used as received unless it was stated otherwise.

2.8.2 Experimental Methods

All ^1H NMR spectra were obtained in CDCl_3 purchased from Cambridge Isotope Laboratories, Inc. ^1H NMR spectra were recorded on a Bruker AVANCE III 300 MHz spectrometer and were referenced versus shifts of solvents containing residual protic impurities. MALDI-TOF MS analysis was performed by using Bruker ultrafleXtreme MALDI-TOF/TOF Analyser equipped with a reflector, delayed ion extraction, and (Nd:YAD) laser. Trans-2-[3-(4-*tert*-butylphenyl)-2-methyl-2-propenyldiene] malononitrile (DCTB) was used as a matrix for polymer samples with

sodium trifluoroacetate (NaTFA) as a cationizing agent. Preparation of the sample by dissolving matrix in THF (10 mg/mL), the polymer in dichloromethane (10 mg/mL), and the cationizing agent in THF (0.1 mol/L), combining the solutions at the ratio of 20:3:1 and spotting 1 μ L on the plate to dry. Data processing was performed using Polymerix@ software. Elemental analysis was conducted at the Centre for Environmental Analysis and Remediation, Saint Mary's University, Halifax, Nova Scotia.

GPC analysis was performed in THF at 25°C on a Wyatt Triple Detection (triple angle light scattering, viscometry and refractive index) system with Agilent 2600 series sample and solvent handling. The system used two Phenogel 103 Å 300 \times 4.60 mm columns (molecular weight range of 1 k to 75 k daltons). Samples were prepared at a concentration of 4 mg/mL and left to equilibrate for 15 min, then filtered through 0.2 μ m syringe filters before analysis. The GPC columns were eluted with HPLC grade THF at a flow rate of 0.30 mL/min with a 50 μ L injection volume.

Synthetic procedures

Synthesis of ligand H₂L_{1a}. According to a previously reported method,²¹ a solution of 2,4-dichlorophenol (20.1 g, 0.123 mol), *N,N*-dimethylethylenediamine (5.42 g, 0.0616 mol), and 37% aqueous formaldehyde (10.0 mL, 0.123 mol) in MeOH (30.0 mL) was stirred and refluxed overnight. Upon cooling, the oil mixture solidified and a large quantity of beige solid formed. The solvent was decanted from the solution, and the solid residue was recrystallized from CH₂Cl₂/MeOH to give a pure, white powder (13.06 g, 48% yield).

Synthesis of ligand H_2L_{1b} . According to a previously reported method,²¹ a solution of 2,4-dichlorophenol (10.1 g, 0.0616 mol), 2-aminomethylpyridine (3.35 g, 0.0308 mol), and 37% aqueous formaldehyde (5.00 mL, 0.0616 mol) in MeOH (30.0 mL) was stirred and refluxed overnight. Upon cooling, the oil mixture started to solidify and beige solid formed. The solvent was decanted, and the remaining solid residue recrystallized from $\text{CH}_2\text{Cl}_2/\text{MeOH}$ to give a pure, white powder (3.06 g, 23% yield).

Synthesis of ligand H_2L_{1c} . According to a previously reported method,²¹ a solution of 2,4-di-*tert*-butylphenol (25.4 g, 0.123 mol), *N,N*-dimethylethylenediamine (6.69 g, 0.0616 mol), and 37% aqueous formaldehyde (10.0 mL, 0.123 mol) in water (50.0 mL) was stirred and refluxed overnight. The solid was filtered and recrystallized from $\text{CH}_2\text{Cl}_2/\text{MeOH}$ to give a pure, white powder (25.06 g, 78% yield).

Synthesis of ligand H_2L_{1d} . According to a previously reported method,²¹ a solution of 2,4-di-*tert*-butylphenol (20.1 g, 0.123 mol), 2-aminomethylpyridine (6.69 g, 0.0616 mol), and 37% aqueous formaldehyde (10.0 mL, 0.123 mol) in water (50.0 mL) was stirred and refluxed overnight. The solid was filtered and recrystallized from $\text{CH}_2\text{Cl}_2/\text{MeOH}$ to give a pure, white powder (13.06 g, 48% yield)

Synthesis of Fe(III) complex 1a. According to a previously reported method,²¹ to a MeOH solution (50.0 mL) of recrystallized H_2L_{1a} (4.38 g, 10.0 mmol) was added a solution of anhydrous FeCl_3 (1.62 g, 10.0 mmol) in MeOH resulting in an intense purple solution. To this solution was added triethylamine (2.00 g, 20.0 mmol), and the resulting mixture was stirred for 2 h. After stirring, the solvent was removed

under vacuum and the residue was extracted into EtOH /CH₂Cl₂. The mixture was filtered through a small silica plug and the solvent was removed under vacuum. The product was vacuum dried at 60 °C for 24 h to yield **1a** (4.63 g, 85%). MS (MALDI-TOF MS) negative mode, anthracene *m/z*: 526([**1a**]⁻), 491([**1a** - Cl]⁻), 561([**1a** + Cl]⁻)

Synthesis of Fe(III) complex 1b. The reaction was performed following the procedures described in the synthesis of **1a**, using recrystallized **H₂L_{1b}** (3.50 g, 6.67 mmol) was added a solution of anhydrous FeCl₃ (1.08 g, 6.67 mmol) in MeOH. Yield: 3.42 g (85%).

Synthesis of Fe(III) complex 1c. The reaction was performed following the procedures described in the synthesis of **1a**, using recrystallized **H₂L_{1c}** (4.58 g, 10.0 mmol) and anhydrous FeCl₃ (1.62 g, 10.0 mmol) in MeOH. Yield: 2.30 g (42%).

Synthesis of Fe(III) complex 1d. The reaction was performed following the procedures described in the synthesis of **1a**, using recrystallized **H₂L_{1d}** (5.45 g, 10 mmol) was added a solution of anhydrous FeCl₃ (1.62 g, 10 mmol) in MeOH. Yield: 5.22 g, 83%). MALDI-TOF MS: negative mode, anthracene *m/z*: 633([**1d**]⁻), 597([**1d** - Cl]⁻).

Polymerization procedure In a glove box, complexes(**1a–d**): (0.0278 mmol) and *rac*-lactide (0.40 g, 2.78 mmol) were placed in a microwave vial and PPNCl (0.0278 mmol), and distilled propylene oxide (3.00 mL) were added. The vial was placed in the pre-heated oil bath (40–80 °C) for the desired time duration. After this reaction

time, the vial was cooled and an aliquot was taken for ^1H NMR spectroscopic analysis (in CDCl_3) to determine conversion to polymer. The solvent was then removed under vacuum and the residue was washed with excess 5% (v/v with 1 M HCl) acidified methanol (> 10 mL). The vial was left in a freezer for polymer product to precipitate. For the kinetic experiments, a certain number of closed vials with identical concentrations were run simultaneously and then quenched sequentially at the desired time.

Bibliography

- [1] Tshuva, E. Y.; Goldberg, I.; Kol, M.; Weitman, H.; Goldschmidt, Z. Novel Zirconium Complexes of Amine Bis(phenolate) Ligands. Remarkable Reactivity in Polymerization of Hex-1-ene due to an Extra Donor Arm. *Chem. Commun.* **2000**, 379–380.
- [2] Tshuva, E. Y.; Goldberg, I.; Kol, M.; Goldschmidt, Z. Zirconium Complexes of Amine- bis(phenolate) Ligands as Catalysts for 1-Hexene Polymerization: Peripheral Structural Parameters Strongly Affect Reactivity. *Organomet.* **2001**, *20*, 3017–3028.
- [3] Tshuva, E. Y.; Goldberg, I.; Kol, M.; Goldschmidt, Z. Coordination Chemistry of Amine Bis(phenolate) Titanium Complexes: Tuning Complex Type and Structure by Ligand Modification. *Inorg. Chem.* **2001**, *40*, 4263–4270.
- [4] Golisz, S. R.; Bercaw, J. E. Synthesis of Early Transition Metal Bisphenolate Complexes and Their Use as Olefin Polymerization Catalysts. *Macromolecules* **2009**, *42*, 8751–8762.
- [5] Dong, Q.; Ma, X.; Guo, J.; Wei, X.; Zhou, M.; Liu, D. Synthesis, Characterization of a Novel Zinc Diamine–Bisphenolate Complex and Its Application as an Initiator for Ring-opening Polymerization of rac-Lactide. *Inorg. Chem. Commun.* **2008**, *11*, 608–611.
- [6] Allan, L. E. N.; MacDonald, J. P.; Nichol, G. S.; Shaver, M. P. Single Component Iron Catalysts for Atom Transfer and Organometallic Mediated Radical Poly-

- merizations: Mechanistic Studies and Reaction Scope. *Macromolecules* **2014**, *47*, 1249–1257.
- [7] Zhu, K.; Shaver, M. P.; Thomas, S. P. Stable and Easily Handled Fe(III) Catalysts for Hydrosilylation of Ketones and Aldehydes. *Eur. J. Org. Chem.* **2015**, *2015*, 2119–2123.
- [8] Zhu, K.; Shaver, M. P.; Thomas, S. T. Amine-bis(phenolate) Iron(III)-Catalyzed Formal Hydroamination of Olefins. *Chem. Asian J.* **2016**, *11*, 977–980.
- [9] Hasan, K.; Dawe, L. N.; Kozak, C. M. Synthesis, Structure, and C–C Cross-Coupling Activity of (Amine)bis(phenolato)iron(acac) Complexes. *Eur. J. Inorg. Chem.* **2011**, *2011*, 4610–4621.
- [10] Qian, X.; Dawe, L. N.; Kozak, C. M. Catalytic Alkylation of Aryl Grignard reagents by Iron(III) Amine-bis(phenolate) Complexes. *Dalton Trans.* **2011**, *40*, 933–943.
- [11] Reckling, A. M.; Martin, D.; Dawe, L. N.; Decken, A.; Kozak, C. M. Title of the Paper. *J. Organomet. Chem.* **2011**, *696*, 787–794.
- [12] Taherimehr, M.; Serta, J.; Kleij, A. W.; Whiteoak, C. J.; Pescarmona, P. P. New Iron Pyridylamino-Bis(Phenolate) Catalyst for Converting CO₂ into Cyclic Carbonates and Cross-Linked Polycarbonates. *ChemSusChem* **2015**, *8*, 1034–1042.
- [13] Duan, R.; Hu, C.; Li, X.; Pang, X.; Sun, Z.; Chen, X.; Wang, X. Air-Stable

- Salen–Iron Complexes: Stereoselective Catalysts for Lactide and ϵ -Caprolactone Polymerization through in Situ Initiation. *Macromolecules* **2017**, *50*, 9188–9195.
- [14] Plommer, H.; Stein, L.; Murphy, J. N.; Ikpo, N.; Mora-Diez, N.; Kerton, F. M. Copolymerization of CHO/CO₂ Catalyzed by a Series of Aluminum Amino-phenolate Complexes and Insights into Structure–Activity Relationships. *Dalton Trans.* **2020**, *49*, 6884–6895.
- [15] Siu, T. C.; Silva, I.; Lunn, M. J.; John, A. Influence of the Pendant arm in Deoxydehydration Catalyzed by Dioxomolybdenum Complexes Supported by Amine Bisphenolate Ligands. *New J. Chem.* **2020**, *44*, 9933–9941.
- [16] Durango-García, C. J.; Rufino-Felipe, E.; López-Cardoso, M.; Muñoz-Hernández, M. A.; Montiel-Palma, V. Synthesis and Structural Characterization of Lithium, Sodium and Potassium Complexes Supported by a Tridentate Amino-bisphenolate Ligand. *J. Mol. Struct.* **2018**, *1164*, 248–258.
- [17] Driscoll, O. J.; Leung, C. K. C.; Mahon, M. F.; McKeown, P.; Jones, M. D. Iron(III) Salalen Complexes for the Polymerisation of Lactide: Iron(III) Salalen Complexes for the Polymerisation of Lactide. *Eur. J. Inorg. Chem.* **2018**, *47*, 5129–5135.
- [18] Cozzolino, M.; Leo, V.; Tedesco, C.; Mazzeo, M.; Lamberti, M. Salen, Salan and Salalen Iron(III) Complexes as Catalysts for CO₂/Epoxide Reactions and ROP of Cyclic Esters. *Dalton Trans.* **2018**, *47*, 13229–13238.
- [19] Alhashmialameer, D.; Collins, J.; Hattenhauer, K.; Kerton, F. M. Iron Amino-

- bis(phenolate) Complexes for the Formation of Organic Carbonates from CO₂ and Oxirane. *Catal. Sci. Technol.* **2016**, *6*, 5364–5373.
- [20] Hasan, K.; Fowler, C.; Kwong, P.; Crane, A. K.; Collins, J. L.; Kozak, C. M. Synthesis and Structure of Iron(III) Diamine-bis(phenolate) Complexes. *Dalton Trans.* **2008**, 2991–2998.
- [21] Hasan, K.; Fowler, C.; Kwong, P.; Crane, A. K.; Collins, J. L.; Kozak, C. M. Synthesis and Structure of Iron(III) Diamine-Bis(Phenolate) Complexes. *Dalton Trans.* **2008**, *22*, 2991–2998.

Chapter 3

Phenyldithiafulvene-substituted Ferrocene Derivatives as Redox-regulated Molecular Switches

The contents of this chapter have been submitted to *J. Org. Chem.* for consideration of publication as a full research article. Contributions of the authors are described below: Fatma Takfa is the first author, who conducted all the experimental work and data collection. She also contributed to the manuscript preparation and editing. Liam Britt is a PhD student in the Zhao group, who contributed to the DFT and MD computational analyses reported in this article. Prof. Yuming Zhao is the supervisor of Fatma Takfa, who helped her design and develop this project. In this article, he acts as the corresponding author, who wrote the manuscript and contributed to

molecular modeling and data analyses.

3.1 Introduction

The discovery of ferrocene (Fc) in the early 1950s^{1,2} marked a groundbreaking event in modern organometallic chemistry. Intense research over the past 70 years has turned it into a versatile molecular building block widely applicable in synthetic chemistry, materials science, and biology.³⁻⁶ Ferrocene is a stable and redox-active molecule that can be used as a functional component in electroactive polymers,⁷ catalysts,⁸ chemical sensors,⁹ molecular machinery,¹⁰ and biological applications.¹¹ In the molecular structure of ferrocene, two planar cyclopentadienyl (Cp) rings are bonded to a Fe(II) center via an η^5 -mode. As such, each of the Cp rings can rotate about the Fe(II) center with a very low energy barrier (ca. 1–2 kcal mol⁻¹).¹²⁻¹⁵ This rotational flexibility imparts ferrocene with a unique function of “atomic ball bearing”.¹⁶ For example, a 1,1'-disubstituted ferrocene system can undergo a pivoting motion to adopt diverse conformations. Control over this uniaxial rotational mode has enabled fascinating molecular rotary devices to be fabricated, where Fc serves as an ideal molecular “hinge”.^{10,17,18} In general, the hinge-like motion of ferrocene can be regulated by various covalent and non-covalent forces, ranging from hydrogen bonding, acid–base interaction, metal coordination, photoisomerization, and redox reactions.^{10,18}

Recently, the class of molecular ensembles that integrate ferrocene with other organic π -electron donors at the 1,1'-positions has captured our attention. We were particularly intrigued to learn if the redox and conformational properties of this type

of molecule could be correlated for achieving more advanced molecular functions. It has been known that tuning the oxidation states on certain organic π -systems can switch their intermolecular interactions between repulsion and attraction. This type of switchability offers as a bottom-up means to control the formation or dissociation of dimeric and polymeric π -stacks.^{19–23} In 2012, Buchner *et al.*²⁴ reported a series of 1,1'-disubstituted ferrocene derivatives containing two redox-active 4,4'-bipyridinium “arms” (see Figure 3.1). These molecules acted as molecular rotors and showed conformations of a non-stacked *trans* form and a π -stacked *cis* form, which were switchable via a two-electron reduction reaction on the bipyridinium arms.

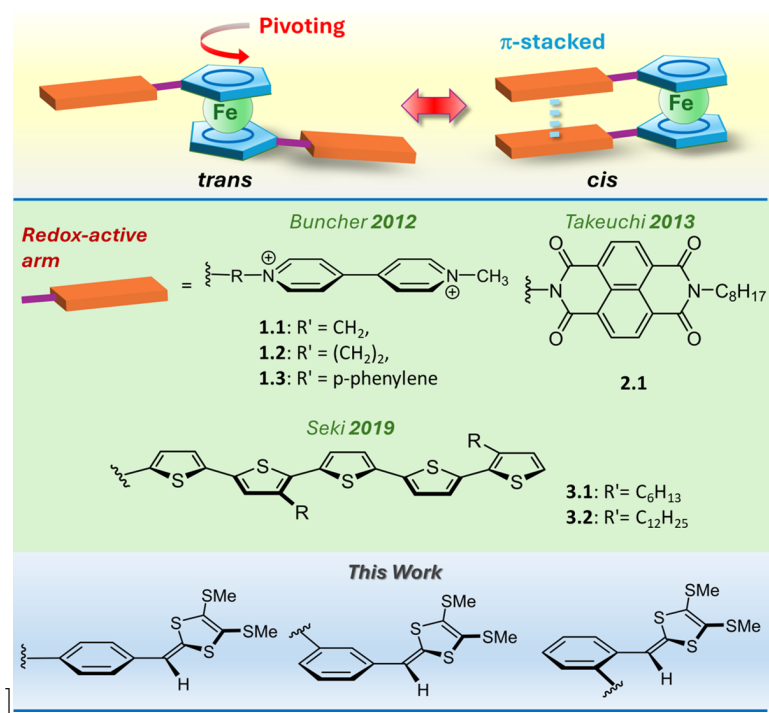


Figure 3.1: Ferrocene-hinged molecular switches containing two redox-active arene side arms as conformational modulators.

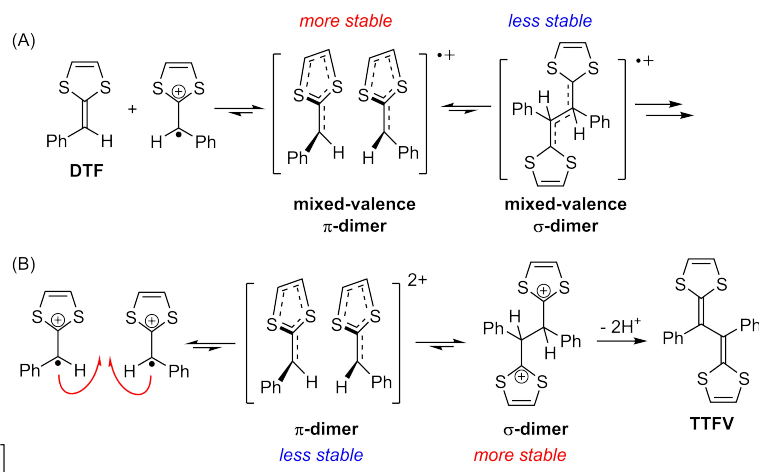
Takeuchi and co-workers in 2013 also developed a ferrocene-hinged molecular

switching system.²⁵ They used redox-active naphthalenediimide (NDI) groups to regulate the intramolecular π -stacking and conformation of the ferrocene derivative (Figure 3.1). Both of the above-mentioned switching systems were operated through reduction reactions on electron-accepting arene arms attached to a Fc unit. Very recently, Seki and co-workers synthesized a class of Fc-hinged bis(pentathiophene)s (Figure 3.1).²⁶ They found that the conformation of Fc in these compound is controllable by heat in condensed states. Nonetheless, the redox properties of these compounds were not investigated, although pentathiophene is a good electron donor that can be readily oxidized. Indeed, there have been no experimental attempts to examine the effects of oxidation on electron-rich Fc-hinged systems. Qiu and co-workers in 2016 computationally investigated a range of 1,1'-disubstituted ferrocenes as switchable nonlinear optic-phores through density functional theory (DFT) calculations.^{27,28} Some electron-donating and oxidizable arene units, including tetrathiafulvalene (TTF), trithiopene (TT), dithienylpyrrole (DTP), and buckybowls, were predicted to form intramolecular π -stacking in varied oxidation states and hence exert control over the pivoting motion of the Fc unit.

Inspired by the above-mentioned experimental and theoretical studies, we designed and synthesized a series of dithiafulvenyl (DTF) functionalized 1,1'-disubstituted ferrocene derivatives, which are hereafter referred to the (DTF)₂-Fc system. Our target molecules consist of three isomeric 1,1'-disubstituted ferrocene derivatives as illustrated in Figure 3.1. In these Fc-hinged molecular structures, each of the redox-active arms contains a π -electron-donating arene group, namely 1,4-dithiafulvene (DTF), and a phenylene bridge. DTF is a proaromatic five-membered heterocycle that is non-aromatic in the neutral state, but gains aromaticity when it is oxidized.

Due to this special property, DTF exhibits rich redox activity/reactivity and serves as a versatile redox-active building block in many molecular optoelectronic materials and devices.²⁹⁻³³

In an oxidative environment, two DTF moieties can react to yield a dimerized product. Scheme 3.1 outlines two possible pathways for a phenyl-substituted DTF as disclosed by our recent computational study.³⁴ In the first pathway (Scheme 3.1A), a DTF radical cation is combined with a neutral DTF molecule to yield a relatively stable mixed-valence (MV) π -dimer, but further reaction of this π -dimer into a σ -bonded dimer is exergonic (non-spontaneous). In the second pathway (Scheme 3.1B), two DTF radical cations overcome an energy barrier to form an unstable π -dimer, which then produces a more stable σ -dimer. After a process of double deprotonation, the σ -dimer is converted into a tetrathiafulvalene vinylogue (TTFV) product.³⁵



Scheme 3.1: (A) Interaction of neutral DTF and its radical cation. (B) Reaction of two DTF radical cations to form a tetrathiafulvalene vinylogue (TTFV) product.

At the beginning of our studies, we envisioned that the $(DTF)_2$ -Fc system would

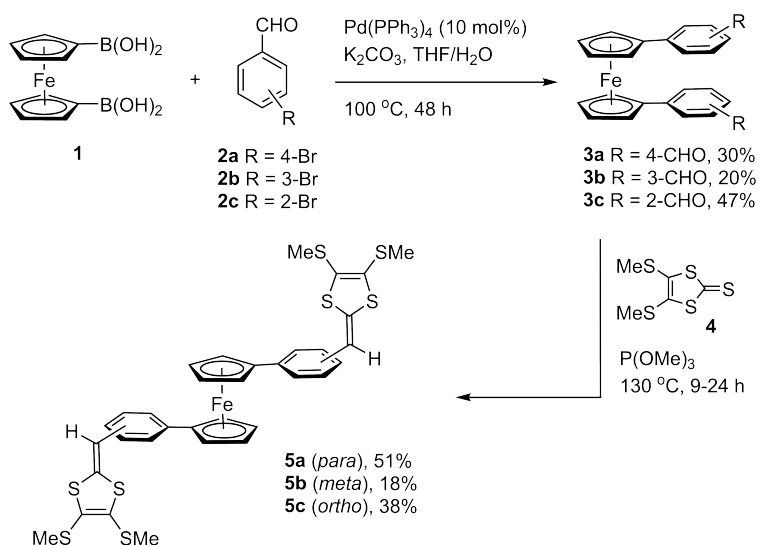
undergo multiple stages of oxidation, since DTF and Fc groups are both redox active. At various oxidation stages, the phenylene–DTF arms may generate attractive or repulsive interactions and hence result in different molecular conformations. Understanding the structural and redox properties of the (DTF)₂–Fc system is valuable for the development of novel Fc-based molecular materials and devices. Moreover, there is a fundamentally interesting question with regard to the (DTF)₂–Fc system; that is, upon oxidation could the DTF groups of this system react to generate TTFV-type products through the oxidative coupling mechanism depicted in Scheme 3.1B. If this reactivity exists, the (DTF)₂–Fc system may be further subjected to electropolymerization to yield redox-active macromolecular materials.^{24,29} Elucidation of these properties will provide useful guidance to rational incorporation of DTF and Fc groups in advanced molecular devices and functional materials. The following sections describe a combined experimental and computational study of this new class of (DTF)₂–Fc compounds.

3.2 Results and Discussion

3.2.1 Synthesis of (DTF)₂–Fc Compounds

The synthetic methods for our designed (DTF)₂–Fc compounds (**5a–b**) are described in Scheme 3.2.

At first, Suzuki–Miyaura cross-coupling between 1,1'-ferrocenediboronic acid (**1**) and bromobenzaldehydes (**2a–c**) was performed to yield ferrocene derivatives **3a–c**, respectively. All the coupling reactions required relatively high temperature



Scheme 3.2: Synthetic routes to (DTF)₂-Fc **5a-c**.

to accomplish, and the yields of these coupling reactions were modest. It was also observed that the use of freshly prepared catalyst, Pd(PPh₃)₄, was critical to these coupling reactions. Next, compounds **3a-c** were respectively subjected to an olefination reaction with dithiolethione **4**^{36,37} in the presence of trimethylphosphite (P(OMe)₃) to give the target compounds **5a-c**. Likewise, the yields of these olefination reactions were modest to low, even though a high temperature (130 °C) and prolonged reaction time (9–24 hours) were implemented. The relatively low yields of the olefination reactions can be attributed to the limited thermal stability of the final products. Purification of **5a-c** required careful silica column chromatographic separation. Overall, our two-step synthesis of **5a-c** is still efficient, allowing sufficient amounts of pure products to be acquired for further characterizations and analyses.

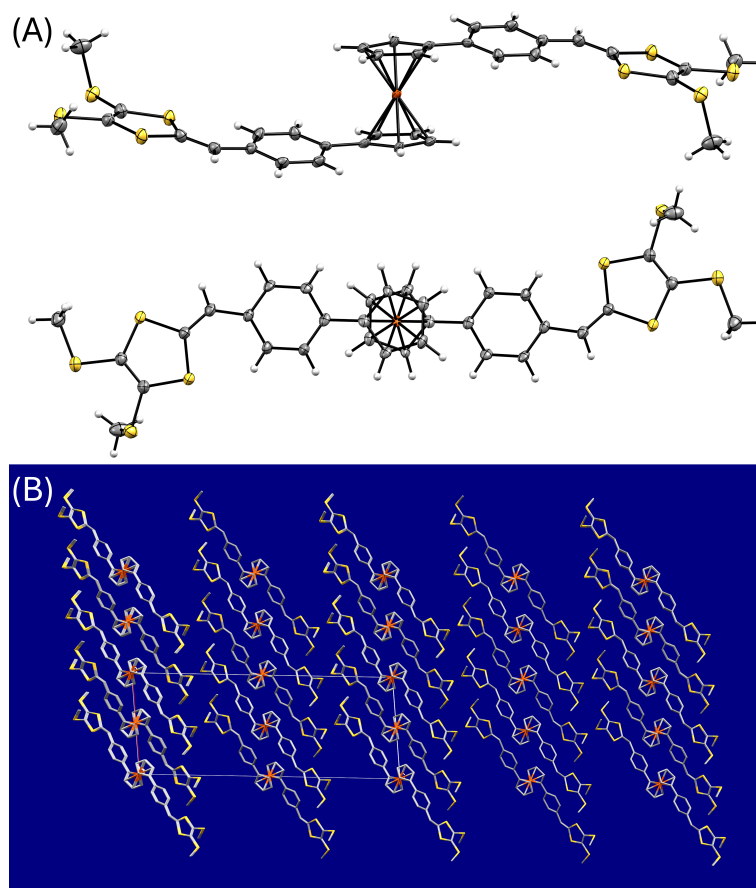


Figure 3.2: (A) ORTEP drawings (at 50% ellipsoid probability) of the molecular structure of **5a** viewed from different perspectives. (B) Crystal packing diagram of **5a** viewed along the *a*-axis of the unit cell (hydrogen atoms are omitted for clarity).

3.2.2 Crystallographic Properties of **5a** and **5c**

The molecular structures and purity of compounds **5a–c** were characterized by NMR, IR, and MS analyses (see Appendix B for details). Efforts to grow single crystals of these compounds were undertaken through various methods with success met for the *para* and *ortho* isomers, **5a** and **5c** through solvent layering.

Figure 3.2A shows the molecular structure of **5a** determined from the X-ray diffraction (XRD) analysis of its single crystals. In the crystalline state, the molecules

of **5a** adopt a *trans* conformation, in which the two phenylene–DTF arms are oriented in an anti-parallel manner. A high degree of co-planarity is seen between the DTF, *p*-phenylene, and cyclopentadienyl ring which are directly bonded to one another. For the central Fc unit, the two Cp rings show a staggered antiprismatic conformation. This molecular conformation maximizes the π -conjugation effects between the DTF and ferrocene groups. In the crystal structure, *trans* conformers of **5a** are packed in a monoclinic $I2/a$ space group (see Figure 3.2B). Among the molecules, intermolecular C–H $\cdots\pi$ and C–H \cdots S contacts can be observed. Intermolecular π -stacking among the arene units, however, is insignificant.

The molecular structure of compound **5c** in the crystal structure exhibits a *cis* conformation (Figure 3.3A). In contrast to its *para*-substituted isomer, The central Fc unit of **5c** shows an eclipsed prismatic conformation, while the DTF, phenylene, and Cp groups are interconnected to give a more twisted molecular shape as a result of the steric crowding arising from the *ortho*-substitution pattern. This geometry weakens the π -conjugation among the DTF, phenylene, and ferrocene groups. It is worth mentioning that the two phenyl rings of **5c** are somewhat slip-stacked, with the distance between the centroids of the two rings being 4.08 Å. In the crystal structure, molecules of **5c** are packed in a monolic $P2_1/n$ space group. Intermolecular C–H $\cdots\pi$, S \cdots S, and C–H \cdots S contacts play key roles in organizing the solid-state packing of **5c**.

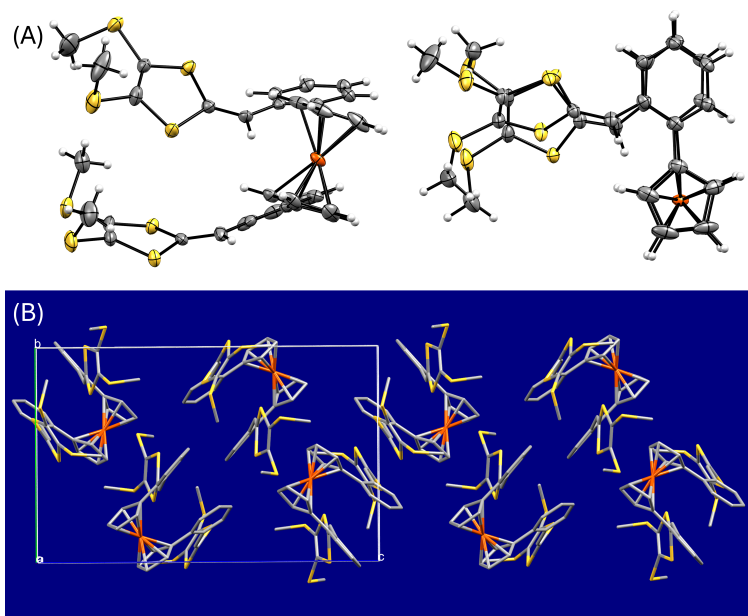


Figure 3.3: (A) ORTEP drawings (at 50% ellipsoid probability) of the molecular structure of **5c** viewed from different perspectives. (B) Crystal packing diagram of **5c** viewed along the *b*-axis of the unit cell (hydrogen atoms are omitted for clarity).

3.2.3 Conformational Properties of **5a–c**

With the solid-state structures of **5a** and **5c** established by XRD analysis, we next investigated the conformational properties of individual molecules of **5a–c** through molecular modeling methods, considering that individual molecules generally show conformational preference different than those in the aggregated state due to the lack of intermolecular packing effects. It is also noteworthy that each of the (DTF)₂-Fc derivatives possesses multiple arene rings that are subjected to rotational motions and hence may yield a variety of conformers and rotamers. To address this complex issue, we utilized the *Conformer-Rotamer Ensemble Sampling Tool* (CREST)^{38,39} developed by Grimme and co-workers in our search for the minimum-energy structures of **5a–c**.

The CREST calculations on **5a** provided a total of 64 stable conformers, all of which have the two phenylene-DTF arms aligned in the *cis* orientation. Further DFT optimization of the CREST predicted lowest-energy conformer was performed at the ω B97X-D/Def2-SVP level of theory,^{40–42} giving the structure as depicted in Figure 3.4. DFT optimization of the *trans* structure of **5a** determined by the X-ray analysis gave a *trans* conformer, the Gibbs energy of which is greater than that of the optimized *cis* conformer by 9.44 kcal mol⁻¹. It is therefore reasonable to conclude that individual molecules of **5a** in the gas phase or dilute solution favor the *cis* conformation over the *trans*. The better stability of the *cis* conformation can be attributed to the effects of intramolecular π -stacking between the phenylene and DTF rings. As shown in Figure 3.4A, the phenylene units and the DTF rings in the *cis* conformer of **5a** form slipped stacking. The detailed interactions can be visualized by the noncovalent interactions (NCI) analysis⁴³ based on the reduced density gradient (RDG) approach (see Figure 3.4C and D).

To experimentally probe the conformational properties of **5a** in the solution phase, we conducted variable temperature (VT) NMR analysis on it and the results are illustrated in Figure 3.5. The ¹H NMR spectrum of compound **5a** measured at room temperature (20 °C) shows three characteristic signals in the downfield region. The two pseudo doublets at 7.25 ppm and 6.99 ppm are due to the phenylene protons *ortho* and *meta* to the DTF group, which are labelled as **Hb** and **Hc**, respectively. The singlet at 6.64 ppm is due to the vinylic proton of the DTF group (labelled as **Ha**). When the temperature was gradually increased from 20 °C to 100 °C, the phenylene protons, **Hb** and **Hc**, showed downfield shifts, but the vinylic proton **Ha** shifted upfield. It is also noteworthy that at temperature above 80 °C, some shoulder

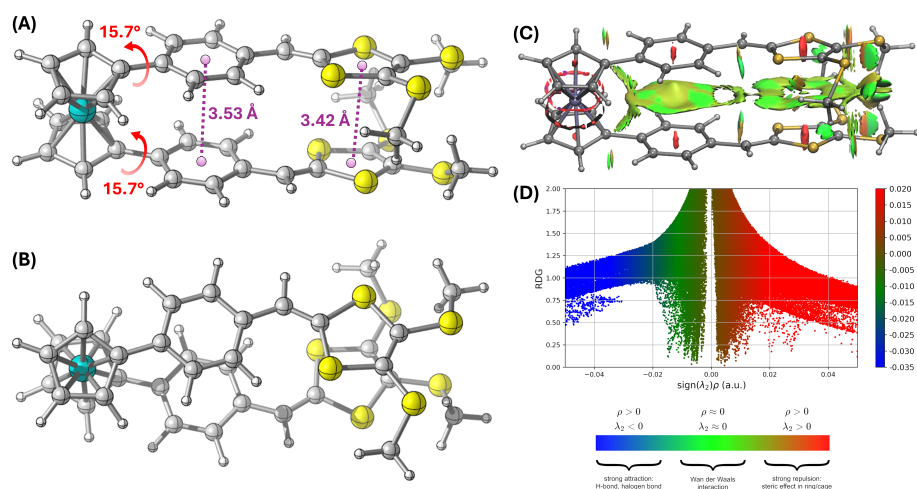


Figure 3.4: (A) and (B) Plots of optimized geometry of **5a** view from different perspectives with selected torsion angles and inter-centroid distances highlighted. (C) NCI analysis of **5a** showing the RDG isosurface (isovalue = 0.40 a.u.). (D) Plot of RDG vs $\text{sign}(\lambda_2)\rho$.

peaks next to the main peaks became discernible. This observation indicates that at relatively high temperature the conformation of **5a** fluctuates more significantly.

To better understand the conformational changes of **5a** in relation to temperature, molecular dynamics (MD) simulations of **5a** were performed at 298 K and 398 K, respectively. Our MD simulations employed the GFN2-xTB method⁴⁴ with the implicit solvent effects of DMF taken into account. After the simulations, the inter-centroid distances between the two phenylene rings (denoted as D_1) and the two dithiole rings (denoted as D_2) in the molecule of **5a** were measured from the MD trajectories (see Figure 3.6A–D). Correlations of these two inter-ring distances with simulation time can be used to evaluate the structural deviations of **5a** from intermolecularly π -stacked *cis* conformation. The analysis shows that at 398 K the structure of **5a** deviates very significantly from the initial π -stacked *cis* conformation

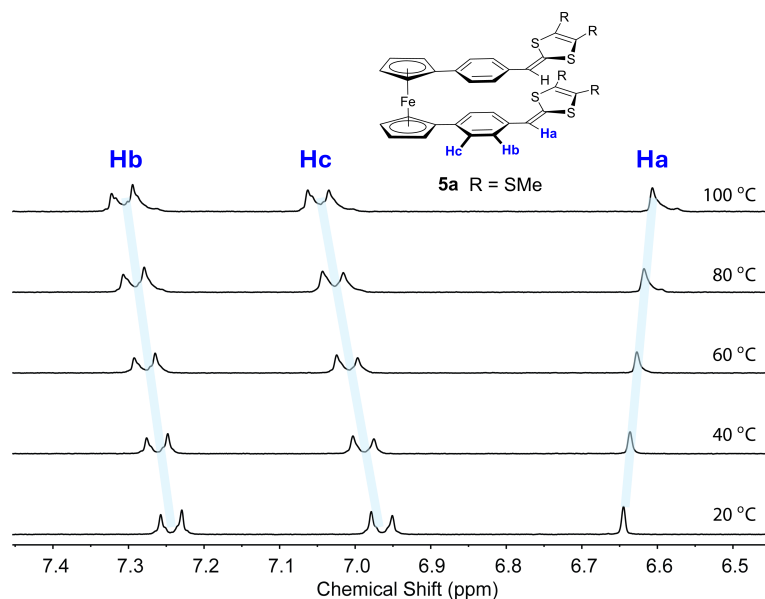


Figure 3.5: ^1H NMR (300 MHz, $\text{DMF-}d_6$) spectra of **5a** showing its phenylene and vinylic proton signals measured at different temperatures.

at about 8 ps of MD simulation time (Figure 3.6A and B), showing a partially opened conformation (Figure 3.6F). Conformers that display a fully *trans* geometry, however, were not observed during the entire MD simulation period. At room temperature (i.e., 298 K), the MD trajectory of **5a** features a much smaller degree of structural fluctuation in comparison with that simulated at 398 K. The plots of D_1 and D_2 values in Figure 3.6C and D indicate that the conformations of **5a** at 298 K are predominantly *cis* with the intermolecular π -stacking among the phenylene and dithiole rings barely disrupted.

According to the MD simulations, the VT-NMR results of **5a** can be explained as follows. At room temperature (298 K), *cis* conformers are dominantly present in the solution of **5a**. The phenylene groups in the molecule of **5a** are thus slipped stacked one another, delivering anisotropic shielding effects on protons **Hb** and **Hc**. When the

temperature is increased, some of the *cis* conformers are changed into partially opened conformers where the intramolecular π -stacking effects are weakened or eliminated. These changes in turn make **Hb** and **Hc** less shielded, so their signals are shifted to the downfield. In the *cis* conformation of **5a**, two DTF rings form slipped stacking. As such, each of the vinylic protons (**Ha**) is close to the electronegative sulfur atoms of the adjacent DTF group to experience some deshielding effects. When the conformation of **5a** is changed from *cis* to partially opened with increasing temperature, the deshielding effects are attenuated and the signal of **Ha** is consequently shifted toward the upfield.

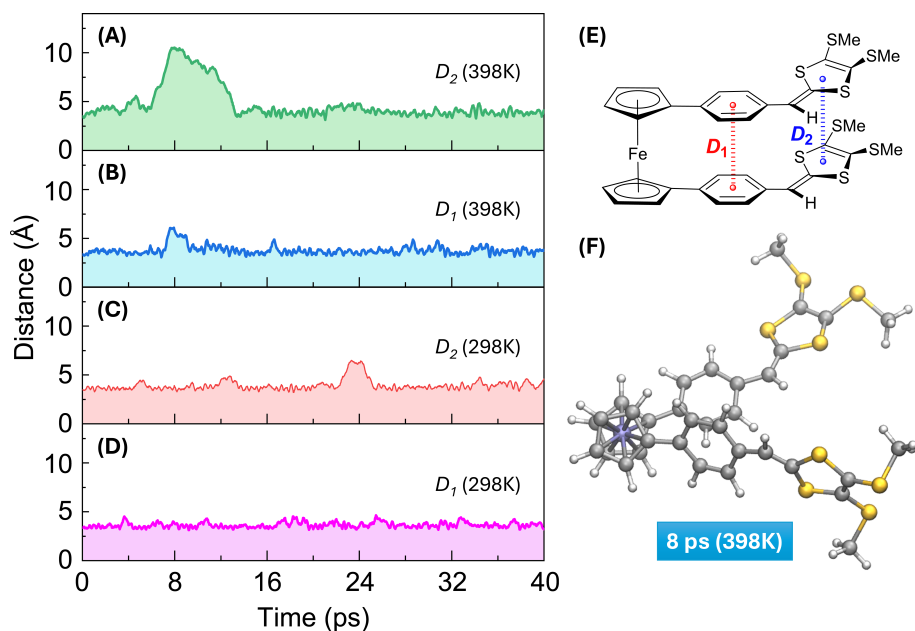


Figure 3.6: (A)–(D) Distances between the centroid positions of the two phenylene groups (D_1) and two dithiole groups (D_2) of **5a** as a function of MD simulation time at different temperatures. (E) Molecular structure of **5a** with the inter-ring distances D_1 and D_2 illustrated. (F) Simulation snapshot of **5a** taken at time = 8 ps, temperature = 398 K.

The CREST calculations of **5b** and **5c** predicted 63 and 11 low-energy conformers. Similar to the case of **5a**, all of the low-energy structures of **5b** and **5c** adopt *cis* or *cis*-like conformations. From the CREST results, DFT-optimized lowest-energy structures of **5b** and **5c** were obtained. In the lowest-energy conformer of *cis* **5b**, the two phenylene units show slipped stacking with an inter-centroid distance of 5.37 Å between the two phenyl rings (Figure 3.7A). Relative to the adjacent Cp ring, each of the phenylene groups shows a torsion angle of 32.7°, which is much larger than that of its *para*-isomer **5a**. The DTF units are nearly co-planar with the phenylene moieties which they are respectively connected with. The stacking between the two DTF groups in **5b** is slightly longer than **5a**. Compared with its *trans* conformer, the Gibbs energy of the optimized *cis* conformer of **5b** is lower by 6.86 kcal mol⁻¹. This result indicates that *cis* is the dominant conformation of **5b** in the solution phase.

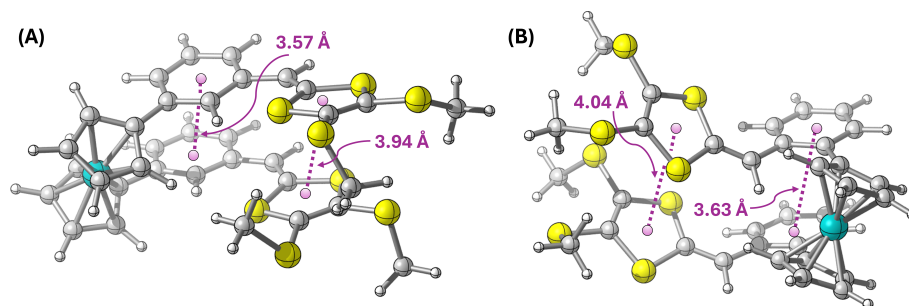


Figure 3.7: Optimized molecular structures of (A) *cis* **5b** and (B) *cis* **5c**. Inter-centroid distances between adjacent arene rings are highlighted.

The DFT-optimized geometry of **5c** also shows a *cis* conformation with slipped stacking between the two phenylene units as well as the two DTF groups (see Figure 3.7B). The *ortho*-substitution pattern in the structure of **5c** gives rise to increased steric clashing among the arene moieties in the molecule. As a result, the molecular

structure of *cis* **5c** is considerably more twisted than the optimized structures of **5a** and **5b**. It is noteworthy that the DTF groups of **5c** show a torsion angle of 41.6° with respect to the adjacent phenylene groups (see Figure 3.7B). The significantly twisted conformation of **5c** accounts for its relatively loose packing in the crystalline state. Actually, the DFT-optimized lowest-energy structure of **5c** bears resemblance to the structure determined by X-ray analysis, suggesting that the solid-state packing has a minor impact on the conformation of **5c**. The *cis* conformer of **5c** was calculated to be more stable than its *trans* conformer by $7.66 \text{ kcal mol}^{-1}$.

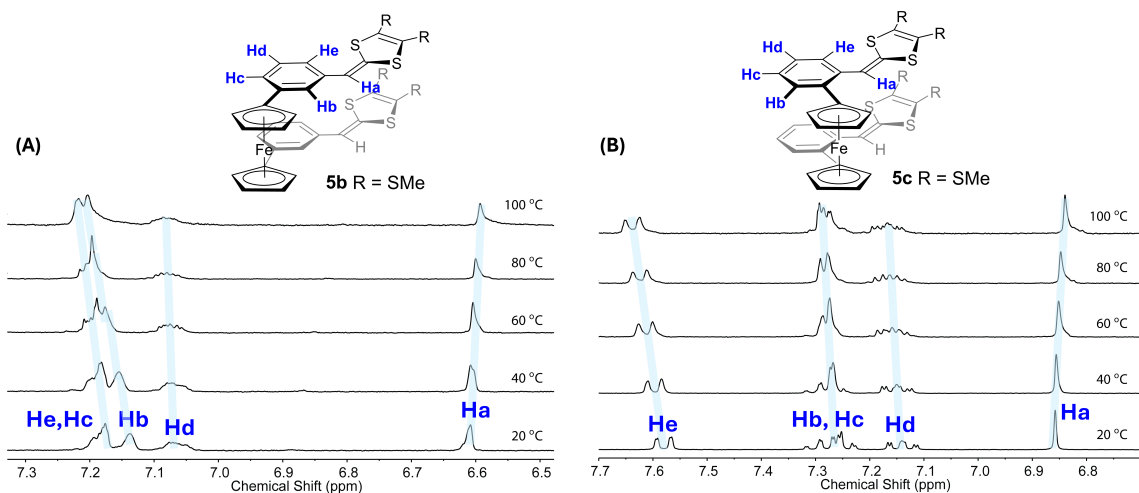


Figure 3.8: ^1H NMR (300 MHz, $\text{DMF-}d_6$) spectra of (A) **5b** and (B) **5c** showing their phenylene and vinylic proton signals measured at different temperatures.

VT-NMR spectra of **5b** and **5c** were also determined to further understand their conformational properties in the solution phase (see Figure 3.8). At room temperature, the ^1H NMR spectrum of **5b** shows a relatively broad singlet signal at 6.61 ppm, which is due to the vinylic proton (labelled as **Ha** in Figure 3.8A). The phenylene protons of **5b** give three groups of broad signals in the region of 7.03–7.22

ppm. The spectral patterns suggest that compound **5b** exists as a range of conformers at room temperature. With increasing temperature, the vinylic proton signal is slightly shifted to the upfield, while the phenylene proton signals show downfield shifts except that of **Hd**, which is the *meta* proton to both DTF and Fc groups. Of all the signals in the aromatic region, the phenylene proton **Hb** (*ortho* to both DTF and Fc groups) shows the most significant change with temperature, from 7.14 ppm at 20 °C to 7.20 ppm at 100 °C. In the meantime, the spectral lineshape of this signal is gradually narrowed and then merged with the signals of the other two phenylene protons **Hc** and **He** at elevated temperature. This result can be ascribed to accelerated rotation of the phenylene groups as well as an increasing population of partially opened conformers as the temperature is raised up.

Similar to the cases of **5a** and **5b**, the vinylic proton of **5c** (labelled as **Ha** in Figure 3.8B) shows an upfield shift and one of the phenylene protons **He** shows a downfield shift with increasing temperature. The phenylene proton **Hd** varies from a pattern of pseudo doublet of triplets (dt) to a complex multiplet (m), but its chemical shift (δ) is barely changed. The other two phenylene protons, **Hb** and **Hc**, gradually coalesce as the temperature is increased. Overall, the VT-NMR data of **5c** suggest that increased temperature results in not only the conversion of intermolecularly π -stacked *cis* conformers to partially opened conformers, but also the formation of complex rotamers due to accelerated rotation of its arene groups.

3.2.4 Electronic Absorption Properties of **5a–c**

The electronic absorption properties of (DTF)₂-Fc **5a–c** in the solution phase were investigated by UV-Vis spectroscopic analysis. As shown in Figure 3.9, compound **5a** gives a strong absorption band at 368 nm along with a relatively weak absorption tail ranging from 430 to 560 nm. According to time-dependent density functional theory (TD-DFT) calculations, the absorption band 368 arises from the $\pi \rightarrow \pi^*$ transitions that involve molecular orbitals populated at the phenylene–DTF moieties. The long-wavelength absorption tail is due to the $d-d$ transitions at the Fe(II) center and as well as transition from the from the d orbital of Fe(II) to the π -orbital at the phenylene–DTF arm (see Figure 5.34 in Appendix B for details). Compounds **5b** and **5c** show absorption peaks at 343 nm and 350 nm, respectively, which are both notably blueshifted relative to compound **5a**. The blueshifts can be explained by that compounds **5b** and **5c** are more twisted in shape and afford lesser degrees of π -conjugated than **5a**. It is noteworthy that the absorption peak of *meta*-substituted **5b** is slightly more blueshifted than *ortho*-substituted **5c**. This observation attests to that the *m*-phenylene bridge has the weakest effect on facilitating the electronic communications between the DTF and Fc groups.

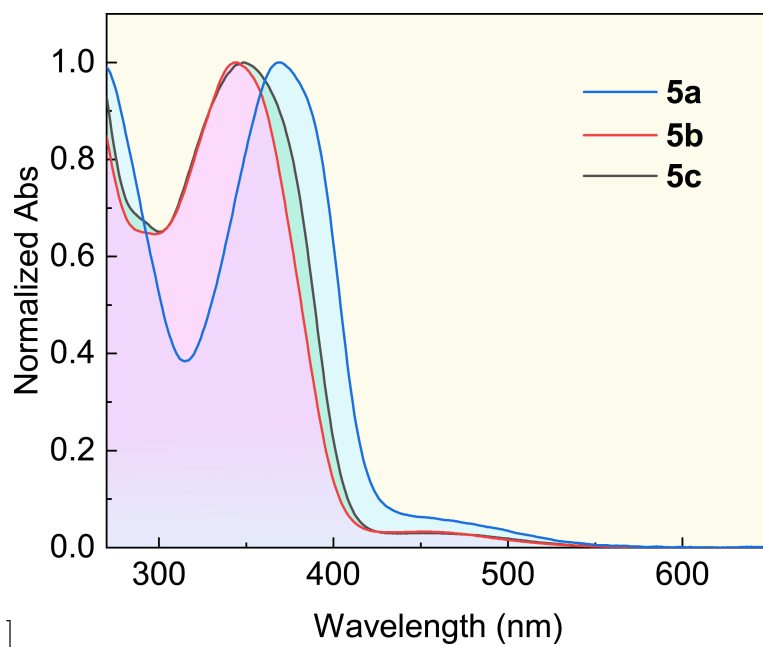


Figure 3.9: Normalized UV-Vis absorption spectra of **5a–c** measured in CH_2Cl_2 at room temperature.

3.2.5 Electrochemical Redox Properties of **5a–c**

The electrochemical redox properties of compounds **5a–c** were examined by cyclic voltammetric (CV) analysis. As shown in Figure 3.10A, the CV profile of **5a** displays three anodic peaks at +0.54 V, +0.72 V, and +1.02 V in the positive potential window, which are consistent with the presence of three electron-donating groups in the molecular structure. The oxidation of **5a** is believed to undergo stepwise single-electron transfers that take place in the two DTF groups and the Fc unit. The three anodic peaks observed in the CV profile of **5a** correspond to the formation of monocationic ($[\mathbf{5a}]^+$), dicationic ($[\mathbf{5a}]^{2+}$), and tricationic ($[\mathbf{5a}]^{3+}$) species, respectively. In the reverse scan, only two cathodic peaks at +0.61 V and 0.45 V are observed. It is therefore proposed that the reduction of $[\mathbf{5a}]^{3+}$ on the

electrode surface undergoes a simultaneous two-electron transfer and then a single electron transfer to reach neutrality.

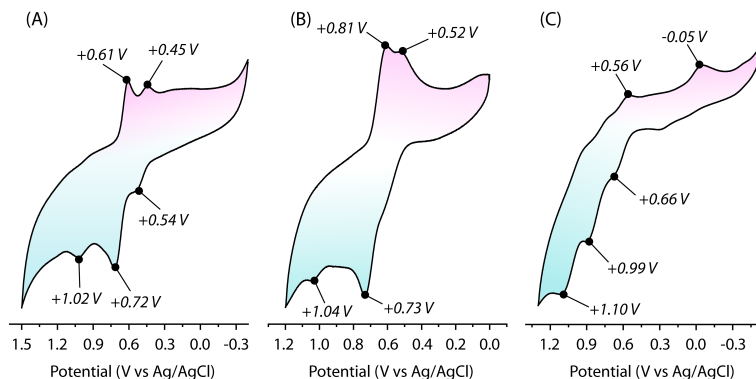


Figure 3.10: Cyclic voltammograms of (A) **5a**, (B) **5b**, and (C) **5c** measured in DMF at room temperature. Experimental conditions: glassy carbon as the working electrode, Ag/AgCl as the reference electrode, Pt wire as the counter electrode, Bu₄NPF₆ (0.1 M) as the electrolyte, and scan rate = 0.20 V/s.

To gain a deeper insight into the electronic properties of the oxidized forms of **5a**, DFT calculations of their electrostatic potential (ESP) maps, atomic charges, and electron spin density maps were conducted. Figure 3.11A shows the ESP map of monocationic **5a** in the *cis* conformation. According to DFT calculations, *cis*-[**5a**]⁺ is more stable than its *trans* counterpart by 20.8 kcal mol⁻¹, indicating that oxidization of **5a** into a radical cation actually results in more attractive π -stacking between the two phenylene-DTF arms. The ESP map of [**5a**]⁺ clearly shows that relatively high ESP values are located around one of the DTF groups (mapped with blue color), while relatively low ESP values are located around the Fc unit (mapped with red color). The ESP distribution indicates that the positive charge is mainly located at one of DTF rings. To further assess charge distribution properties, atomic charges of *cis*-

$[\mathbf{5a}]^+$ were computed using the atomic dipole moment corrected Hirshfeld (ADCH) population method.⁴⁵ As illustrated in Figure 3.11C, the atoms of the central Fc unit account for a total charge of +0.173, indicating that Fc is not significantly oxidized at this stage. One of the two phenylene–DTF arms shows a much higher positive charge (+0.675) than the other one (+0.152). The positive charge of *cis*- $[\mathbf{5a}]^+$ is therefore mainly populated in this phenylene–DTF segment.

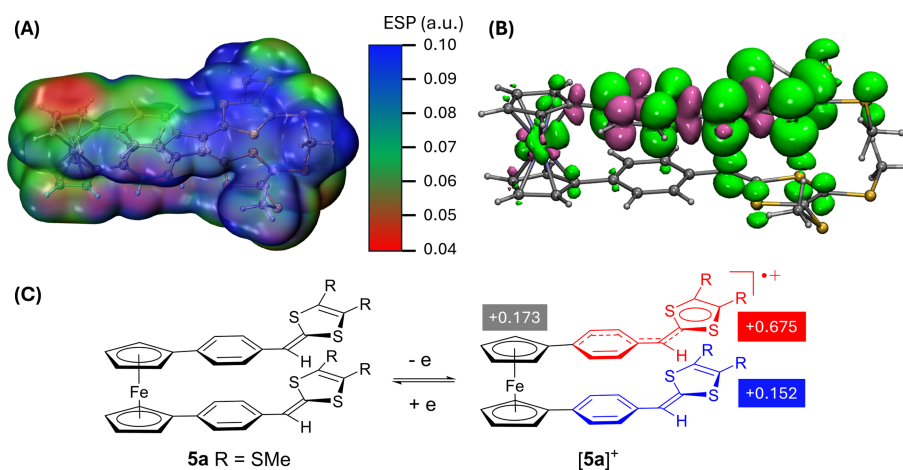


Figure 3.11: (A) ESP map of monocationic *cis*- $\mathbf{5a}$. (B) Isosurface map of the spin density (0.001 a.u.) distribution of monocationic *cis*- $\mathbf{5a}$. (C) Reaction scheme of the single-electron transfer taking place on *cis*- $\mathbf{5a}$. Colored text boxes give the total atomic charges (ΣQ) of the central Fc unit and two phenylene-DTF arms, respectively.

The monocation of *cis*- $\mathbf{5a}$ with an unpaired electron gives a spin multiplicity of doublet ($S = 2$). The spin density map of *cis*- $[\mathbf{5a}]^+$ discloses that the monoradical character is dominantly distributed in the phenylene–DTF segment that has a higher degree of positive charge (Figure 3.11B). The adjacent DTF group and the central Fc unit also show some spin density, but the magnitude is kind of weak. Collectively, the results of the ESP, atomic charge analysis, and spin density calculations suggest

that $[\mathbf{5a}]^+$ is formed by a single-electron transfer occurring at one of its DTF groups. The resulting radical and cationic characters are mainly delocalized along one of the phenylene–DTF arms as illustrated by the scheme given in Figure 3.11C.

The dication of $\mathbf{5a}$ in theory can have two electron spin configurations, namely singlet ($S = 1$) and triplet ($S = 3$). For the singlet state, the *cis* conformation of $[\mathbf{5a}]^{2+}$ is more stable than the *trans* by 23.0 kcal mol⁻¹ according to DFT calculations. Compared with the case of monocation, the singlet dication of $\mathbf{5a}$ shows increased preference for the *cis* conformation over the *trans*, which points to a beneficial effect of π -stacking between the two oppositely spinning radicals of DTF on stabilizing the singlet dication of $\mathbf{5a}$. The triplet dication of $\mathbf{5a}$ in the *cis* conformation is more stable than the singlet *cis* dication by 3.01 kcal mol⁻¹. The ESP map of singlet *cis*- $[\mathbf{5a}]^{2+}$ exhibits a charge distribution very different from its triplet counterpart (see Figure 3.12A and C). The Fc unit is less electropositive than the two DTF groups in the singlet state, but it turns to be more electropositive in the triplet state. Atomic charge analysis concurs with the ESP calculations, showing that the Fc unit of singlet *cis*- $[\mathbf{5a}]^{2+}$ possesses a lower charge of +0.444 in comparison with the charges distributed on the two phenylene–DTF arms (+0.778 for each). In the triplet state, the Fc unit takes a relatively high charge of +0.978, while each of the phenylene–DTF arms has a relatively low charge of +0.511. The singlet *cis*- $[\mathbf{5a}]^{2+}$ can therefore be deemed as two delocalized DTF radical cations, which are stacked in parallel to facilitate π -electron delocalization. For the triplet *cis*- $[\mathbf{5a}]^{2+}$, its biradical spin density is distributed across the entire π -conjugated framework of the molecule as revealed by the plot shown in Figure 3.13. The triplet dication of *cis*- $\mathbf{5a}$ can thus be described as the electronic configuration illustrated in Figure 3.12D, which includes a ferrocenium

radical cation and a mixed-valence (MV) radical cation distributed across two closely stacked phenylene–DTF moieties.

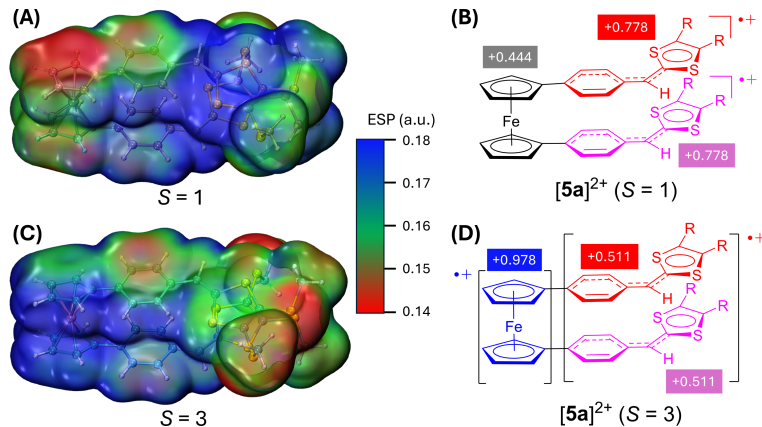


Figure 3.12: (A) ESP map of dicationic *cis*-**5a** and (B) its schematic drawing of charge distribution in the singlet ($S = 1$) state. (C) ESP map of dicationic *cis*-**5a** and (D) its schematic drawing of charge distribution in the triplet ($S = 3$) state. Colored text boxes give the total atomic charges (ΣQ) of the central Fc unit and two phenylene-DTF arms, respectively.

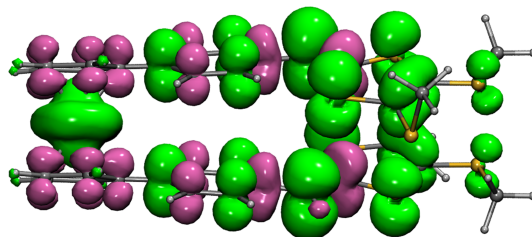


Figure 3.13: Isosurface map of the spin density (0.001 a.u.) distribution of *cis*-dicationic **5a** ($S = 3$).

Tricationic **5a** was also modeled in two different electron spin configurations—doublet ($S = 2$) and quartet ($S = 4$). In the the doublet spin state, the trication

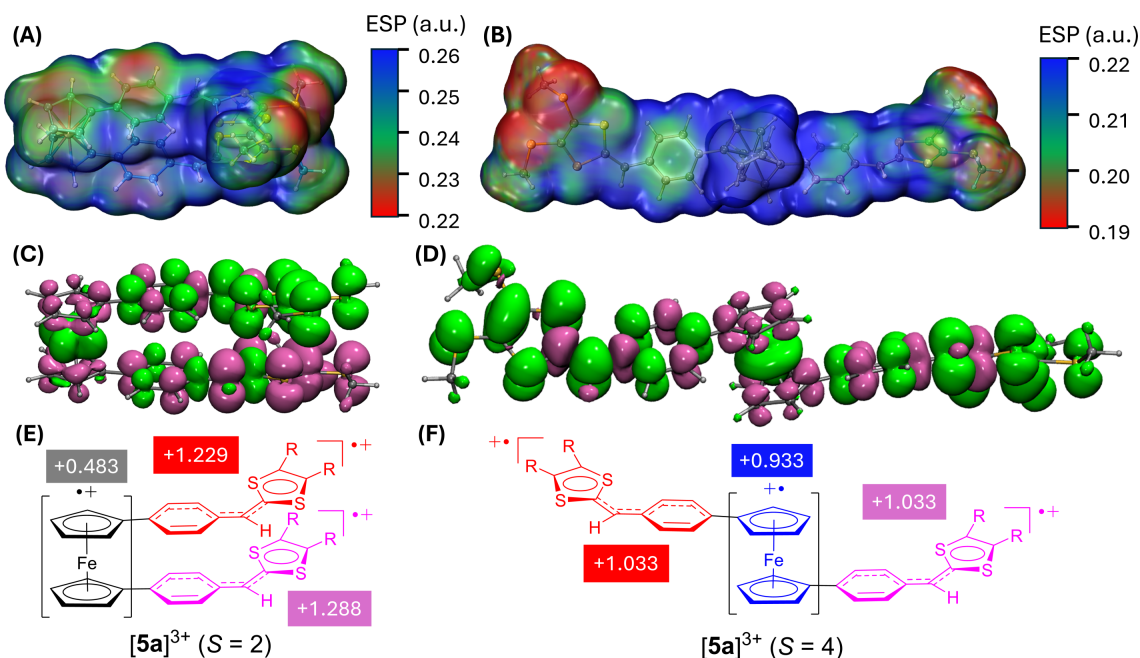


Figure 3.14: ESP maps of (A) *cis* tricationic **5a** ($S = 2$) and (B) *trans* tricationic **5a** ($S = 4$). Isosurface maps of the spin density (0.001 a.u.) distribution of (C) *cis* tricationic **5a** ($S = 2$) and (D) *trans* tricationic **5a** ($S = 4$).

of **5a** was found to favor a *cis* conformation. As shown in Figure 3.14A and E, the ESP map and atomic charge analysis of the doublet $[\mathbf{5a}]^{3+}$ reveal that the two DTF groups possess a higher electropositive character than the Fc group. Therefore, this trication has the positive charges mainly distributed in the two phenylene–DTF segments, which hold charges of +1.229 and +1.288, respectively. The Fc unit, on the other hand, shows a relatively low charge value of +0.483. For the quartet $[\mathbf{5a}]^{3+}$, the optimized geometry exhibits a *trans* conformation. Its ESP map and atomic charge analysis (Figure 3.14B and E) reveal that positive charges are evenly distributed along the central Fc group and the two phenylene–DTF arms. In this spin state, the π -stacking between the two DTF groups gives way to the electrostatic repulsion, driving the molecule to adopt a *trans* conformation instead of a *cis* one. It is also worth

mentioning that the doublet trication and quartet trication have nearly identical Gibbs energies, with the doublet being slightly more stable by 0.13 kcal mol⁻¹. The two spin states of [5a]³⁺ both show highly delocalized spin density, which contributes to their stabilization (see Figure 3.14C and D).

Overall, the DFT computational analysis allows the charge and electron spin properties of compound 5a in different oxidation states to be quantitatively evaluated. Based on these results, the CV profiles of compounds 5b and 5c can also be reasonably assigned and interpreted. The voltammogram of *meta*-substituted isomer 5b shows two anodic peaks at +0.73 V and +1.04 V in the forward CV scan (Figure 3.10B), which can be assigned to the sequential formation of dicationic and tricationic states. The formation of the monocation of 5b cannot be clearly observed in the CV profile, suggesting that the oxidation of 5b starts with a simultaneous two-electron transfer on the molecule rather than a single-electron transfer. This redox behavior is different from that of 5a. In compound 5b, the electronic communications between the two DTF groups through the central Fc unit are relatively weak due to the *meta*-substitution effect. As a result, the two DTF groups behave as two isolated electron donors and are hence oxidized at the same potential. In the reverse CV scan of 5b, there are two cathodic peaks at +0.81 and +0.52 V in the profile, which are similar to those of 5a.

The cyclic voltammogram of *ortho*-substituted 5c shows three distinct anodic peaks at +0.66 V, +0.99 V, and +1.10 V (Figure 3.10C). Like the case of 5a, the first two steps of oxidation taking place on 5c are due to the sequential single-electron transfers that lead to the formation of monocation and dication, respectively. Compared with the CV data of 5a, the first two oxidation potentials measured in the

CV profile of **5c** are shifted in the positive direction. Since the molecular structure of *ortho*-substituted **5c** carries more steric encumbrance between the DTF and Fc groups, the electron delocalization effect in **5c** is somewhat lowered, and the first two oxidation potentials are more positively shifted compared to those of **5a**. The reverse CV scan of **5c** gives two cathodic peaks at +0.56 V and -0.05 V. They are significantly lower than the cathodic peaks observed in the voltammograms of **5a** and **5b**. The exact reason for this unusual electrochemical behavior has not yet been clarified at this juncture. However, significant conformational changes associated with the reduction of the cations of **5c** are believed to play a role here. Further experimental and theoretical investigations on this point are therefore warranted.

3.2.6 Supramolecular Interactions of **5a** with γ -Cyclodextrin

In the field of supramolecular chemistry, Fc and its derivatives have been widely investigated as redox-responsive guests due to the robust electroactivity of Fc.^{6,46,47} Among various supramolecular hosts, cyclodextrins (CDs) are well known to favorably bind with Fc and Fc derivatives.⁴⁸⁻⁵² CDs are a class of macrocyclic oligosaccharides composed of multiple glucoside units.^{53,54} The number of glucoside units of a CD molecule determines the size of the non-polar cavity it possesses for host-guest inclusion. Commonly studied CDs are α -, β -, and γ -CDs, which are known to interact with Fc to form certain types of inclusion complexes; in particular, the size of β -CD matches Fc well to give 1:1 complexes.⁴⁸⁻⁵² It has also been reported that CDs can form inclusion complexes with electron-donating heterocyclic compounds such as thiophene⁵⁵ and tetrathiafulvalene (TTF).⁵⁶ In this light, we envisioned our (DTF)₂-

Fc derivatives would show supramolecular host-guest interactions with certain CD molecules. To shed more light on this respect, we further carried out investigation on the supramolecular interactions between *para*-substituted **5a** and γ -CD. We chose **5a** and γ -CD as guest and host molecules because of their matching molecular shapes and sizes. Figure 3.15 illustrates three possible binding modes for the complexation of **5a** with a CD host. If the Fc group or one of the DTF units is captured inside the CD cavity, a 1:1 complex is formed. The former complex (**5a₁**) should retain the *cis*-conformation of **5a**, while the latter one (**5a₂**) may adopt a multitude of conformations ranging from partially opened to a fully *trans* geometry. If the two DTF end groups both interact with CD molecules, then a 2:1 complex should be formed. The structure of **5a** encapsulated by two CD molecules (**5a₃**) should favor a *trans* conformation to avoid steric clashing.

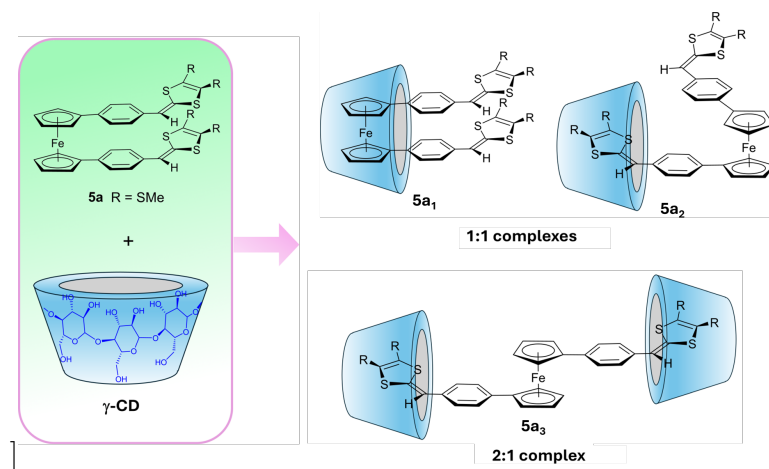


Figure 3.15: Proposed binding modes between **5a** and γ -CD.

To investigate the detailed supramolecular interactions between the (DTF)₂-Fc system and γ -CD, we first performed NMR analysis on a mixture of **5a** and γ -CD at

1:1 mole ratio in DMSO- d_6 . The resulting NMR spectrum shows three sharp signals at 7.11 (d, $J = 8.4$ Hz), 6.83 (d, $J = 8.4$ Hz), and 6.56 (s) ppm in the aromatic region, which are consistent with the phenylene and vinyl protons of free molecules of **5a** (Figure 3.16A). In the mean time, numerous new peaks arise in the aromatic region after mixing **5a** with γ -CD. Among them, two broad signals in the region of 7.15 to 7.43 ppm are prominent. These peaks are downfield shifted in comparison with the two phenylene proton signals of pristine **5a**. According to the VT-NMR analysis of **5a** (vide infra), the downfield shifts can be attributed to an increase in the population of conformers that take partially opened geometries after interacting with γ -CD.

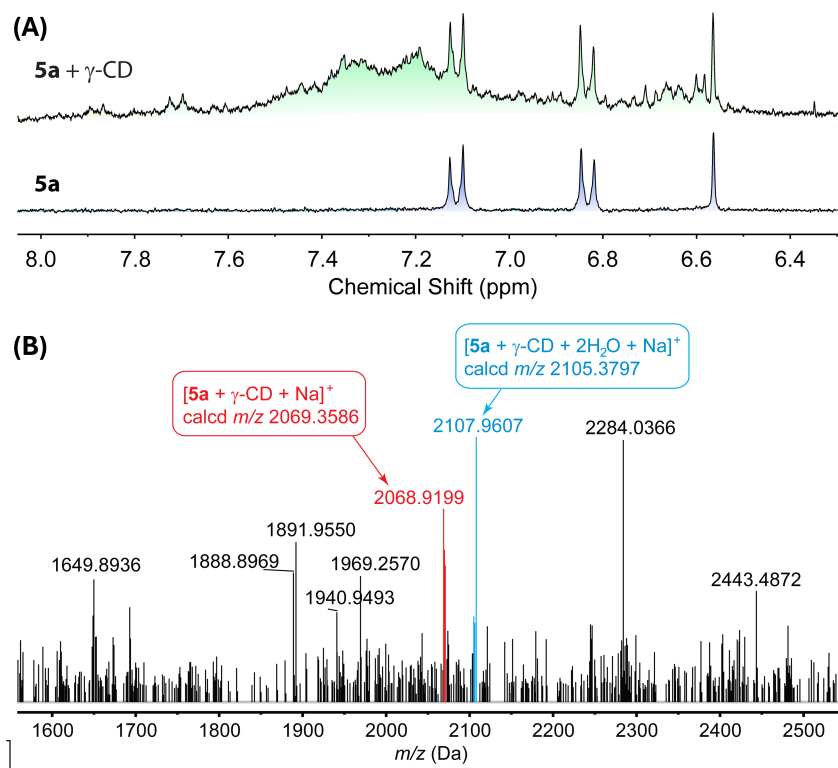


Figure 3.16: (A) Expanded ^1H NMR (300 MHz, $\text{DMSO-}d_6$) spectra of **5a** and a mixture of **5a** and γ -CD at 1:1 mole ratio. (B) MALDI-TOF mass spectrum measured from a mixture of **5a** and γ -CD. Mass peaks assigned to the molecular ions due to the 1:1 complex of **5a** and γ -CD are highlighted by red and cyan colors.

The binding ratio of **5a** with γ -CD in the solution phase was further determined by MALDI-TOF MS analysis. Figure 3.16B shows the mass data determined from a 1:1 (mole ratio) solution of **5a** and γ -CD in CH_2Cl_2 . In this spectrum, one can clearly see the molecular ions of the 1:1 complex of **5a** and γ -CD as labelled. There were no observation of any mass peaks corresponding to the 1:2 complexation of **5a** and γ -CD. Therefore, it is fair to assert that compound **5a** in the neutral state prefers to bind with one equivalent of γ -CD in the solution phase to form a 1:1 host-

guest complex. As for the detailed binding sites in this complex, we believe that the DTF inclusion mode is more favored than the Fc inclusion, which can be reasoned as follows. Supposing the Fc inclusion occurs dominantly, the conformation of **5a** included in γ -CD should retain the *cis* shape very similar to that of unbound **5a**. If this is the case, the NMR patterns of **5a**/ γ -CD in the aromatic region should not show such significant changes as observed. To validate this argument, we performed NMR analysis of a mixture of **5a** with β -CD, since β -CD has a smaller cavity than γ -CD and more selectively matches the Fc unit than the DTF group. Our experimental results showed that mixing **5a** with β -CD did not cause noticeable spectral changes in the aromatic region (see Figure 5.31 in Appendix B).

GFN2-xTB calculations were conducted to gain a deeper insight into the 1:1 binding properties of **5a** and γ -CD. Our modeling results concur with the deduction drawn from experimental observations. When the Fc unit is included in the CD cavity (i.e., Fc-inclusion mode), the structure of **5a** still keeps the *cis* conformation that shows intramolecular π -stacking among its two phenylene-DTF arms. In this way, the Fc-inclusion binding results in a stabilization energy (ΔE_b) of 7.24 kcal mol⁻¹. On the contrary, if the CD molecule encapsulates one of the phenylene-DTF moieties (DTF-inclusion mode), the conformation of **5a** is changed from *cis* to a wedge-shaped geometry with the intramolecular π -stacking of the two phenylene-DTF arms completely lost. As a result, the stabilization energy of the DTF-inclusion mode is only 0.582 kcal mol⁻¹, since this binding mode requires extra energy to break up the π -stacking. The binding energies of these two complexes cannot accurately reflect their proportional distributions at equilibrium. Binding free energies are more suitable for this analysis, but it is expensive to conduct free energy calculations on

such a large system. To circumvent this barrier, we evaluated the kinetic stability of these two binding modes by MD simulations. Figure 3.17A compares the root mean square deviation (RMSD) plots calculated from the MD trajectories of the 1:1 Fc-inclusion and DTF-inclusion complexes, respectively. As can be seen that the two complexes retain stability in the first 1.5 ps of MD time. At about 1.6 ps, the Fc-inclusion mode shows clear dissociation (see Figure 3.17B), but the DTF-inclusion still retains the binding. The results of MD simulations indicate that the DTF-inclusion mode is kinetically more stable, which can be attributed to the steric crowding of the wedge-shaped conformation of **5a** in this binding mode. Together, our experimental and MD simulation results point to a shared conclusion; that is, one of the DTF end groups of **5a** is trapped inside the cavity of γ -CD. This type of supramolecular interaction in turn disrupts the intramolecular π -stacking of *cis*-**5a**, leading to the formation of partially opened conformers which are observable by NMR analysis. In the sense of conformational control, inclusion of **5a** into γ -CD provides a supramolecular means to partially open the *cis*-conformer of **5a** in the solution phase.

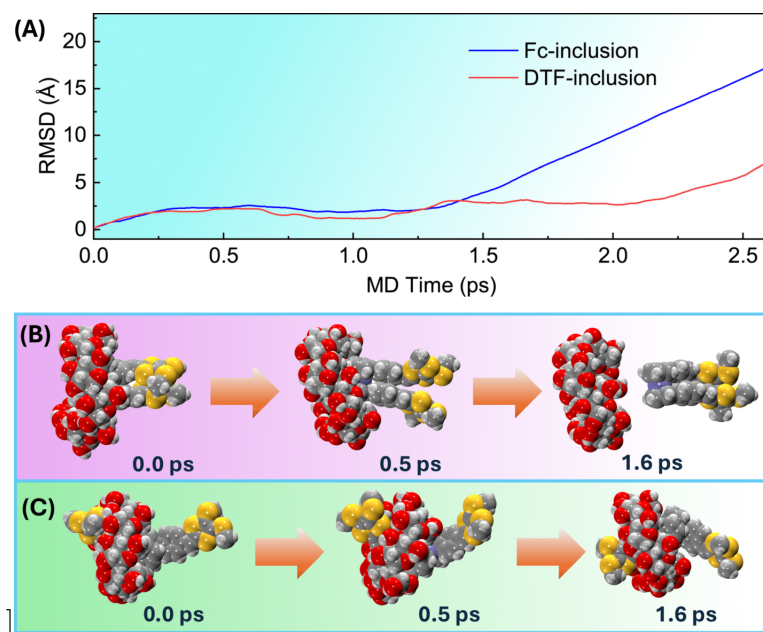


Figure 3.17: (A) RMSD plots of the 1:1 complexes of **5a** and γ -CD in DMF at 298 K. Snapshots taken during the MD simulations of the complexes in the (B) Fc-inclusion mode and (C) DTF-inclusion mode.

Next, we investigated the supramolecular interactions of γ -CD with **5a** in the oxidized state(s). Prior to this study, the reactivity of **5a** in various oxidation states was assessed by multi-cycle CV scans in the positive potential window (see Figure 3.18A). The voltammograms of **5a** measured from different scan cycles show insignificant variations, confirming that **5a** is lack of the common reactivity of DTF oxidative coupling as described in Scheme 3.1B. With this property determined, we subsequently performed a CV titration experiment, where **5a** was titrated with γ -CD from 0.0 to 4.0 mole equivalents (Figure 3.18B). The titration results show that the current intensity of each anodic and cathodic peak gradually decreases with increasing addition of γ -CD. This trend is attributable to the formation of inclusion complexes of

5a and γ -CD as they have lower diffusion coefficients than pristine **5a**. The potential of each redox peak in the voltammograms, however, does not vary significantly with increasing addition of γ -CD. Given that the cathodic peaks in the reverse scan are barely changed in the multi-cycle CV analysis, we chose to use the current intensity of the second cathodic peak at $E_{pc}^2 = +0.61$ V as a metric to evaluate the binding of oxidized **5a** with γ -CD. The outcome is illustrated in Figure 3.18C, in which the attenuation of the current intensity at E_{pc}^2 shows a nonlinear correlation with the mole ratio of γ -CD. The change in current intensity can be well fitted by a mono-exponential equation, alluding to a scenario where 1:1 binding is the dominant mode. Nevertheless, the binding of oxidized **5a**, particularly tricationic **5a**, with two equivalents of γ -CD is still anticipated to be possible, considering that [**5a**]³⁺ in the quartet spin state ($S = 4$) favors a fully opened *trans* conformation (vide supra). To delve into this aspect, we carried out an experiment as schematically illustrated in Figure 3.18D. Herein, compound **5a** was first oxidized with iodine in CH₂Cl₂ and then allowed to interact with an excess amount of γ -CD. The resulting mixture was reduced by Na₂S₂O₃ and then subjected to MALDI-TOF MS analysis to detect the formation of any inclusion complexes. As shown in Figure 3.18E, the formation of a 2:1 complex of γ -CD and **5a** is clearly evidenced by its molecular ion peak observed at m/z 3060 Da. It is also noteworthy that the mass spectrum shows a range of mass peaks that are evenly spaced by 74 Da. This mass pattern is due to the consecutive loss of a C₃H₆O₂ segment from the CD molecules bound to **5a**.

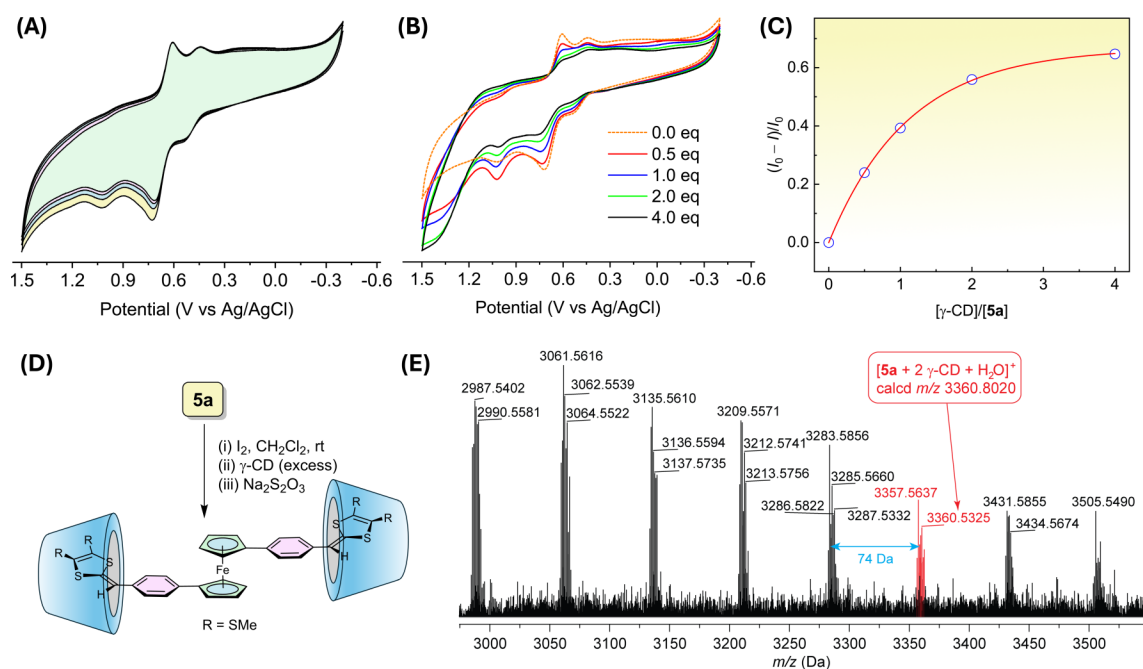


Figure 3.18: (A) Multi-cycle CV scans of **5a** in DMF. (B) Cyclic voltammograms monitoring the titration of **5a** (0.10 mM) with γ -CD (from 0 to 4.0 mole equiv) in DMF. (C) Current responses of the cathodic peak at +0.61 V (vs Ag/AgCl) to the addition of CD. I_0 and I are the current intensities before and during the titration. (D) Formation of a 2:1 complex of γ -CD and **5a** under oxidative conditions. (E) MALDI-TOF mass spectrum showing the molecular ion of the 2:1 complex of γ -CD and **5a** (highlighted by red color).

3.3 Conclusions

In this work, we have synthesized and characterized three new 1,1'-disubstituted Fc derivatives **5a–c**, which contain *para*-, *meta*-, and *ortho*-substituted DTF-phenylene arms, respectively. The molecular structures and conformational properties of these (DTF)₂-Fc compounds were examined by single crystal X-ray diffraction analysis, DFT calculations, and MD simulations. Intramolecular π -stacking between the two

phenylene–DTF segments provides a significant driving force for individual molecules of (DTF)₂–Fc to favor the *cis* conformation. Upon solid-state aggregation, *para*-substituted **5a** adopts a *trans* conformation that allows for efficient crystal packing. This scenario can be viewed as trapping the relatively unstable *trans* conformer through crystal lattice confinement. Elevated temperature promotes the (DTF)₂–Fc system to partially open in the solution phase, which has been corroborated by VT-NMR analysis and MD simulations. CV studies indicate that *para*- and *ortho*-substituted compounds (**5a** and **5c**) undergo stepwise single-electron transfers upon electrochemical oxidation, resulting in monocationic, dicationic, and tricationic species consecutively. The oxidation of *meta*-substituted **5b**, however, begins with a simultaneous two-electron transfer on its two DTF groups and then a single-electron transfer to a fully oxidized (tricationic) state. To understand their detailed electronic and conformational properties, DFT modeling was performed on **5a**, which best represents our design concept of Fc-hinged molecular switches. In the oxidation states, intramolecular π -stacking between the two DTF–phenylene arms of **5a** mainly delivers attractive forces to make the system favor the *cis* conformation. Only at the tricationic quartet spin state, the molecular structure of **5a** favors a fully opened *trans* conformation. This results suggest that our designed (DTF)₂–Fc system has the potential to achieve redox-controlled conformational switching from *cis* to *trans* in a high oxidation state.

Since *para*-substituted **5a** possesses the molecular shape that is most suitable for acting as molecular tweezers, we further examined its formation of host-guest inclusion complexes with γ -CD and associated conformational changes. Our experimental results confirmed that γ -CD can interact with neutral **5a** to yield a 1:1 guest-host

complex in the solution phase. In this host-guest complexation, the DTF group of **5a** is a more favored binding site than the Fc unit. The binding of **5a** with γ -CD causes the structure of **5a** to switch from *cis* to partially opened conformations. Under oxidative conditions, cations of **5a** are able to bind with up to two equivalents of γ -CD to yield a 2:1 host-guest complex. This oxidation-inclusion sequence opens a bottom-up way to switch the conformation of the Fc₂-DTF system from *cis* to *trans* in a controlled manner. First, the *cis* conformation of Fc₂-DTF can be switched to *trans* through a full oxidation process. Then the molecule of *trans* Fc₂-DTF is trapped in two equivalents of γ -CD as a 2:1 inclusion complex. Overall, our studies have established a new family of Fc-based redox-responsive molecular building blocks that are expected to find intriguing applications in redox-responsive molecular devices and supramolecular assemblies.

3.3.1 Experimental Section

Materials and instrumentation

All reagents used were purchased from Sigma Aldrich or Alfa Aesar and used without further purification. All reactions were conducted in standard, dry glassware under an inert atmosphere of N₂ unless otherwise noted. Evaporation and concentration were carried out using a rotary evaporator operated under water aspirator pressure. Flash column chromatography was performed with 240–400 mesh silica gel, and thin-layer chromatography (TLC) was carried out with silica gel F254 covered on plastic sheets and monitored by UV light. Melting points (m.p.) were measured using an SRS OptiMelt melting point apparatus and are uncorrected.

^1H and ^{13}C NMR spectra were measured on a Bruker Avance III 300 MHz multinuclear spectrometer. Chemical shifts (δ) are reported in ppm and were referenced versus shifts of solvents containing residual protic impurities. Infrared spectra (IR) were recorded on a Bruker Alfa spectrometer. ESI-TOF MS analysis of compounds **3a–c** and **5a–c** was done on a GCT premier Micromass Technologies instrument. MALDI-TOF MS analysis was performed using a Bruker ultrafleXtreme MALDI-TOF/TOF analyser equipped with a reflector, delayed ion extraction, and (Nd:YAD) laser. 2,5-Dihydroxybenzoic acid (DHB) was used as the matrix for samples with sodium iodide (NaI) as cationizing agent. Preparation of the MALDI-TOF MS sample was done as follows. The matrix was dissolved in THF (10 mg/mL), the sample in CH_2Cl_2 (10 mg/mL), and the cationizing agent in THF (0.1 mol/L). The prepared solutions were then combined at a volumetric ratio of 20:3:1 and then deposited on a target plate for MS analysis.

UV/vis absorption spectra were recorded on a Varian Cary 6000i spectrophotometer. Cyclic voltammetric (CV) analysis was carried out in a standard three-electrode setup controlled by a BASi Epsilon potentiostat. Glassy carbon electrode was used as the working electrode, and its surface was polished by 1.0 micron alumina prior to CV scans. A Pt wire was used as the counter electrode, and the reference electrode was Ag/AgCl (3.0 M NaCl). All CV experiments were performed in CH_2Cl_2 and/or DMF media with Bu_4NBF_4 as the electrolyte.

Single crystal X-ray diffraction (SCXRD) analyses were performed on an XtaLAB Synergy-S, Dualflex, HyPix-6000HE diffractometer at 100(2) K, using Cu $K\alpha$ radiation ($\lambda = 1.5406 \text{ \AA}$). The data collection and reduction were processed within CrysAlisPro (Rigaku OD, 2019).

Synthetic procedures

Synthesis of 3a. A solution of ferrocenediboronic acid (**1**, 0.500 g, 1.83 mmol), 4-bromobenzaldehyde (**2a**, 0.845 g, 4.57 mmol), Pd(PPh₃)₄ (0.528 g, 10% mmol) and K₃PO₄ (1.16 g, 5.48 mmol) in THF/H₂O (6.0 mL, 3:1 v/v) was degassed under N₂ for 15 min. Then the reaction was stirred under N₂ and refluxed over 2 days. The reaction was allowed to cool down at rt. The reaction mixture was diluted with dichloromethane (100 mL) and then mixed with water (50 mL). The two layers were separated with a separation funnel. The aqueous layer was further extracted with dichloromethane (50 mL). The combined organic layers were dried over MgSO₄, filtered, and concentrated under reduced pressure. The residue was subjected to silica flash column chromatography using CH₂Cl₂ as the eluent to obtain pure **3a** (0.200 g, 0.507 mmol, 30%) as a dark orange solid. m.p. > 145 °C (dec). ¹H NMR (300 MHz, CDCl₃): δ 9.92 (s, 2H), 7.61 (d, *J* = 8.6 Hz, 4H), 7.30 (d, *J* = 8.2 Hz, 4H), 4.60 (t, *J* = 1.9, 4H), 4.36 (t, *J* = 1.9 Hz, 4H); ¹³C NMR (75 MHz, CDCl₃): δ 191.7, 145.0, 134.2, 130.0, 126.0, 84.3, 71.8, 68.6; FTIR (neat): 2921, 2795, 2721, 1775, 1684, 1597, 1482, 1214, 1170, 1035, 819, 528 cm⁻¹; HRMS (ESI-TOF, positive mode): *m/z* calcd for C₂₄H₁₈FeO₂ [M]⁺ 394.0656, found 394.0650.

Synthesis of 3b. The reaction was performed following the same procedures described in the synthesis of **3a**, using ferrocenediboronic acid (**1**, 0.350 g, 1.28 mmol), 3-bromobenzaldehyde (**2b**, 0.300 mL, 2.52 mmol), Pd(PPh₃)₄ (0.291, 10% mmol), and K₃PO₄ (0.815 g, 3.84 mmol) in THF/H₂O (6.0 mL, 3:1 v/v). Pure **3b** (100 mg, 0.254 mmol, 20%) was obtained as an orange solid after silica flash column chromatography

using CH₂Cl₂ and then EtOAc/CH₂Cl₂ (1: 99, v/v) as eluents. m.p. = 139–141 °C (dec). ¹H NMR (300 MHz, CDCl₃): δ 9.84 (s, 2H), 7.56 (dt, *J* = 7.5, 1.4 Hz, 2H), 7.51 (t, *J* = 1.4 Hz, 2H), 7.43–7.35 (m, 2H), 7.23 (t, *J* = 7.6 Hz, 2H), 4.59 (t, *J* = 1.9 Hz, 4H), 4.34 (t, *J* = 1.9 Hz, 4H); ¹³C NMR (75 MHz, CDCl₃): δ 192.4, 138.3, 136.6, 131.6, 129.1, 127.5, 126.2, 84.7, 70.8, 67.8; FTIR (neat): 3374, 2923, 2806, 2730, 1694, 1580, 1498, 1285, 1183, 818, 684, 645, 505 cm⁻¹; HRMS (ESI-TOF, positive mode): *m/z* calcd for C₂₄H₁₉FeO₂ [M+H]⁺ 395.0734, found 395.0723.

Synthesis of 3c. The reaction was performed following the same procedures described in the synthesis of **3a**, using ferrocenediboronic acid (**1**, 0.300 g, 1.10 mmol), 2-bromobenzaldehyde (**2c**, 0.30 mL, 2.52 mmol), Pd(PPh₃)₄ (0.291 g, 10% mmol), and K₃PO₄ (0.815 g, 3.84 mmol) in (6.0 mL, 3:1, v/v). Pure **3c** (205 mg, 0.520 mmol, 47%) was obtained as an orange solid after silica flash column chromatography using CH₂Cl₂ and then EtOAc/CH₂Cl₂ (1: 99, v/v) as eluents. m.p. > 124 °C (dec). ¹H NMR (300 MHz, CDCl₃): δ 10.32 (s, 2H), 7.81 (dd, *J* = 7.7, 1.7 Hz, 2H), 7.64 (dd, *J* = 7.7, 1.9 Hz, 2H), 7.41 (dt, *J* = 7.7, 1.7 Hz, 2H), 7.31 (d, *J* = 7.7 Hz, 2H), 4.49 (t, *J* = 1.9 Hz, 4H), 4.38 (t, *J* = 1.9 Hz, 4H); ¹³C NMR (75 MHz, CDCl₃): δ 192.3, 141.6, 134.5, 133.2, 131.6, 137.7, 126.8, 84.8, 72.7, 71.5; FTIR (neat): 3053, 2923, 2858, 1683, 1594, 1435, 1252, 1191, 1033, 820, 759, 633, 545 cm⁻¹; HRMS (ESI-TOF, positive mode): *m/z* calcd for C₂₄H₁₈FeO₂ [M]⁺ 394.0656, found 394.0640.

Synthesis of 5a. Compound **3a** (151 mg, 0.381 mmol) and compound **4** (260 mg, 1.15 mmol) were dissolved in P(OMe)₃ (3.0 mL) and heated to 110 °C for 9 h. The reaction was allowed to cool down. The resulting orange precipitate was filtrated

and rinsed with MeOH (10 mL). The crude **5a** was dissolved in CH₂Cl₂ (2 mL) and purified through silica column chromatography (CH₂Cl₂:hexane, 3:7 v/v), yielding pure **5a** (147 mg, 0.200 mmol, 51%) as an orange solid. m.p. > 185 °C (dec). ¹H NMR (300 MHz, CDCl₃): δ 7.14 (d, *J* = 8.4 Hz, 4H), 6.94 (d, *J* = 8.2 Hz, 4H), 6.42 (s, 2H), 4.50 (t, *J* = 1.9 Hz, 2H), 4.24 (t, *J* = 1.8 Hz, 2H), 2.452 (s, 6H), 2.447 (s, 6H). ¹³C NMR (75 MHz, CDCl₃): δ 135.2, 133.8, 130.6, 127.5, 126.9, 125.9, 124.3, 115.2, 86.2, 70.3, 67.5, 19.2, 19.0. FTIR (neat): 2918, 1603, 1571, 1492, 1415, 1277, 1084, 963, 841, 814, 511, 470 cm⁻¹; HRMS (ESI-TOF, positive mode): *m/z* calcd for C₃₄H₃₀FeS₈ [M]⁺ 749.9463, found 749.9455.

Synthesis of 5b. Compound **5b** was synthesized following the same procedures described in the synthesis of **3a**, using compound **3b** (85.0 mg, 0.216 mmol), compound **4** (200 mg, 0.881 mmol) in P(OMe)₃ (3.0 mL) at 110 °C for 24 h. The reaction mixture was then vacuum distilled to remove most of the unreacted P(OMe)₃. The residue was further purified by silica column chromatography (CH₂Cl₂/hexane, 3:7 v/v) to afford pure **5b** (80 mg, 0.107 mmol, 18%) as an orange solid. m.p. > 66.2°C (dec). ¹H NMR (300 MHz, CDCl₃): δ 7.15–7.10 (m, 2H), 7.08–6.94 (m, 6H), 6.38 (s, 2H), 4.49 (dd, *J* = 1.9 Hz, 4H), 4.27 (dd, *J* = 1.9 Hz, 4H), 2.48 (s, 6H), 2.42 (s, 6H); ¹³C NMR (75 MHz, CDCl₃): δ 137.4, 135.8, 131.3, 128.1, 127.1, 124.2, 123.3, 114.9, 85.8, 70.0, 67.7, 18.8, 18.6; FTIR (neat): 2990, 2915, 1595, 1497, 1417, 1309, 966, 888, 805, 683, 589, 489 cm⁻¹; HRMS (ESI-TOF, positive mode): *m/z* calcd for C₃₄H₃₀FeS₈ [M]⁺ 749.9463, found 749.9451.

Synthesis of 5c. Compound **5c** was synthesized following the same procedures described in the synthesis of **5a**, using **3c** (200 mg, 0.508 mmol) and **4** (460 mg, 2.03 mmol) in P(OMe)₃ (3.0 mL) at 110 °C for 12 h. The reaction mixture was then subjected to vacuum distillation to remove most of the unreacted P(OMe)₃. The residue was further purified by silica column chromatography (hexanes) to afford pure **5c** (100 mg, 1.13 mmol, 38%) as an orange solid. m.p. > 143.0 °C (dec). ¹H NMR (300 MHz, CDCl₃): δ 7.46 (dd, *J* = 7.7, 1.1 Hz, 2H), 7.25 (dd, *J* = 7.7, 1.4 Hz, 2H), 7.19 (dt, *J* = 7.8, 1.1 Hz, 2H), 7.07 (dt, *J* = 7.4, 1.4 Hz, 2H), 4.45 (t, *J* = 1.9 Hz, 4H), 4.28 (t, *J* = 1.9 Hz, 4H), 2.45 (m, 6H), 2.40 (m, 6H); ¹³C NMR (75 MHz, CDCl₃): δ 135.4, 134.7, 131.8, 130.6, 126.3, 124.2, 115.8, 86.9, 71.5, 70.4, 19.01, 18.96; FTIR (neat): 2915, 2700, 1685, 1571, 1487, 1429, 1214, 1011, 817, 752, 507 cm⁻¹; HRMS (ESI-TOF, positive mode): *m/z* calcd for C₃₄H₃₀FeO₂ [M+H]⁺ 750.9541, found 750.9481.

Preparation of 2:1 inclusion complex of γ -CD and 5a. Compound **5a** (10.0 mg, 1.33 mmol) was dissolved in CH₂Cl₂ (4 mL). To this solution was added I₂ (34.0 mg, 13.4 mmol). The mixture was stirred at room temperature for 40 min (the color of the solution was observed to change from orange to dark purple). Next, γ -CD (69.0 mg, 5.30 mmol) was added, stirring the solution at room temperature for 24 h. A saturated aq. NaS₂O₃ was then added to the reaction mixture and stirred for another 30 min (the solution color gradually changed from dark purple to orange). The organic layer was extracted with CH₂Cl₂ (2 × 5mL). The organic layer was collected and dried over MgSO₄. The resulting sample was subjected to MALDI-TOF MS analysis to detect the formation of inclusion complexes of γ -CD and **5a**.

Bibliography

- [1] Miller, S. A.; Tebboth, J. A.; Tremaine, J. F. 114. Di cyclo pentadienyliron. *J. Chem. Soc.* **1952**, 632–635.
- [2] Kealy, T. J.; Pauson, P. L. A New Type of Organo-Iron Compound. *Nature* **1951**, *168*, 1039–1040.
- [3] Heinze, K.; Lang, H. Ferrocene Beauty and Function. *Organomet.* **2013**, *32*, 5623–5625.
- [4] Astruc, D. Why is ferrocene so exceptional? *Eur. J. Inorg. Chem.* **2017**, *2017*, 6–29.
- [5] Štěpnička, P. Forever Young: the First Seventy Years of Ferrocene. *Dalton Trans.* **2022**, *51*, 8085–8102.
- [6] Guchhait, C.; Suriyaa, V.; Sahu, N.; Sarkar, S. D.; Adhikari, B. Ferrocene: An Exotic Building Block for Supramolecular Assemblies. *Chem. Commun.* **2023**, *59*, 14482–14496.
- [7] Hudson, R. D. A. Ferrocene polymers: current architectures, syntheses and utility. *J. Organomet. Chem.* **2001**, *637*, 47–69.
- [8] Atkinson, R. C. J.; Gibson, V. C.; Long, N. J. The syntheses and catalytic applications of unsymmetrical ferrocene ligands. *Chem. Soc. Rev.* **2004**, *33*, 313–328.
- [9] Saleem, M.; Yu, H.; Wang, L.; Khalid, H.; Akram, M.; Abbasi, N. M.; Huang, J.

- Review on synthesis of ferrocene-based redox polymers and derivatives and their application in glucose sensing. *Anal. Chim. Acta* **2015**, *876*, 9–25.
- [10] Scottwell, S.; Crowley, J. D. Ferrocene-containing non-interlocked molecular machines. *Chem. commun.* **2016**, *52*, 2451–2464.
- [11] Larik, F. A.; Saeed, A.; Fattah, T. A.; Muqadar, U.; Channar, P. A. Recent advances in the synthesis, biological activities and various applications of ferrocene derivatives. *Appl. Organomet. Chem.* **2017**, *31*, e3664.
- [12] Holm, C. H.; Ibers, J. A. NMR Study of Ferrocene, Ruthenocene, and Titanocene Dichloride. *J. Chem. Phys.* **1959**, *30*, 885–888.
- [13] Seibold, E. A.; Sutton, L. E. Structure of Ferrocene. *J. Chem. Phys.* **1955**, *23*, 1967–1967.
- [14] Bohn, R. K.; Haaland, A. On the Molecular Structure of Ferrocene, $\text{Fe}(\text{C}_5\text{H}_5)_2$. *J. Organomet. Chem.* **1966**, *5*, 470–476.
- [15] Haaland, A.; Nilsson, J. E. The Determination of the Barrier to Internal Rotation in Ferrocene and Ruthenocene by Means of Electron Diffraction. *Chem. Commun.* **1968**, 88–89.
- [16] Li, C.; Medina, J. C.; Maguire, G. E. M.; Abel, E.; Atwood, J. L.; Gokel, G. W. Neutral Molecule Receptor Systems Using Ferrocene's "Atomic Ball Bearing" Character as the Flexible Element. *J. Am. Chem. Soc.* **1997**, *119*, 1609–1618.
- [17] Shoji, O.; Okada, S.; Satake, A.; Kobuke, Y. Coordination Assembled Rings of Ferrocene-bridged Trisporphyrin with Flexible Hinge-like Motion: Selective

- Dimer Ring Formation, Its Transformation to Larger Rings, and Vice Versa. *J. Am. Chem. Soc.* **2005**, *127*, 2201–2210.
- [18] Sivaev, I. B. Ferrocene and Transition Metal Bis(dicarbollides) as Platform for Design of Rotatory Molecular Switches. *Molecules* **2017**, *22*, 2201.
- [19] Torrance, J. B. The Difference Between Metallic and Insulating Salts of Tetracyanoquinodimethone (TCNQ): How to Design an Organic Metal. *Acc. Chem. Res.* **1979**, *12*, 79–86.
- [20] Devic, T.; Yuan, M.; Adams, J.; Fredrickson, D. C.; Lee, S.; Venkataraman, D. The Maximin Principle of π -Radical Packings. *J. Am. Chem. Soc.* **2005**, *127*, 14616–14627.
- [21] Preuss, K. E. Pancake Bonds: π -Stacked Dimers of Organic and Light-Atom Radicals. *Polyhedron* **2014**, *79*, 1–15.
- [22] Kertesz, M. Pancake Bonding: an Unusual pi-Stacking Interaction. *Chem. Eur. J.* **2019**, *25*, 400–416.
- [23] Bhattacharjee, R.; Jarvis, H.; McCormack, M. E.; Petrukhina, M. A.; Kertesz, M. Structure and Bonding in π -Stacked Perylenes: The Impact of Charge on Pancake Bonding. *J. Am. Chem. Soc.* **2024**, *146*, 10465–10477.
- [24] Iordache, A.; Oltean, M.; Milet, A.; Thomas, F.; Baptiste, B.; Saint-Aman, E.; Bucher, C. Redox control of rotary motions in ferrocene-based elemental ball bearings. *J. Am. Chem. Soc.* **2012**, *134*, 2653–2671.

- [25] Takai, A.; Yasuda, T.; Ishizuka, T.; Kojima, T.; Takeuchi, M. A Directly Linked Ferrocene–Naphthalenediimide Conjugate: Precise Control of Stacking Structures of π -Systems by Redox Stimuli. *Angew. Chem. Int. Ed.* **2013**, *52*, 9167–9171.
- [26] Tsujimoto, Y.; Sakurai, T.; Ono, Y.; Nagano, S.; Seki, S. Cold Crystallization of Ferrocene-hinged π -Conjugated Molecule Induced by the Limited Conformational Freedom of Ferrocene. *J. Phys. Chem. B* **2019**, *123*, 8325–8332.
- [27] Wang, W.; Ma, N.; Sun, S.; Qiu, Y. Impact of Redox Stimuli on Ferrocene–Buckybowl Complexes: Switchable Optoelectronic and Nonlinear Optical Properties. *Organomet.* **2014**, *33*, 3341–3352.
- [28] Wang, W. Y.; Ma, N.; Wang, L.; Zhu, C. L.; Fang, X.; Qiu, Y. Effect of π -Conjugate Units on the Ferrocene-based Complexes: Switchable Second Order Nonlinear Optics Controlled by Redox Stimuli. *Dyes Pigm.* **2016**, *126*, 29–37.
- [29] Uemura, T.; Naka, K.; Chujo, Y. Functional Macromolecules with Electron-donating Dithiafulvene Unit. *New Synth. Methods* **2004**, 81–106.
- [30] Alías, S.; Andreu, R.; Blesa, M.; Franco, S.; Garín, J.; Gragera, A.; Orduna, J.; Romero, P.; Villacampa, B.; Allain, M. Synthesis, Structure, and Optical Properties of 1,4-Dithiafulvene-based Nonlinear Optic-phores. *J. Org. chem.* **2007**, *72*, 6440–6446.
- [31] Åxman Petersen, M.; Zhu, L.; Jensen, S. H.; Andersson, A. S.; Kadziola, A.; Kilså, K.; Brøndsted Nielsen, M. Photoswitches Containing a Dithiafulvene Electron Donor. *Adv. Funct. Mater.* **2007**, *17*, 797–804.

- [32] Zhao, Y.; Chen, G.; Mulla, K.; Mahmud, I.; Liang, S.; Dongare, P.; Thompson, D. W.; Dawe, L. N.; Bouzan, S. Tetrathiafulvalene Vinylogues as Versatile Building Blocks for New Organic Materials. *Pure Appl. Chem.* **2012**, *84*, 1005–1025.
- [33] Abdollahi, M. F.; Zhao, Y. Recent Advances in Dithiafulvenyl-functionalized Organic Conjugated Materials. *New J. Chem.* **2020**, *44*, 4681–4693.
- [34] Britt, L. H.; Eradeh, R.; Leung, C.; Zhao, Y. DFT Investigations of Phenylthiafulvene Dimers at Different Oxidation States. *Phys. Chem. Chem. Phys.* **2023**, *25*, 33159–33168.
- [35] Hapiot, P.; Lorcy, D.; Tallec, A.; Carlier, R.; Robert, A. Mechanism of Dimerization of 1,4-Dithiafulvenes into TTF Vinylogues. *J. Phys. Chem.* **1996**, *100*, 14823–14827.
- [36] Christensen, C. A.; Batsanov, A. S.; Bryce, M. R. Thiolated π -Extended Tetrathiafulvalenes: Versatile Multifunctional π -Systems. *J. Org. Chem.* **2007**, *72*, 1301–1308.
- [37] Chen, G.; Mahmud, I.; Dawe, L. N.; Daniels, L. M.; Zhao, Y. Synthesis and Properties of Conjugated Oligoene-centered π -Extended Tetrathiafulvalene Analogues and Related Macromolecular Systems. *J. Org. Chem.* **2011**, *76*, 2701–2715.
- [38] Pracht, P.; Bohle, F.; Grimme, S. Automated Exploration of the Low-Energy Chemical Space with Fast Quantum Chemical Methods. *Phys. Chem. Chem. Phys.* **2020**, *22*, 7169–7192.

- [39] Pracht, P.; Grimme, S.; Bannwarth, C.; Bohle, F.; Ehlert, S.; Feldmann, G.; Gorges, J.; Müller, M.; Neudecker, T.; Plett, C. CREST—A Program for the Exploration of Low-Energy Molecular Chemical Space. *J. Chem. Phys.* **2024**, *160*.
- [40] Chai, J.; Head-Gordon, M. Long-Range Corrected Hybrid Density Functionals with Damped Atom-Atom Dispersion Corrections. *Phys. Chem. Chem. Phys.* **2008**, *10*, 6615–6620.
- [41] Chai, J.; Head-Gordon, M. Systematic Optimization of Long-Range Corrected Hybrid Density Functionals. *J. Chem. Phys.* **2008**, *128*.
- [42] Schäfer, A.; Huber, C.; Ahlrichs, R. Fully Optimized Contracted Gaussian Basis Sets of Triple Zeta Valence Quality for Atoms Li to Kr. *J. Chem. Phys.* **1994**, *100*, 5829–5835.
- [43] Johnson, E. R.; Keinan, S.; Mori-Sánchez, P.; Contreras-García, J.; Cohen, A. J.; Yang, W. Revealing Noncovalent Interactions. *J. Am. Chem. Soc.* **2010**, *132*, 6498–6506.
- [44] Bannwarth, C.; Ehlert, S.; Grimme, S. GFN2-xTB—An Accurate and Broadly Parametrized Self-consistent Tight-Binding Quantum Chemical Method with Multipole Electrostatics and Density-dependent Dispersion Contributions. *J. Chem. Theor. Comput.* **2019**, *15*, 1652–1671.
- [45] Lu, T.; Chen, F. Atomic Dipole Moment Corrected Hirshfeld Population Method. *J. Theor. Comput. Chem.* **2012**, *11*, 163–183.

- [46] Peng, L.; Feng, A.; Huo, M.; Yuan, J. Ferrocene-based Supramolecular Structures and Their Applications in Electrochemical Responsive Systems. *Chem. Commun.* **2014**, *50*, 13005–13014.
- [47] Sharma, S.; Rathore, K. Stimuli Responsive Ferrocene-based Supramolecular Systems: New Route for the Design of Smart Devices. *J. Organomet. Chem.* **2023**, *997*, 122787.
- [48] Isnin, R.; Salam, C.; Kaifer, A. E. Bimodal Cyclodextrin Complexation of Ferrocene Derivatives Containing n-Alkyl Chains of Varying Length. *J. Org. Chem.* **1991**, *56*, 35–41.
- [49] Menger, F. M.; Sherrod, M. J. Docking calculations on ferrocene complexation with cyclodextrins. *J. Am. Chem. Soc.* **1988**, *110*, 8606–8611.
- [50] Osella, D.; Carretta, A.; Nervi, C.; Ravera, M.; Gobetto, R. Inclusion Complexes of Ferrocenes and β -Cyclodextrins. Critical Appraisal of the Electrochemical Evaluation of Formation Constants. *Organomet.* **2000**, *19*, 2791–2797.
- [51] Casas-Solvas, J. M.; Ortiz-Salmerón, E.; Fernández, I.; García-Fuentes, L.; Santoyo-González, F.; Vargas-Berenguel, A. Ferrocene- β -cyclodextrin Conjugates: Synthesis, Supramolecular Behavior, and Use as Electrochemical Sensors. *Chem. Eur. J.* **2009**, *15*, 8146–8162.
- [52] Kasprzak, A.; Koszytkowska-Stawińska, M.; Nowicka, A. M.; Buchowicz, W.; Poplawska, M. Supramolecular Interactions between β -Cyclodextrin and the Nucleobase Derivatives of Ferrocene. *J. Org. Chem.* **2019**, *84*, 15900–15914.

- [53] Szejtli, J. Introduction and General Overview of Cyclodextrin Chemistry. *Chem. Rev.* **1998**, *98*, 1743–1754.
- [54] Del Valle, E. M. Cyclodextrins and Their Uses: A Review. *Proc. Biochem.* **2004**, *39*, 1033–1046.
- [55] Takashima, Y.; Sakamoto, K.; Oizumi, Y.; Yamaguchi, H.; Kamitori, S.; Harada, A. Complex Formation of Cyclodextrins with Various Thiophenes and Their Polymerization in Water: Preparation of Poly-pseudo-rotaxanes Containing Poly(thiophene)s. *J. Incl. Phenom. Macrocycl. Chem.* **2006**, *56*, 45–53.
- [56] Schröder, H. V.; Schalley, C. A. Tetrathiafulvalene—a Redox-switchable Building Block to Control Motion in Mechanically Interlocked Molecules. *Beilstein J. Org. Chem.* **2018**, *14*, 2163–2185.

Chapter 4

Conclusions and Future Work

This MSc thesis investigated the application of iron compounds in two distinct projects. The research has yielded significant insights into the catalytic behavior of iron complexes in the production of environmentally friendly polymers and the redox-controlled switchability of ferrocene-hinged molecular devices.

In the first project (Chapter 2), four iron(III) amino-(bis)phenolate complexes (**1a–d**) were successfully synthesized and characterized. These complexes demonstrated effective catalytic activity in the polymerization of *rac*-Lactide, with **1c** exhibiting the highest activity due to its more Lewis acidic iron center. Various reaction parameters for *rac*-lactide polymerization under the catalysis of complexes **1a–d** have been systematically examined, including reaction time, catalyst loading, reaction temperature, choice of co-catalyst and initiator. The results point to promising application of the iron amino-(bis)phenolate complexes as effective catalysts for lactide polymerization. Experimental results showed that satisfactory conversion efficiency for PLA could still be achieved at relatively low catalyst loading (0.5%). Temperature

is a crucial reaction parameter for the polymerization. Experimental results indicated that running the polymerization at 80 °C led to high conversions. Lower temperatures caused the conversions to decrease, but could make the molecular weights of the polymers increased to some extent. Therefore, there is still room for optimizing the reaction temperature to strike a balance between high conversion and good polymer quality. In the future work, there is another intriguing factor that can be introduced to the polymerization conditions for improving molecular weights, which is to combine PLA with other materials, such as phthalic anhydride.¹ At low catalyst loading, the iron complex-catalyzed polymerization reactions were determined to show a first-order kinetic behavior, depending on the monomer concentration. The kinetic behavior at high catalyst loading has not been elucidated and needs to be studied in future work. Moreover, the effects of room temperature on the P_r value are worth further investigation.²

In the second project (Chapter 3), a series of reactions such as Suzuki-Miyaura cross-coupling and phosphitepromoted olefination have been carried out to generate a new family of $(DTF)_2$ -Fc derivatives. Following the synthetic work, a series of advanced instrumental analyses have been conducted using NMR, mass spectrometry, IR, UV-Vis absorption spectroscopy, X-ray single crystallography, and cyclic voltammetry (CV). These studies systematically elucidated the structural, electronic, and redox properties of these new compounds. The molecular structures and conformational properties of the $(DTF)_2$ -Fc compounds were examined by single crystal X-ray diffraction analysis, DFT calculations, and MD simulations. The results pointed to a great potential in redox-controlled molecular switching devices. Another important finding of this project is that supramolecular host-

guest complexation with cyclodextrins can be utilized to regulate the *cis-to-trans* conformational switching of the (DTF)₂-Fc system. The controllability can be further enhanced by combining the redox effects with supramolecular interactions. According to the results from the two research projects, future work is suggested to focus on the following directions. (1) Design and synthesis of (DTF)₂-Fc derivatives with where π -extended molecular frameworks. For instance, fusion of the DTF unit with benzo or a larger arene group. In this way, conformation of the (DTF)₂-Fc system can be better controlled through enhanced intramolecular and intermolecular π -stacking. It is also expected that the redox activity of such derivatives would be different from the current compounds. The extended π -structures, in theory, should facilitate the formation of more stable cationic states and possibly result in intriguing radical species for advanced electronic and magnetic application. (2) Host-guest inclusion of (DTF)₂-Fc with other supramolecular hosts such as cucurbiturils and crown ethers. Studies in this direction will provide more effective supramolecular means to control and stabilize certain conformers of (DTF)₂-Fc. (3) The conformational properties at a temperature lower than room temperature are worth investigating through VT-NMR analysis in the future. The effect of low temperature may lead us to finding other types of conformers and hence some intriguing application in molecular rotary devices. (4) Using the (DTF)₂-Fc compounds as reducing and capping agents in nanoparticle systemesis.³ For example, in a previous study by the Zhao group, DTF derivatives were found to induce the formation of gold nanoparticles (AuNPs), owing to their low oxidation potentials and the ability to complex with Au. In this respect, the (DTF)₂-Fc system is predicted to show effectiveness at AuNP synthesis, yielding hybrid AuNPs useful for photocatalysis, electrocatalysis,

and chemical sensing applications.

Bibliography

- [1] Driscoll, O. J.; Stewart, J. A.; McKeown, P.; Jones, M. D. Ring-Opening Copolymerization Using Simple Fe(III) Complexes and Metal- and Halide-Free Organic Catalysts. *Macromolecules* **2021**, *54*, 8443–8452.
- [2] Driscoll, O. J.; Leung, C. K. C.; Mahon, M. F.; McKeown, P.; Jones, M. D. Iron(III) Salalen Complexes for the Polymerisation of Lactide: Iron(III) Salalen Complexes for the Polymerisation of Lactide. *Eur. J. Inorg. Chem.* **2018**, *47*, 5129–5135.
- [3] Adowsa, H.; Zhao, Y. Redox interactions of Au(III) with carboxylated dithiafulvenes and tetrathiafulvalene analogues in polar organic media. *Chem. Commun.* **2016**, *52*, 13101–13104.

Chapter 5

Appendixes

5.1 Appendix A: Supporting Information for Chapter 2

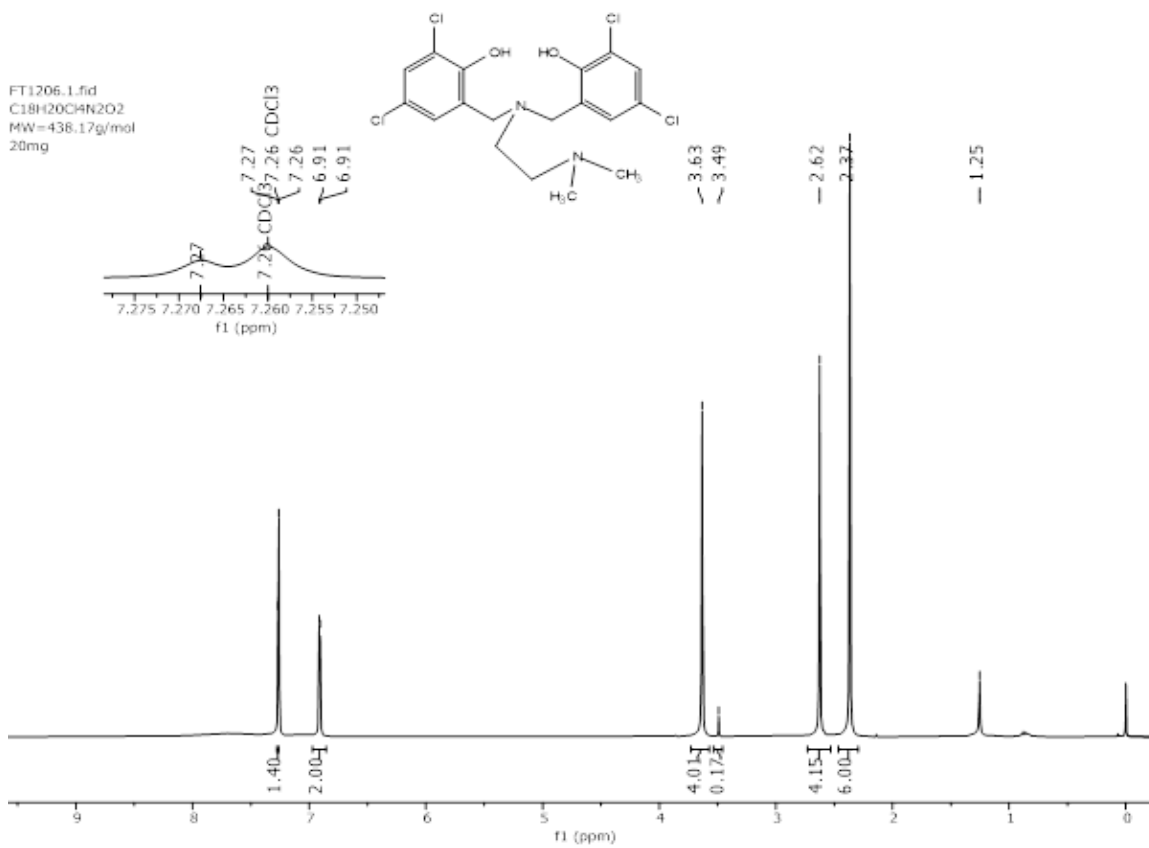


Figure 5.1: ^1H NMR (300 MHz) spectrum of H_2L_1a in CDCl_3 .

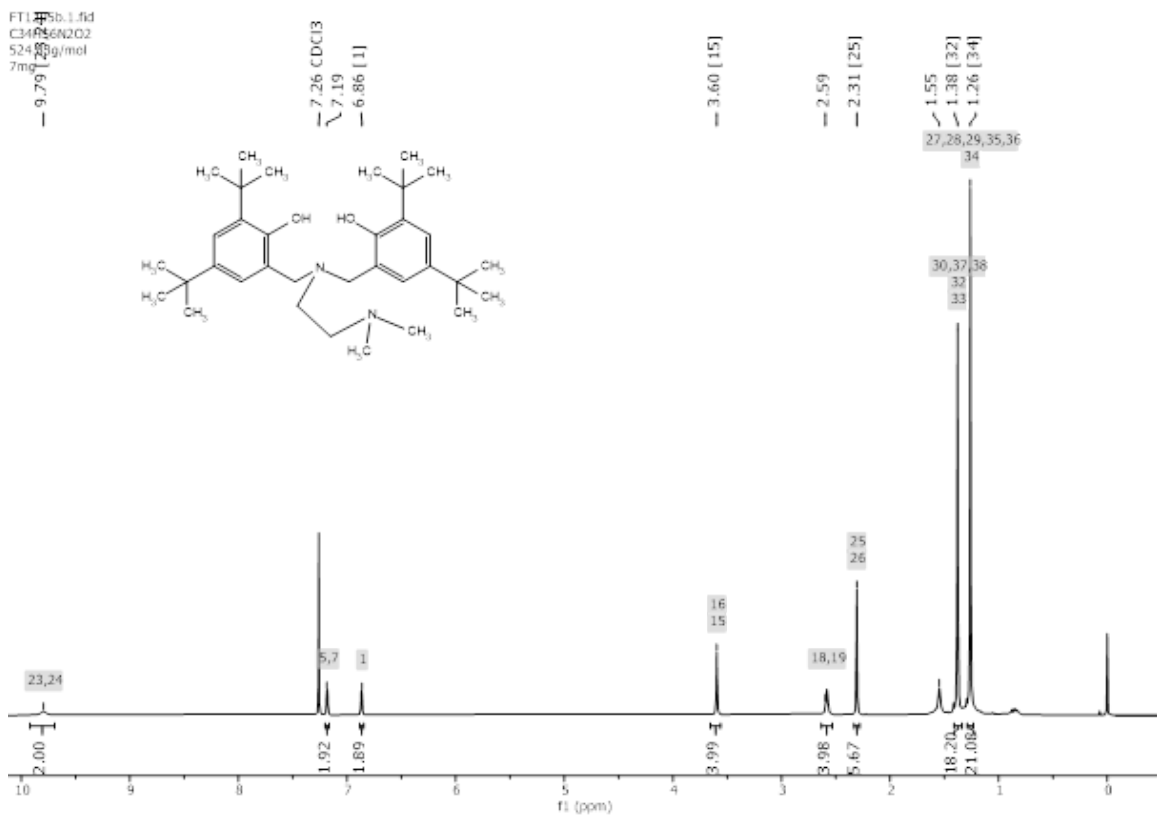


Figure 5.2: ^1H NMR (300 MHz) spectrum of $\text{H}_2\text{L}_1\text{b}$ in CDCl_3 .

FT1204-1.fid

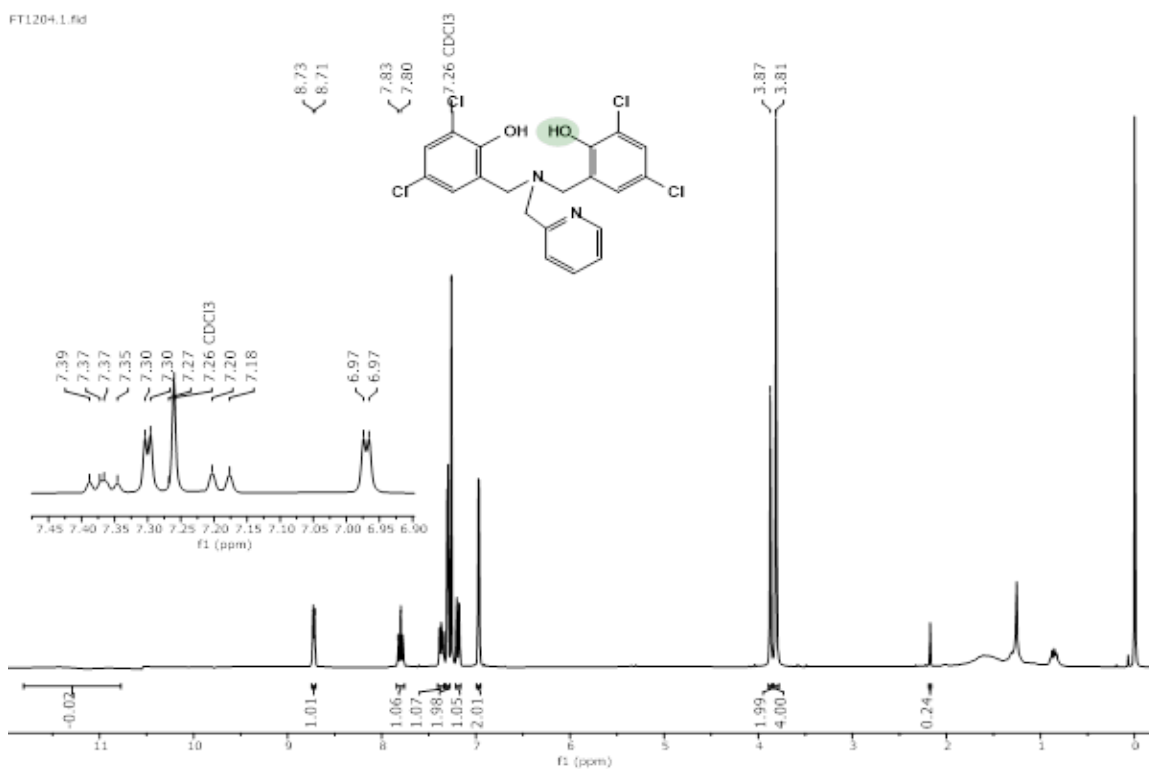


Figure 5.3: ¹H NMR (300 MHz) spectrum of H₂L₁c in CDCl₃.

FT1204-1.fid

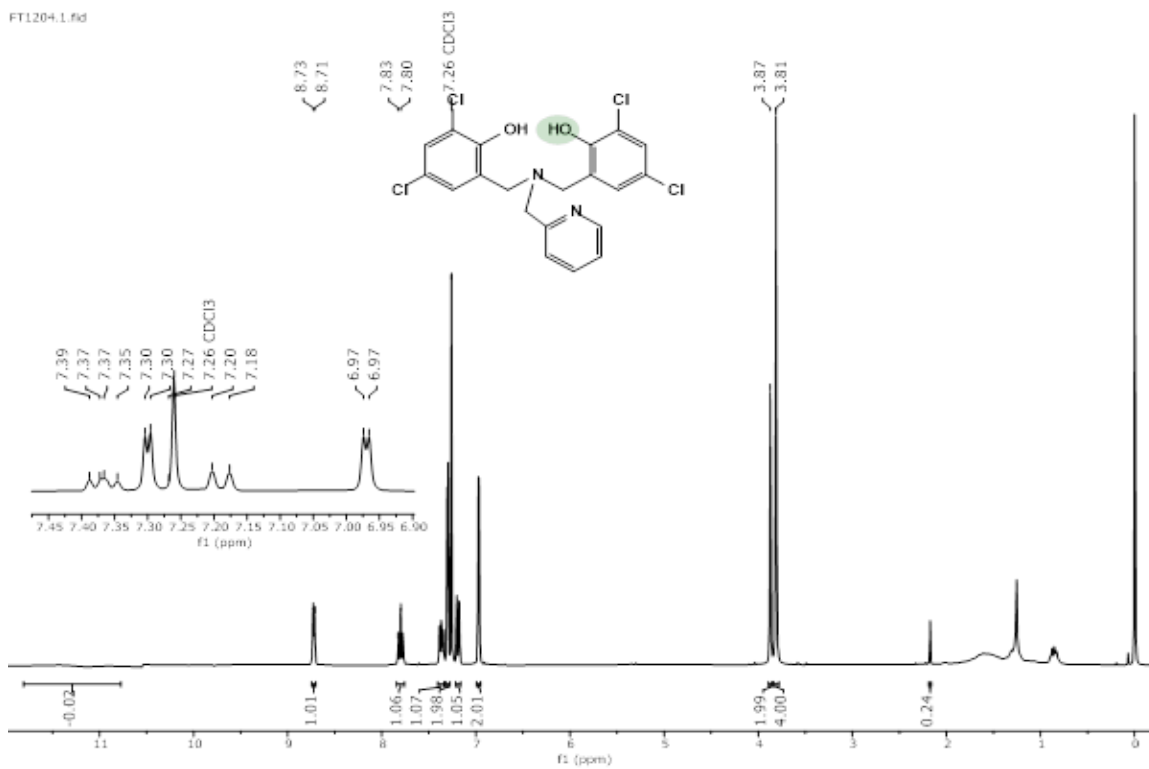


Figure 5.4: ¹H NMR (300 MHz) spectrum of H₂L₁d in CDCl₃.

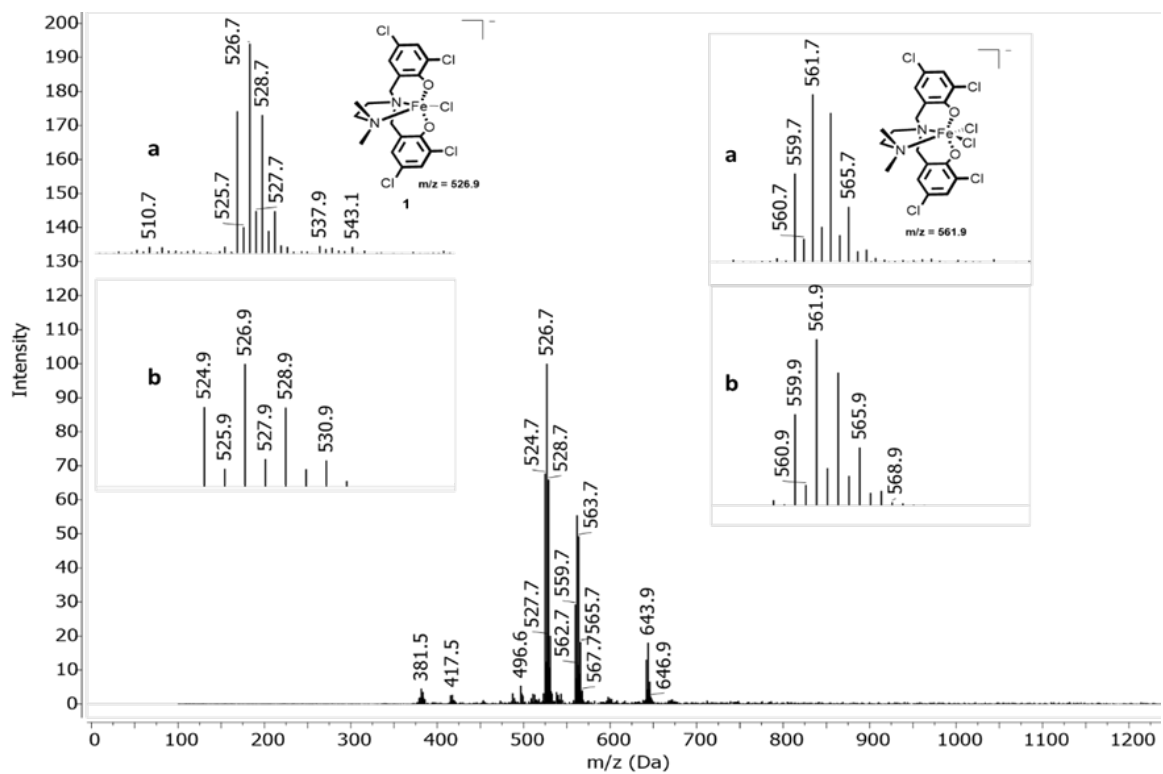


Figure 5.5: MALDI-TOF mass spectrum (negative mode) of complex **1a** showing experimental (a) and theoretical isotopic distribution patterns.

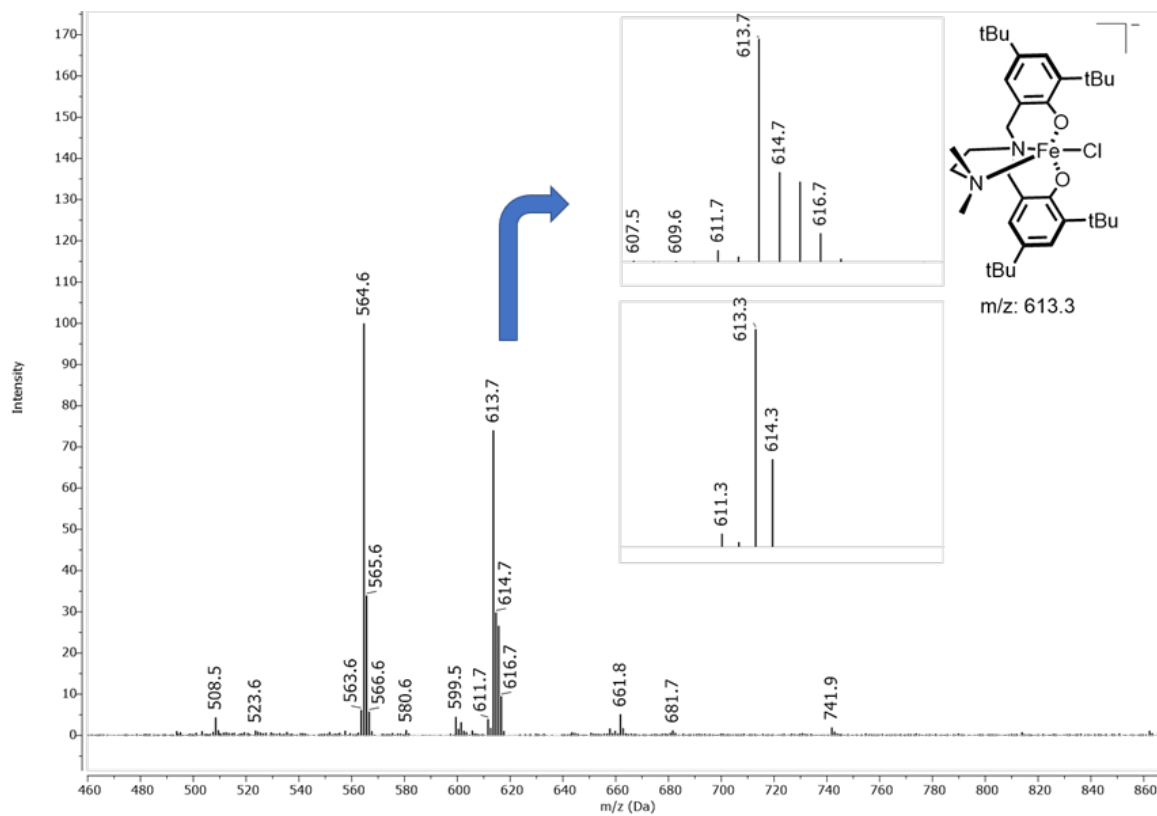


Figure 5.6: MALDI-TOF mass spectrum (negative mode) of complex **1b**.

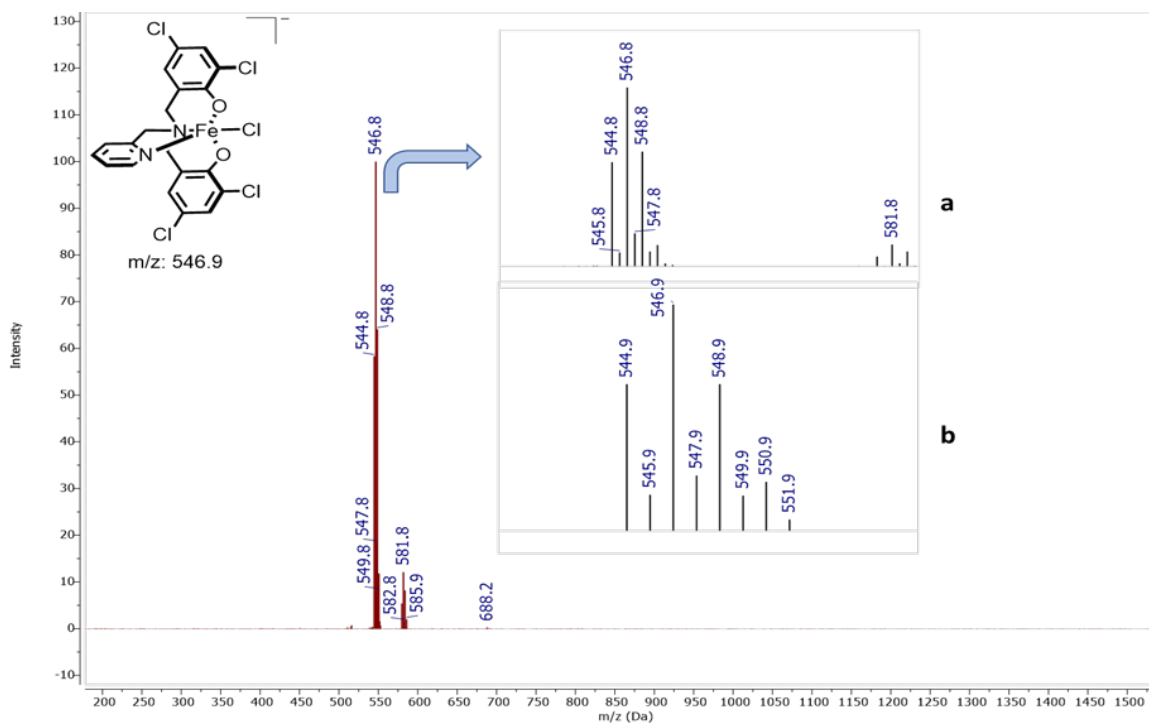


Figure 5.7: MALDI-TOF mas spectrum (negative mode) of complex **1c** showing experimental (a) and theoretical isotopic(b) distribution patterns.

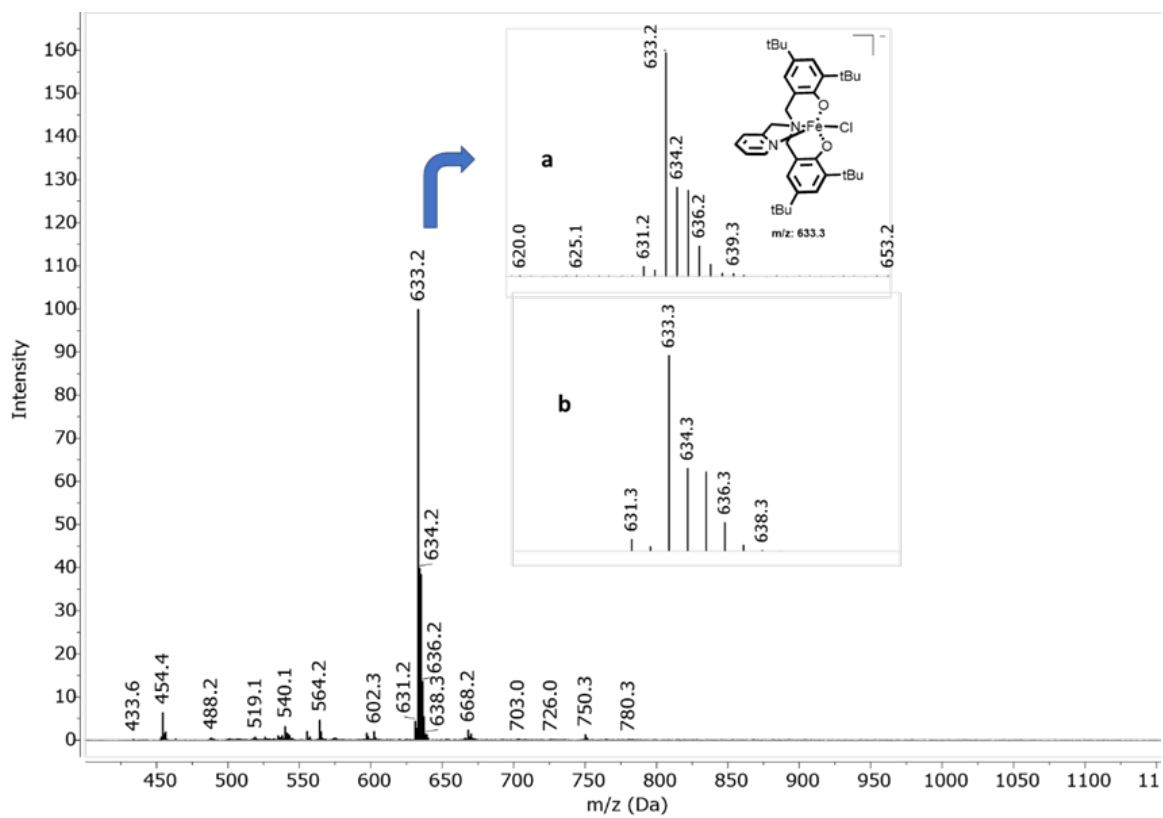


Figure 5.8: MALDI- TOF spectrum in negative mode of complex **1d**

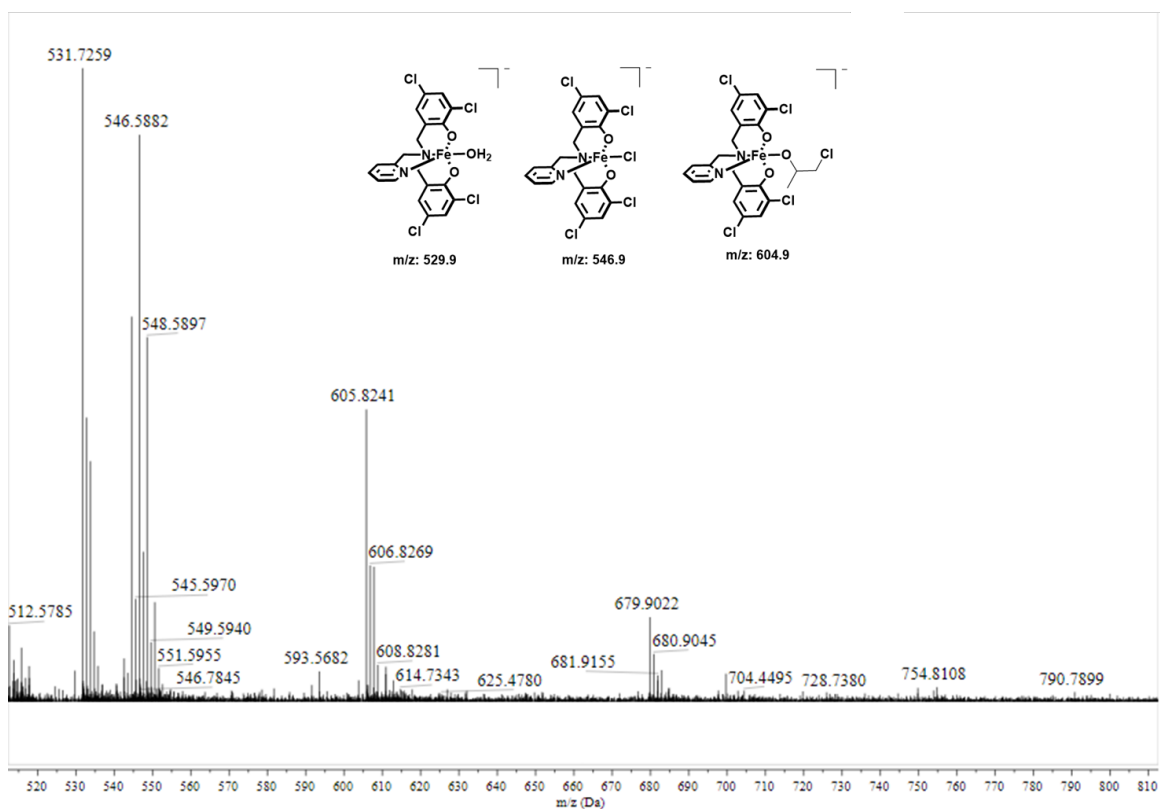


Figure 5.9: MALDI-TOF mass spectrum (negative mode) of complex **1c** with PPnCl in PO showing the formation of alkoxy species at $m/z = 606.1$.

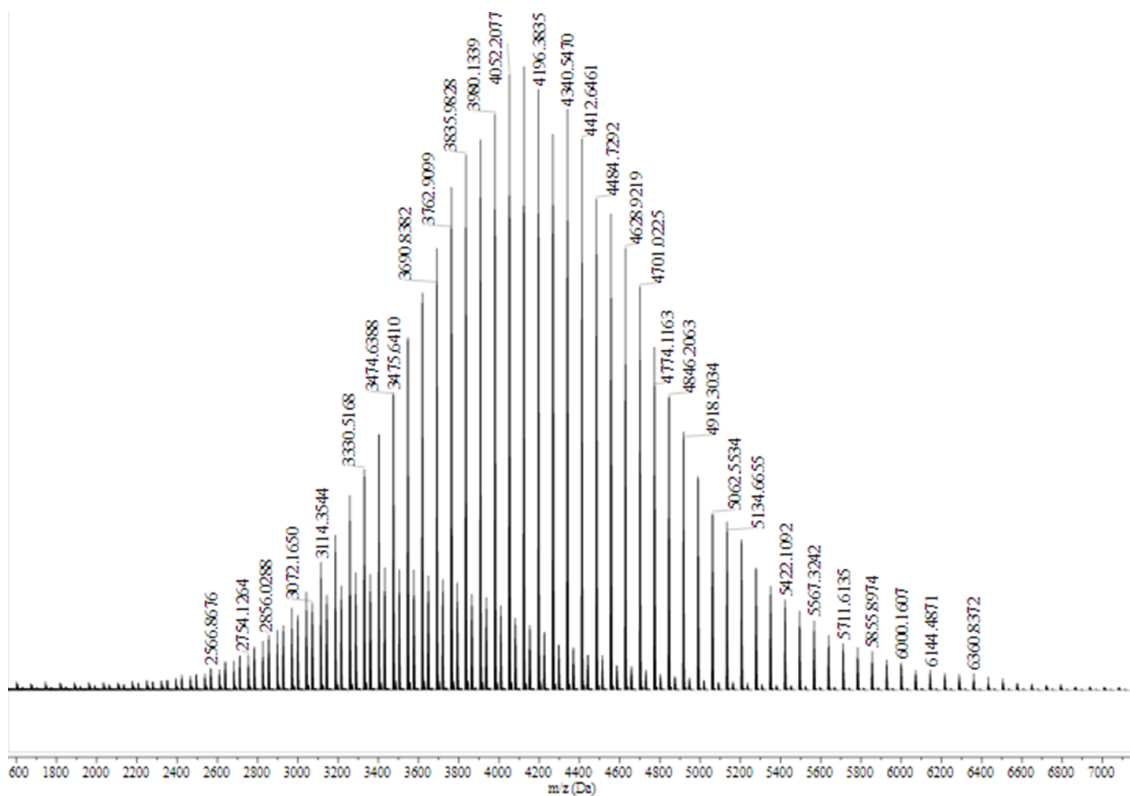


Figure 5.12: MALDI-TOF mass spectrum of PLA derived (with no co-catalyst used).

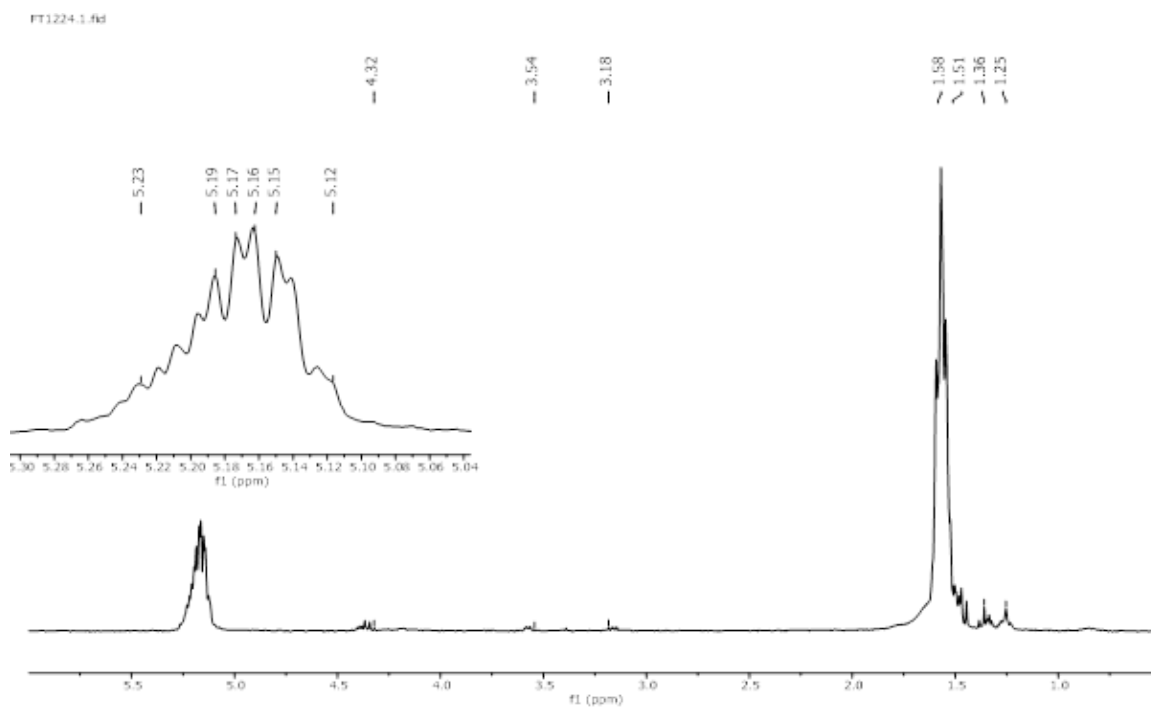


Figure 5.13: ^1H NMR (300 MHz) spectrum of crude polymer(PLA, CDCl_3).

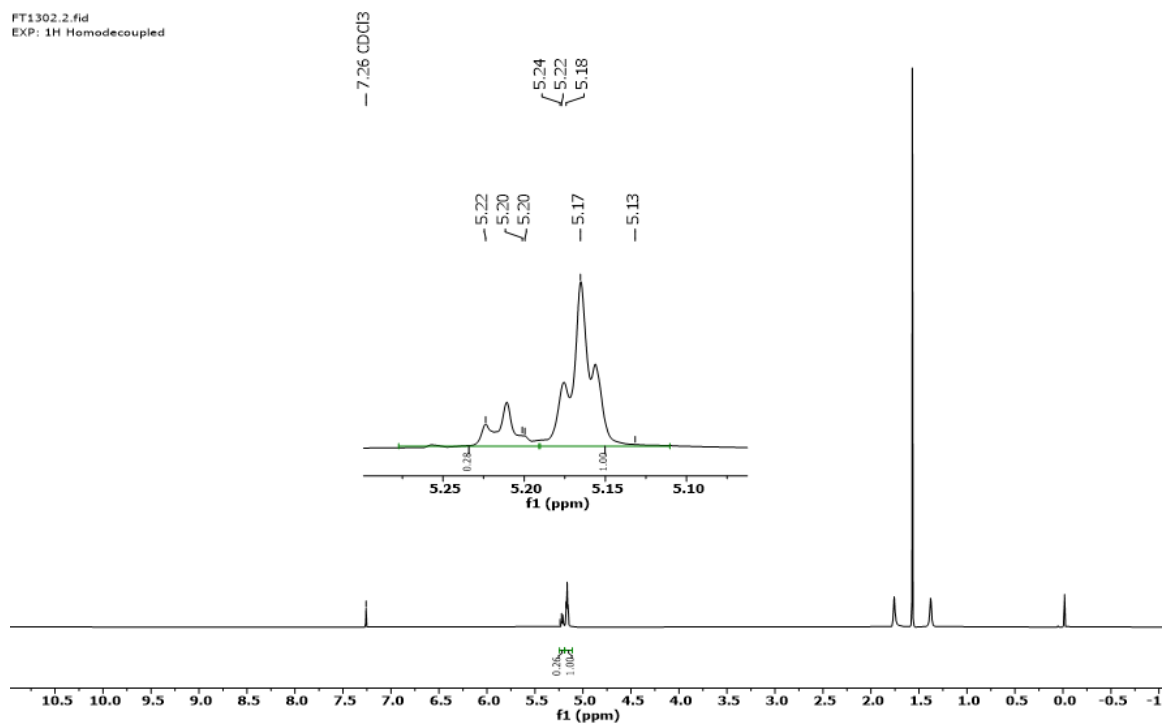


Figure 5.14: ^1H NMR (300 MHz) spectrum of PLA from complex1c (80 °C, 4 hours, $\text{Et}_3\text{NH}^+\text{Cl}^-$, PO, $P_r = 0.48$).

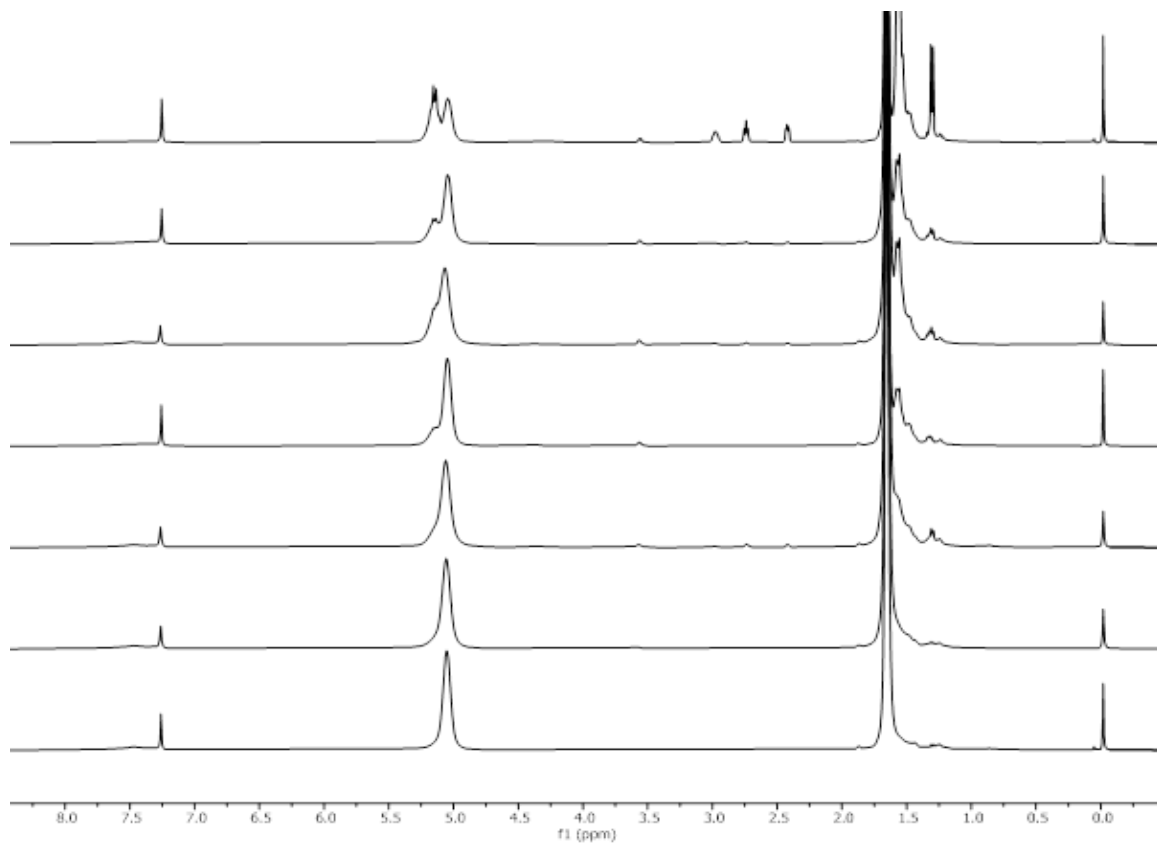


Figure 5.15: ¹H NMR (300 MHz) spectrum of complex **1c** for LA polymerization (at 22 °C, t = 0–25h).

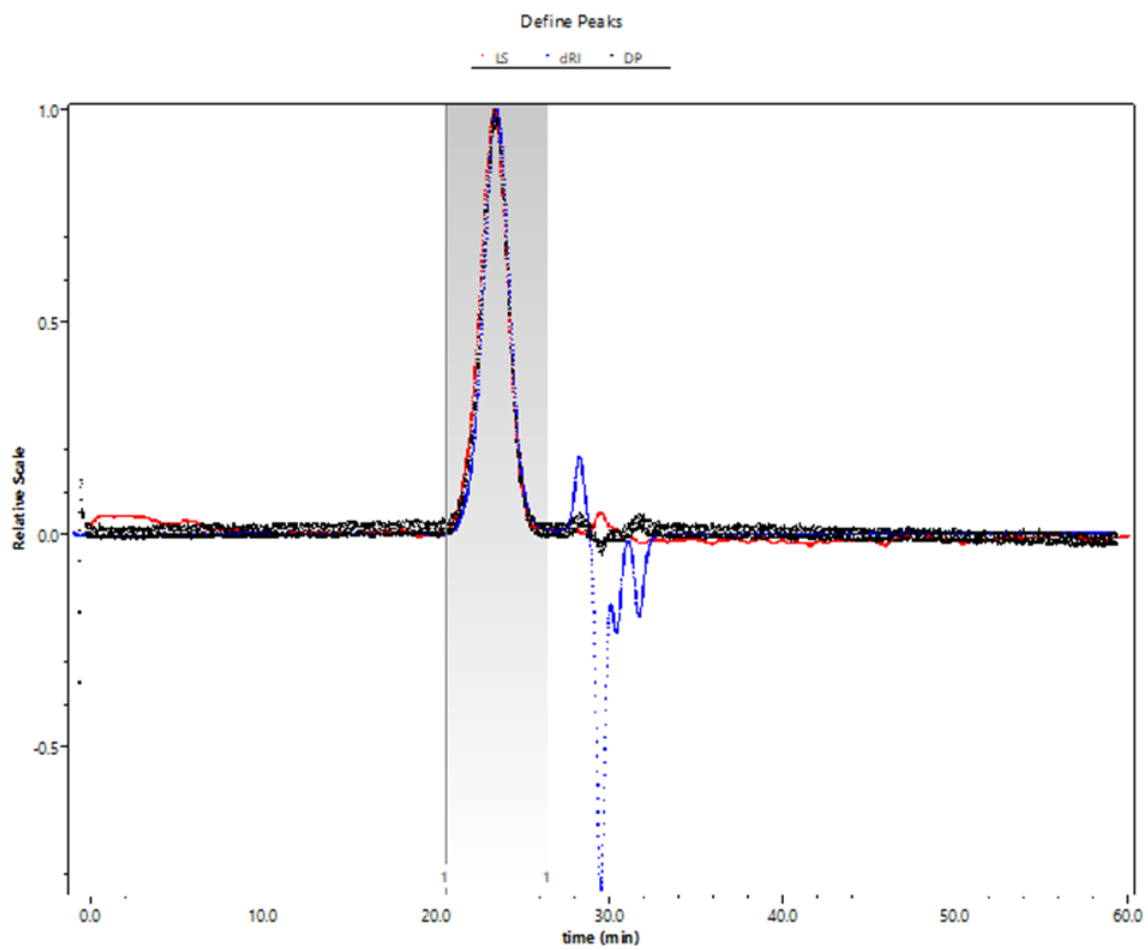


Figure 5.16: Representative GPC for ROP of LA with complex **1c** ($M_w = 6.30$ KDa, $D = 1.06$).

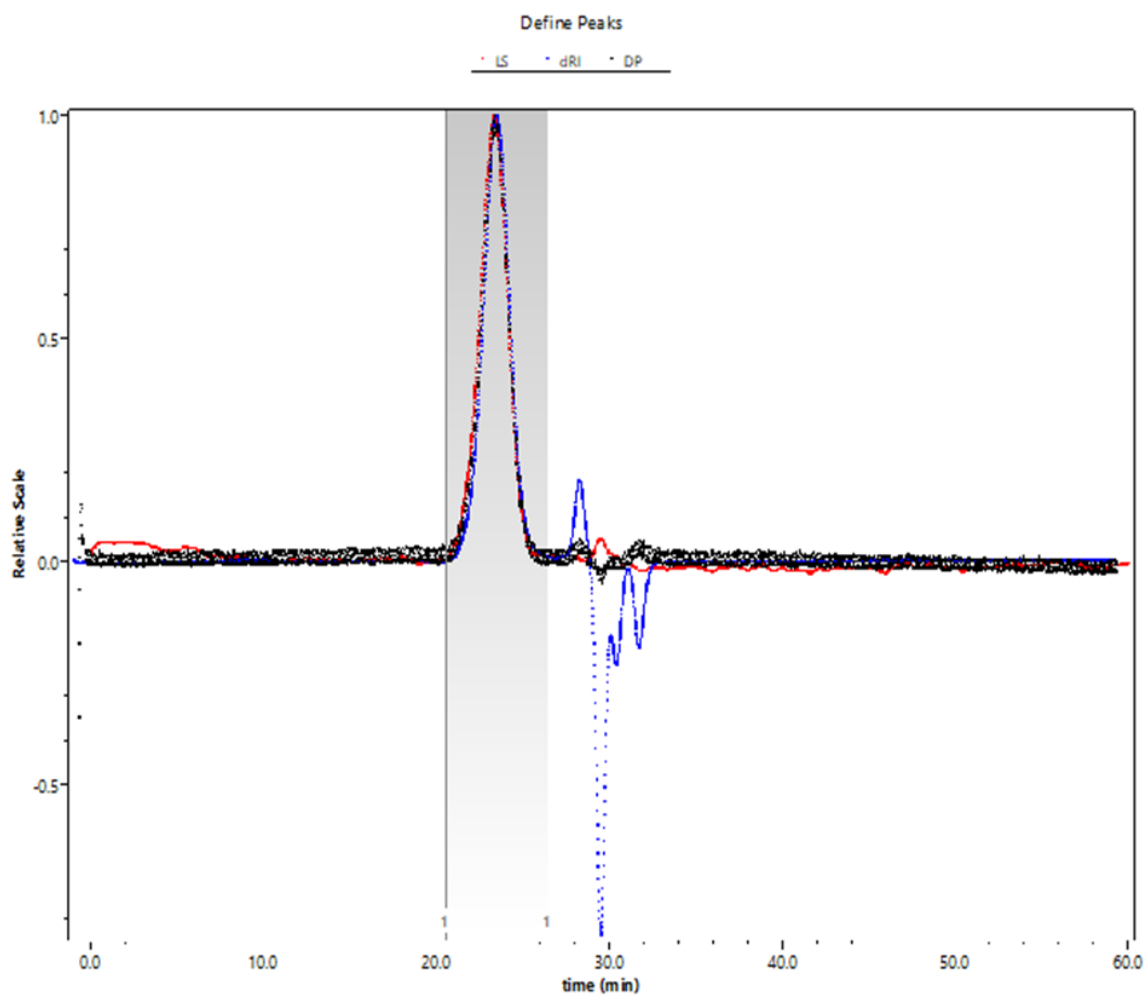


Figure 5.17: Representative GPC for ROP of LA with **1c** ($M_w = 5.70$ KDa, $D = 1.08$).

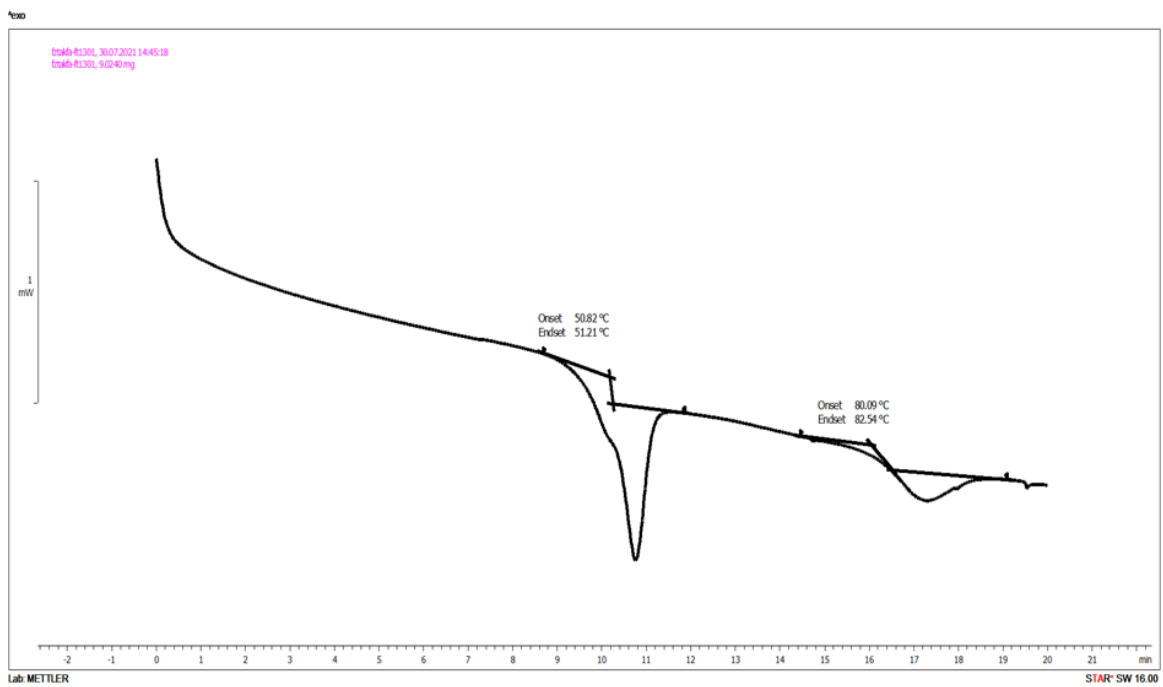


Figure 5.18: Differential scanning calorimetric thermogram of PLA (entry 7).

5.2 Appendix B: Supporting Information for Chapter 3

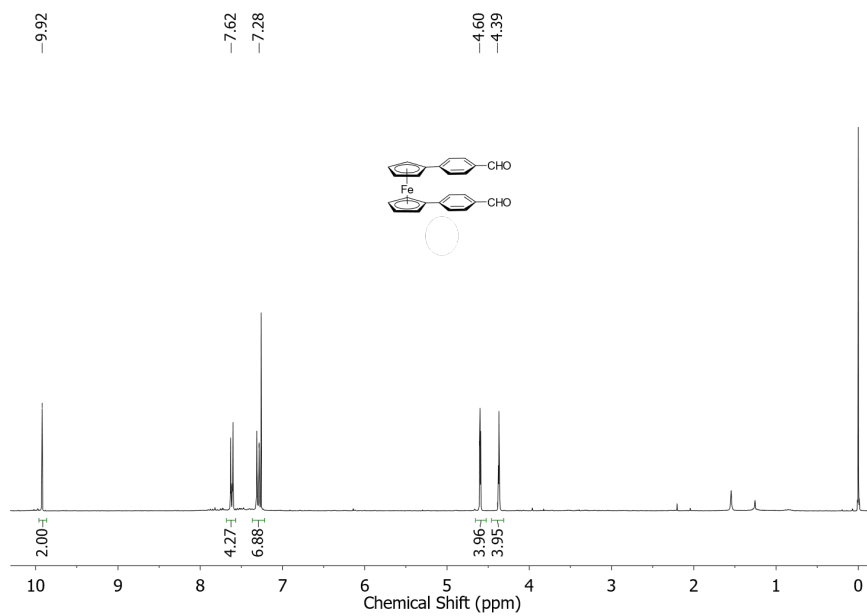


Figure 5.19: ^1H NMR (300 MHz) spectrum of **3a** in CDCl_3 .

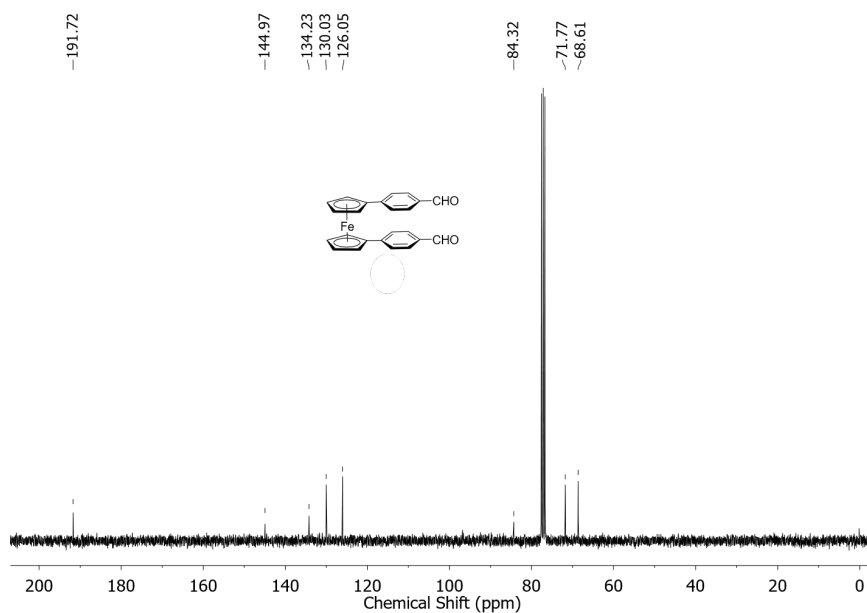


Figure 5.20: ^{13}C NMR (75 MHz) spectrum of **3a** in CDCl_3 .

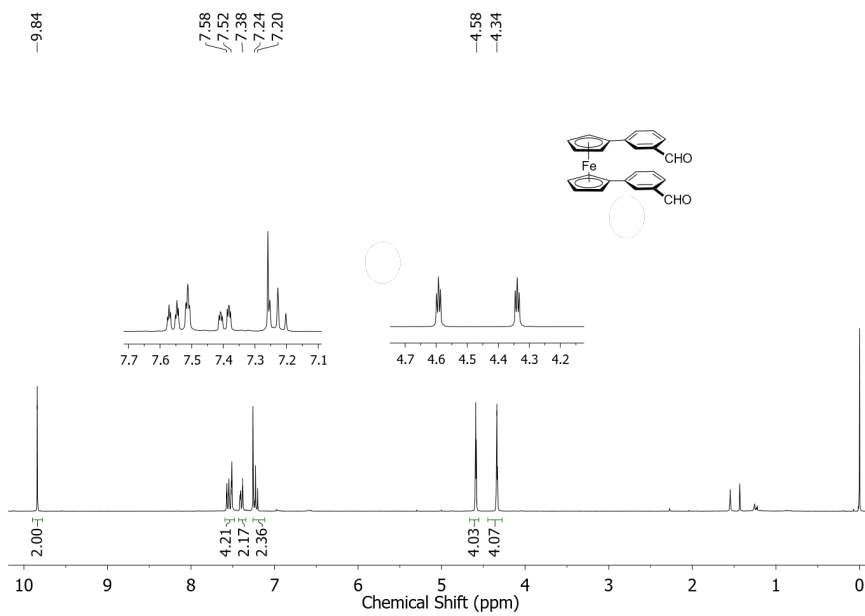


Figure 5.21: ^1H NMR (300 MHz) spectrum of **3b** in CDCl_3 .

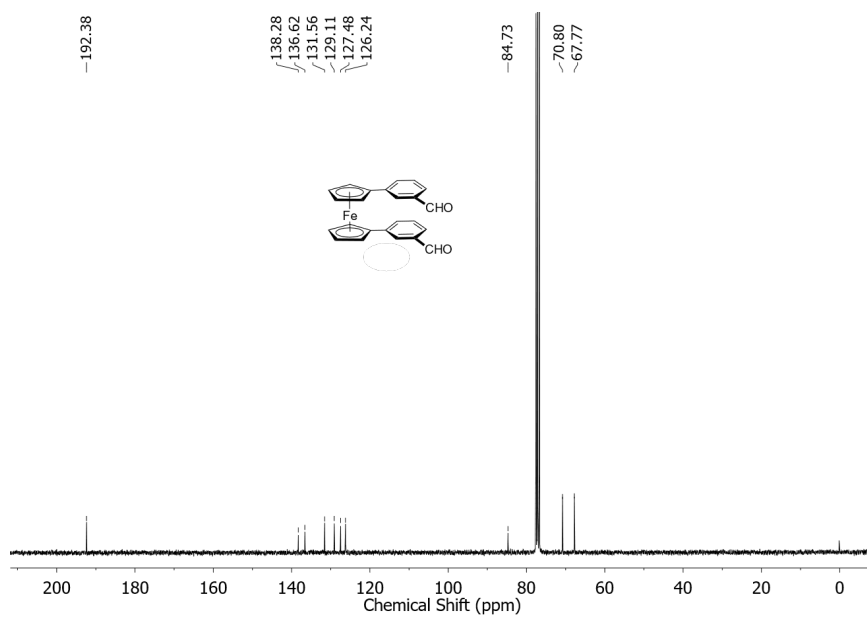


Figure 5.22: ^{13}C NMR (75 MHz) spectrum of **3b** in CDCl_3 .

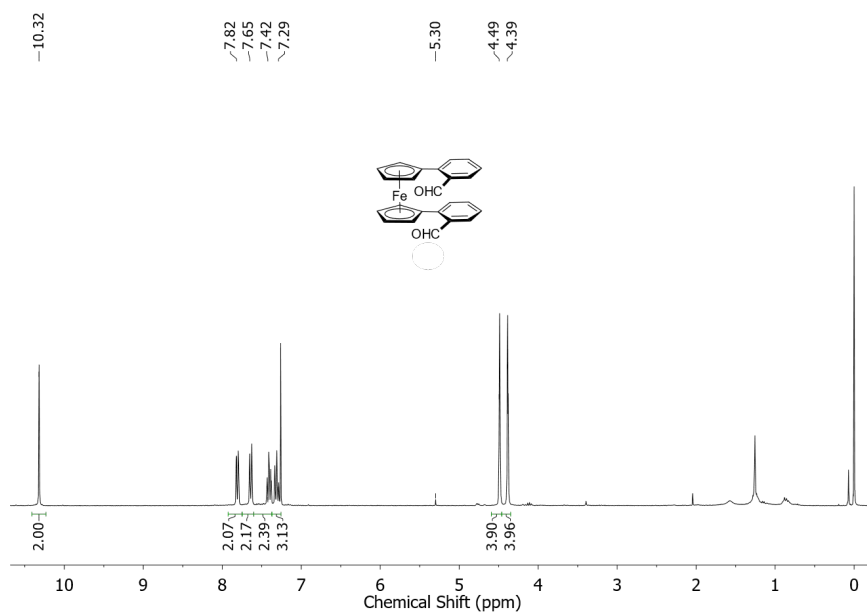


Figure 5.23: ^1H NMR (300 MHz) spectrum of **3c** in CDCl_3 .

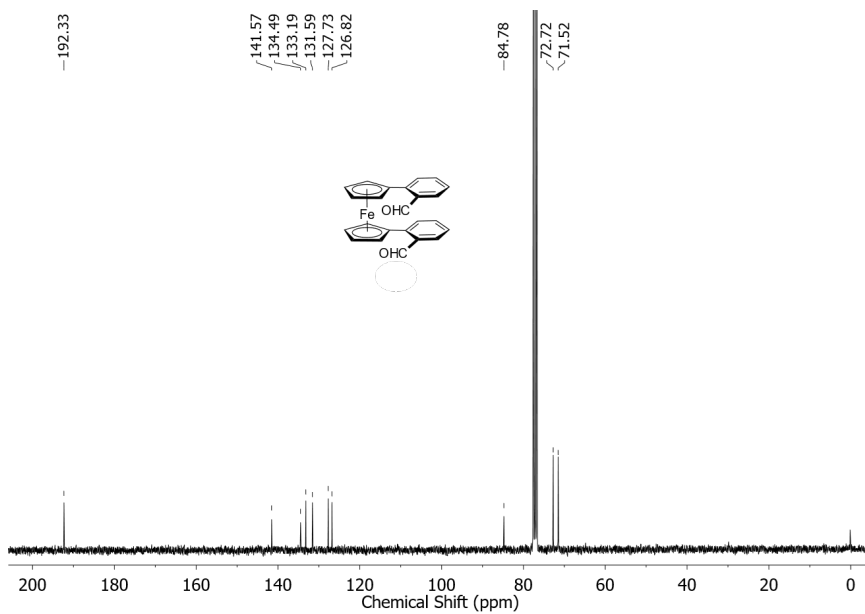


Figure 5.24: ^{13}C NMR (75 MHz) spectrum of **3c** in CDCl_3 .

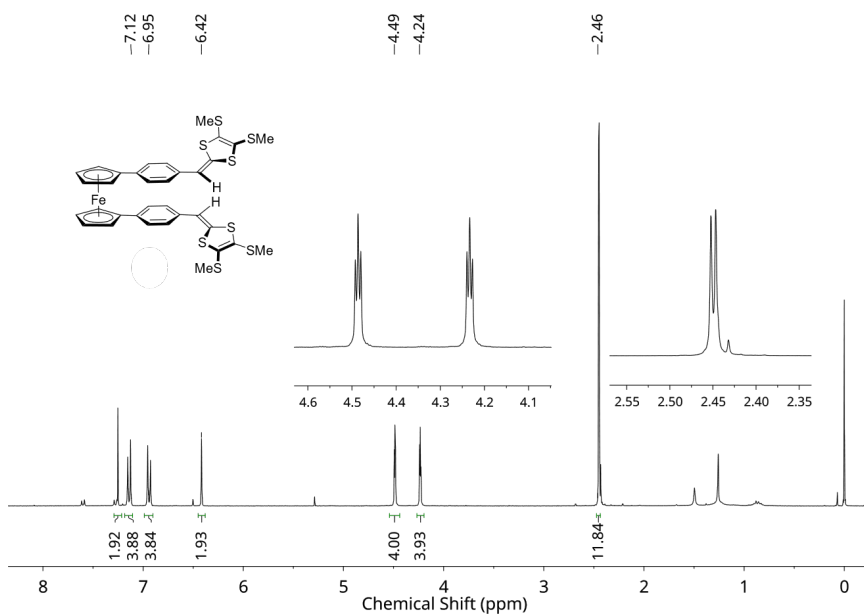


Figure 5.25: ^1H NMR (300 MHz) spectrum of **5a** in CDCl_3 .

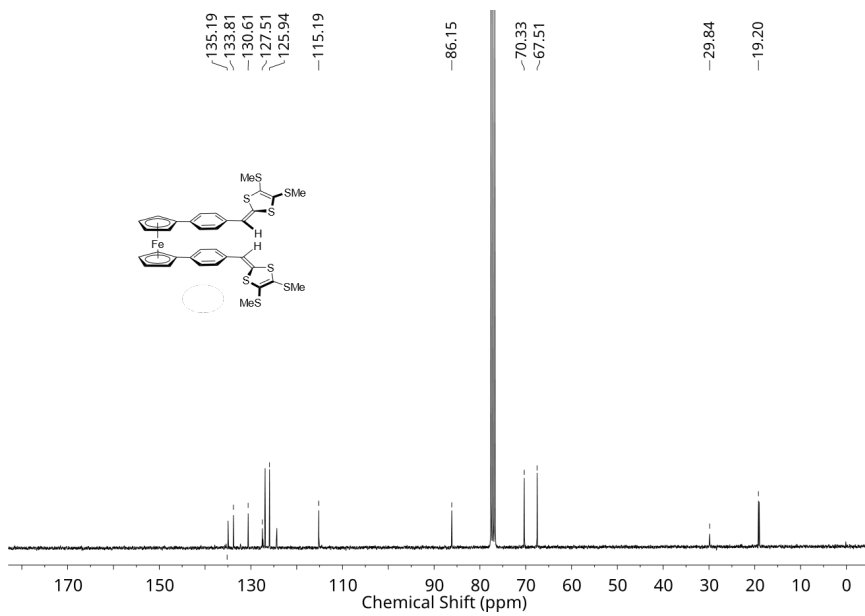


Figure 5.26: ^{13}C NMR (75 MHz) spectrum of **5a** in CDCl_3 .

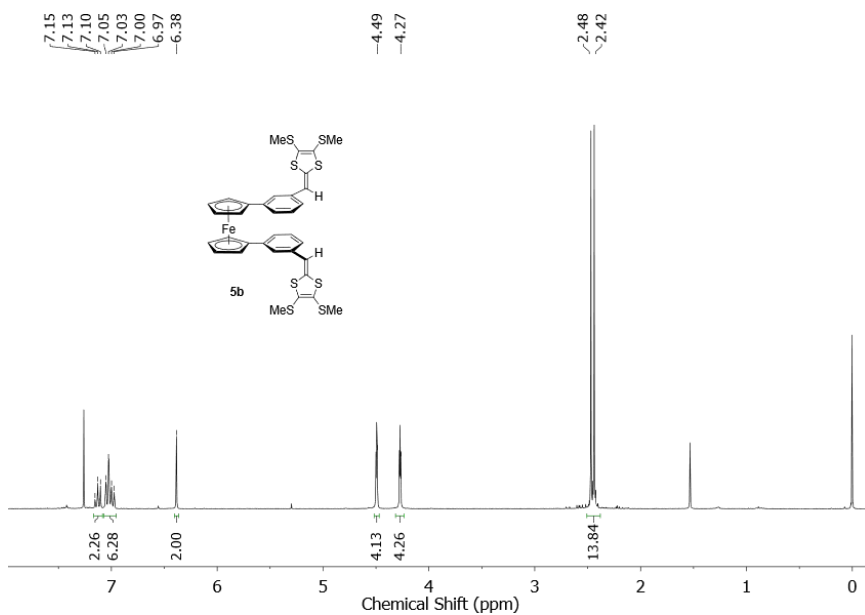


Figure 5.27: ^1H NMR (300 MHz) spectrum of **5b** in CDCl_3 .

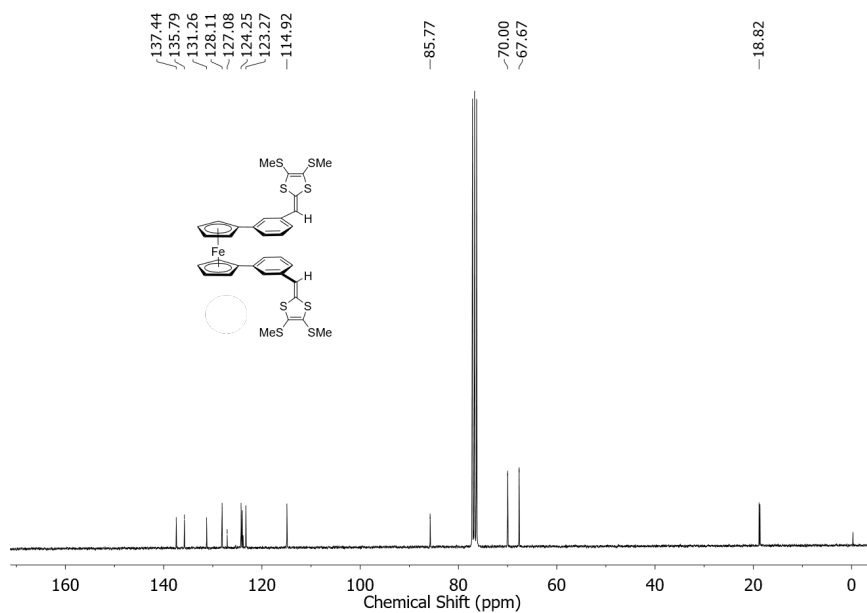


Figure 5.28: ^{13}C NMR (75 MHz) spectrum of **5b** in CDCl_3 .

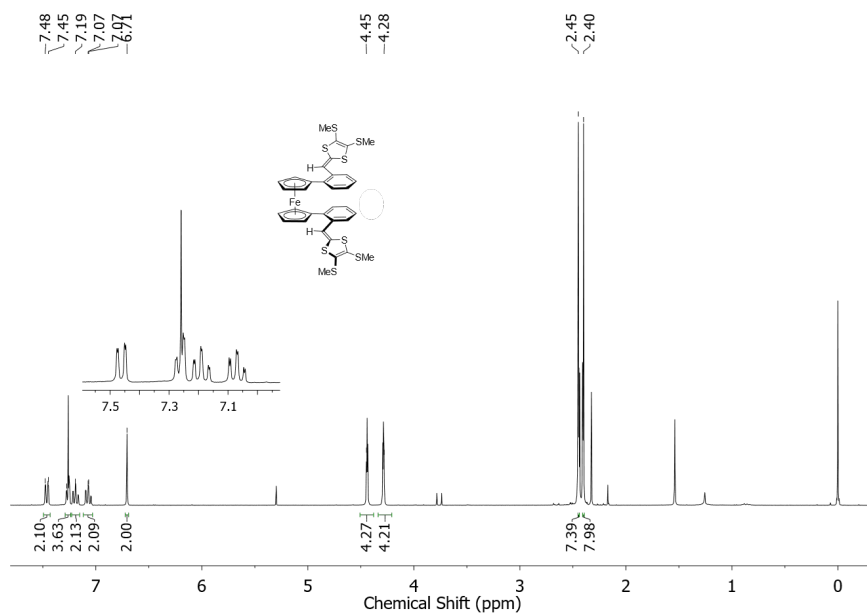


Figure 5.29: ^1H NMR (300 MHz) spectrum of **5c** in CDCl_3 .

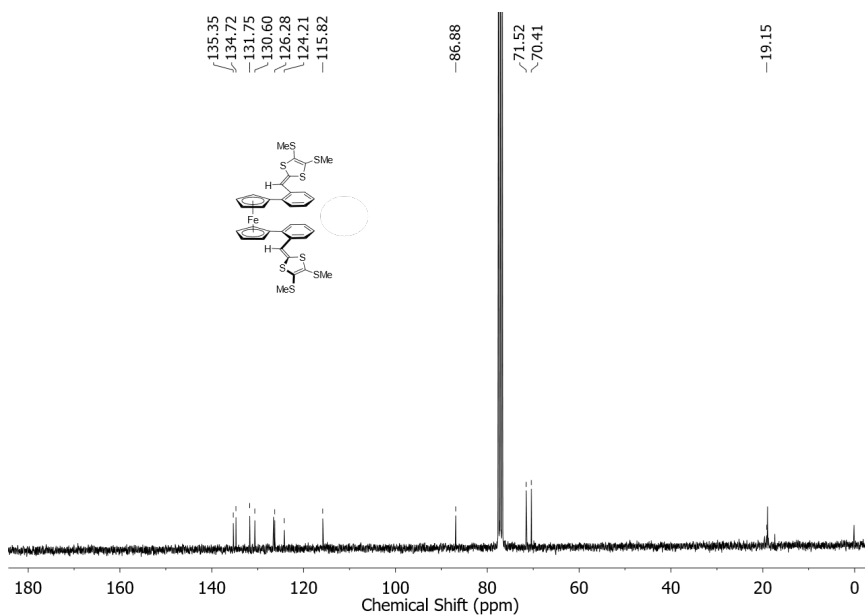


Figure 5.30: ^{13}C NMR (75 MHz) spectrum of **5c** in CDCl_3 .

Table 5.1: Summary of Experimental UV-Vis absorption data of **3a–c** and **5a–c** (measured in CH_2Cl_2)

Entry	λ_{max}/nm ($\epsilon/\text{mol}^{-1}\text{L cm}^{-1}$)
3a	291 (4.31×10^4)
3b	296 (1.40×10^4)
3c	300 (2.20×10^4)
5a	370 (4.37×10^4)
5b	345 (2.20×10^4)
5c	346 (1.10×10^4)

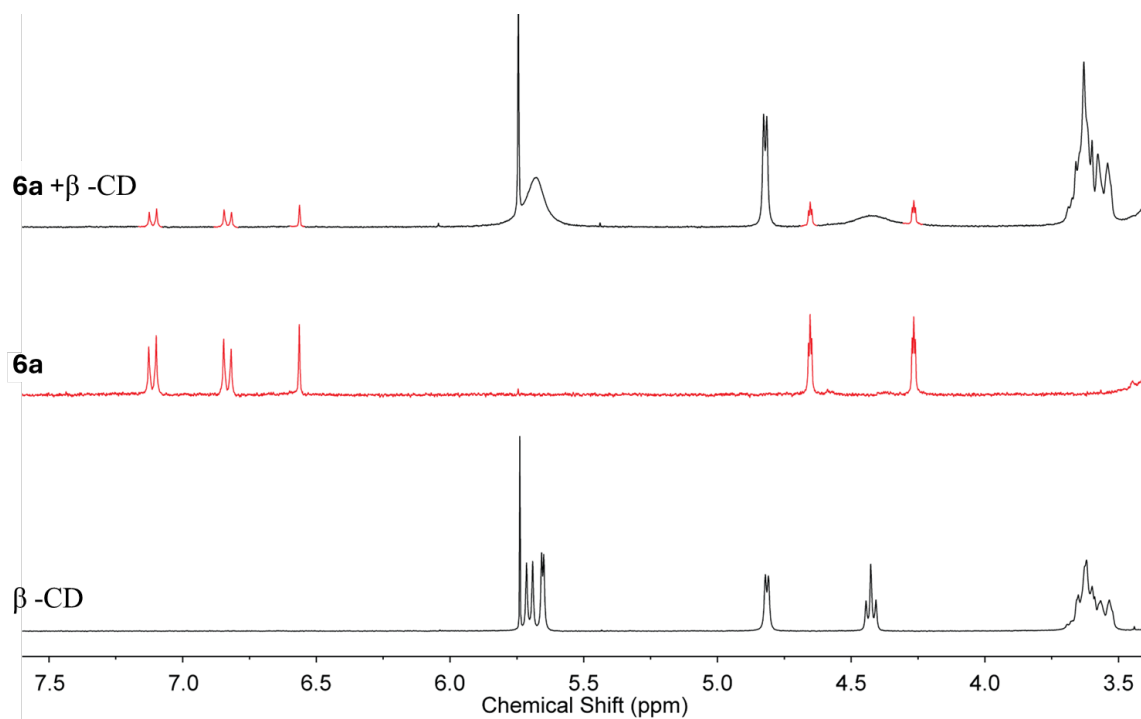


Figure 5.31: ^1H NMR (300 MHz, DMSO- d_6) spectrum of a mixture of **6a** and β -CD (ca. 1:2 mole ratio) in comparison with those of pure **5a** and β -CD.

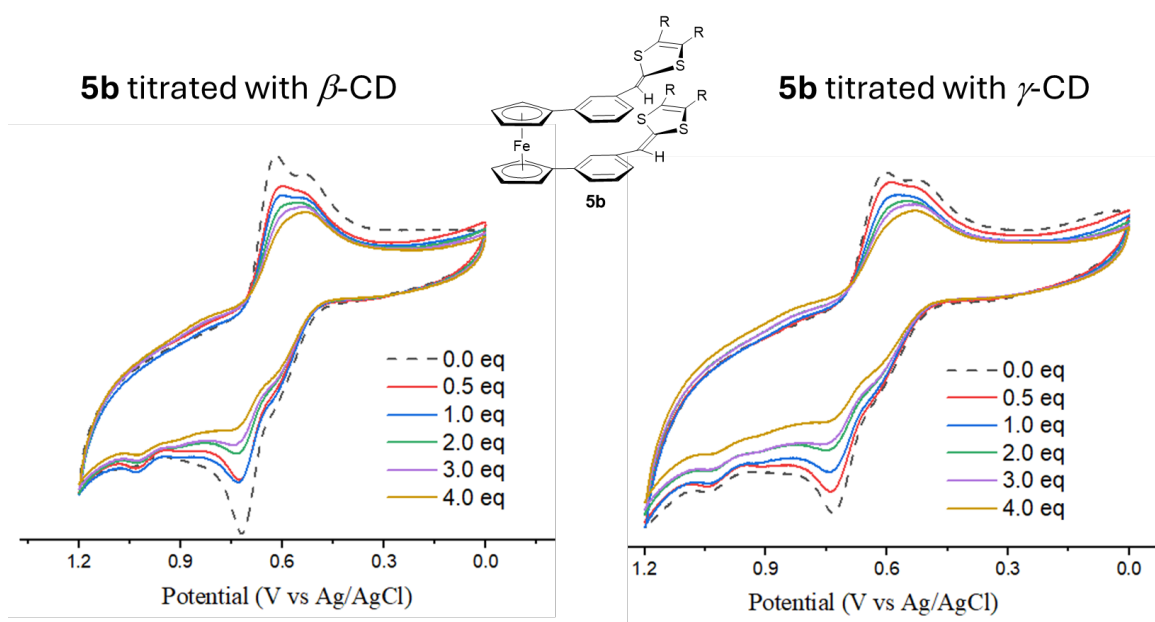


Figure 5.32: CV of **5b** with CD measured in DMF. Experimental conditions: electrolyte: $n\text{-Bu}_4\text{NBF}_4$, 0.1 M, working electrode: glassy carbon, reference electrode: Ag/AgCl, counter electrode: Pt wire. Scan rate = 200 mV/s.

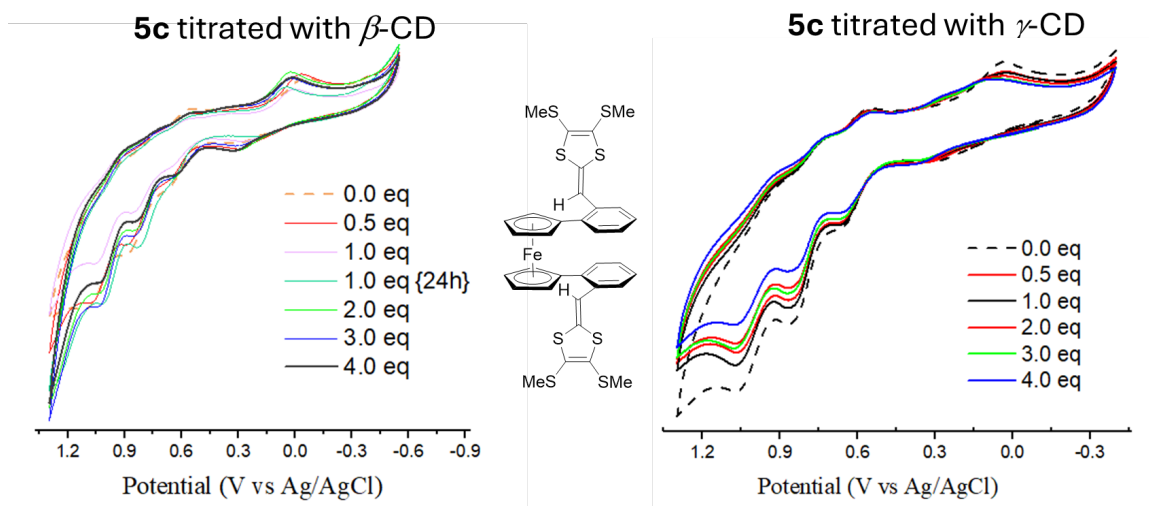


Figure 5.33: CV of **5c** with CD measured in DMF. Experimental conditions: electrolyte: $n\text{-Bu}_4\text{BF}_4$, 0.1 M, working electrode: glassy carbon, reference electrode: Ag/AgCl, counter electrode: Pt wire. Scan rate = 200 mV/s.

Table 5.2: Summary of TD-DTF results for *para*-**5a**(transitions with $f < 0.001$ are omitted)

λ_{abs} (nm)	f	Major MO Contributions
552.5	0.005	H-3→L (11%), H-3→L+10 (33%), H-2→L+9 (25%)
357.6	0.0019	H-7→L (10%), H-7→L+10 (30%), H-3→L+9 (18%)
355.1	0.0019	H-7→L+9 (37%), H-3→L+10 (12%), H-2→L+9 (17%)
351.9	0.0268	H-1→L+1 (35%), H→L (47%)
342.1	0.3049	H-1→L+3 (10%), H-1→L+5 (18%), H→L+1 (15%), H→L+4 (39%)
328.5	1.5612	H-1→L (22%), H→L+1 (50%)

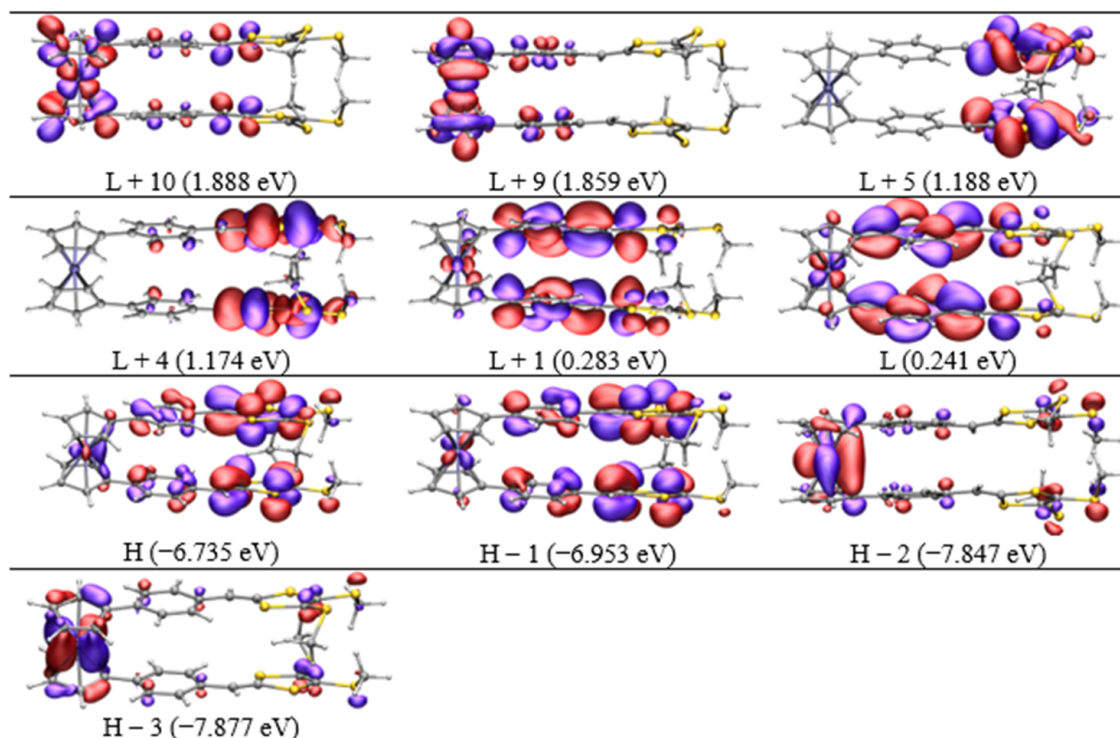


Figure 5.34: Plots of MOs involved in vertical electronic transitions of *para-5a* (isovalue = 0.03 a.u.).

Table 5.3: Summary of TD-DTF results for *meta-5b* transitions with $f < 0.003$ are omitted

λ_{abs} (nm)	f	Major MO Contributions
546.9	0.0003	H-3 \rightarrow L+8 (32%), H-2 \rightarrow L+4 (15%), H-2 \rightarrow L+10 (15%)
545.7	0.0003	H-3 \rightarrow L+4 (14%), H-3 \rightarrow L+10 (14%), H-2 \rightarrow L+8 (36%)
340.0	0.0444	H \rightarrow L (25%), H \rightarrow L+5 (19%), H \rightarrow L+7 (22%)
336.5	0.0142	H \rightarrow L (43%), H \rightarrow L+5 (15%), H \rightarrow L+7 (13%)
331.1	0.0346	H-1 \rightarrow L+1 (27%), H-1 \rightarrow L+6 (34%)
321.5	0.4527	H-1 \rightarrow L (49%), H-1 \rightarrow L+2 (11%)

Table 5.4: Summary of TD-DTF results for *ortho-5c* (transitions with $f < 0.0005$ are omitted)

$\lambda_{abs}(\text{nm})$	f	Major MO Contributions
553.8	0.0005	H-3→L+8 (31%), H-2→L+9 (23%)
482.2	0.0004	H-10→L+9 (19%), H-3→L+8 (28%)
353.0	0.0006	H-10→L+8 (35%), H-2→L+8 (19%)
335.4	0.0325	H-1→L (17%), H→L (29%), H→L+6 (17%)
329.9	0.2241	H-1→L+1 (21%), H-1→L+6 (14%), H→L+1 (23%), H→L+7 (13%)
323.6	0.327	H-1→L+3 (19%), H→L (10%), H→L+2 (23%), H→L+3 (19%)
317.1	0.1284	H-1→L+2 (46%), H→L+2 (24%), H→L+3 (12%)

Table 5.5: Crystal data and structure refinement for **5a**

Empirical formula	$C_{34}H_{30}FeS_8$
Formula weight	750.91
Temperature/K	100(2)
Crystal system	monoclinic
Space group	$I2/a$
$a/\text{\AA}$	12.9808(5)
$b/\text{\AA}$	7.4691(2)
$c/\text{\AA}$	33.2905(14)
$\alpha/^\circ$	90
$\beta/^\circ$	95.311(4)
$\gamma/^\circ$	90
Volume/ \AA^3	3213.8(2)
Z	4
ρ_{calc}/cm^3	1.552
μ/mm^{-1}	8.816
$F(000)$	1552.0
<i>Crystal size</i> / mm^3	$0.135 \times 0.105 \times 0.032$
Radiation	Cu $K\alpha$ ($\lambda = 1.54184$)
2θ range for data collection/ $^\circ$	5.332 to 158.86
Index ranges	$-16 \leq h \leq 16, -9 \leq k \leq 9, -42 \leq l \leq 42$
Reflections collected	5990
Independent reflections	5990 [$R_{sigma} = 0.0201$]
Data/restraints/parameters	5990/0/199
Goodness-of-fit on F^2	1.121
Final R indexes [$Igeq2\sigma(I)$]	$R_1 = 0.0756, wR_2 = 0.2081$
Final R indexes [all data]	$R_1 = 0.0808, wR_2 = 0.2150$
Largest diff. peak/hole / $e \text{\AA}^{-3}$	1.34/−0.76

Table 5.6: Crystal data and structure refinement for **5c**

Empirical formula	$C_{34}H_{30}FeS_8$
Formula weight	750.91
Temperature/K	100(2)
Crystal system	monoclinic
Space group	$P2_1/n$
$a/\text{\AA}$	12.56600(10)
$b/\text{\AA}$	12.79260(10)
$c/\text{\AA}$	20.7214(2)
$\alpha/^\circ$	90
$\beta/^\circ$	99.6380(10)
$\gamma/^\circ$	90
Volume/ \AA^3	3283.99(5)
Z	4
$\rho_{calc}/\text{g/cm}^3$	1.519
μ/mm^{-1}	8.628
$F(000)$	1552.0
Crystal size/ mm^3	$0.284 \times 0.128 \times 0.057$
Radiation	Cu $K\alpha$ ($\lambda = 1.54184$)
2θ range for data collection/ $^\circ$	7.702 to 158.926
Index ranges	$-15 \leq h \leq 15, -16 \leq k \leq 10, -26 \leq l \leq 25$
Reflections collected	42451
Independent reflections	7026 [$R_{int} = 0.0639, R_{sigma} = 0.0413$]
Data/restraints/parameters	7026/1/511
Goodness-of-fit on F^2	1.060
Final R indexes [$I \geq 2\sigma$ (I)]	$R_1 = 0.0456, wR_2 = 0.1103$
Final R indexes [all data]	$R_1 = 0.0512, wR_2 = 0.1173$
Largest diff. peak/hole / $e \text{\AA}^{-3}$	0.58/-0.45

Results of Computational Modeling Studies

Optimized molecular geometries of 5a in different conformations, oxidation and electron spin states (ω B97XD/Def2-SVP)

<i>Cis-5a</i> (charge = 0, S = 1) <i>E</i> = -5760.415032 Hartree, <i>D</i> = 0.044 Debye				<i>Trans-5a</i> (charge = 0, S = 1) <i>E</i> = -5759.936458 Hartree, <i>D</i> = 0.000 Debye			
Fe	-6.341750	0.000014	-0.000020	Fe	0.000000	0.000000	0.000000
S	1.807750	2.300100	0.084790	S	-5.886860	-0.740190	5.498190
S	3.132800	0.879880	-2.123420	S	-8.014380	-2.585060	4.664200
S	4.434120	3.304180	1.234580	S	-7.538590	0.520600	7.674330
S	5.924240	1.651800	-1.211880	S	-9.901060	-1.571500	6.826410
C	-6.252000	1.472610	-1.422310	C	0.135420	-2.035330	0.079220
H	-6.199320	1.316850	-2.497870	H	-0.320420	-2.649810	-0.483460
C	-7.449450	1.600090	-0.664530	C	1.399400	-1.460960	-0.182310
H	-8.462140	1.549480	-1.059580	H	1.932680	-1.619580	-0.950740
C	-7.088720	1.781680	0.701050	C	1.739370	-0.601260	0.908240
H	-7.776420	1.888160	1.537650	H	2.540880	-0.097430	0.995020
C	-5.668130	1.766610	0.785200	C	0.660740	-0.634130	1.843010
H	-5.088020	1.843350	1.702750	H	0.614590	-0.147280	2.657380
C	-5.135280	1.577390	-0.530890	C	-0.346180	-1.534900	1.336180
C	-3.708730	1.452690	-0.885250	C	-1.639790	-1.835160	1.972280
C	-2.704740	1.832000	0.011810	C	-2.153540	-1.076300	3.016430
H	-2.975350	2.256370	0.979740	H	-1.635260	-0.359930	3.364880
C	-1.358270	1.670740	-0.291230	C	-3.394420	-1.332490	3.560050
H	-0.625300	1.944030	0.467560	H	-3.707380	-0.789670	4.275570
C	-0.950800	1.122720	-1.517150	C	-4.214470	-2.385630	3.081730
C	-1.963620	0.753380	-2.421460	C	-3.665260	-3.187070	2.075040
H	-1.684170	0.318780	-3.384840	H	-4.155840	-3.935260	1.755630
C	-3.306330	0.912890	-2.115280	C	-2.409490	-2.909960	1.524790
H	-4.057940	0.591130	-2.839050	H	-2.073200	-3.466040	0.832300
C	0.437370	0.884320	-1.908220	C	-5.568900	-2.680660	3.520270
H	0.551370	0.296200	-2.824730	H	-5.973870	-3.426180	3.093800
C	1.595730	1.293240	-1.347210	C	-6.340870	-2.065210	4.437800
C	3.578000	2.296770	0.074990	C	-7.415030	-0.654290	6.357710
C	4.185880	1.636260	-0.935480	C	-8.381640	-1.505770	5.989770
C	3.679010	2.810470	2.809740	C	-8.685050	1.745530	6.977570
H	3.793600	1.732840	2.980310	H	-8.339050	2.065690	6.118480
H	2.616500	3.086810	2.851330	H	-8.771960	2.500750	7.596430
H	4.220410	3.369700	3.584830	H	-9.563100	1.331740	6.842390
C	6.192200	0.092570	-2.097320	C	-10.891180	-2.715770	5.853860
H	5.732850	0.112300	-3.095830	H	-11.014480	-2.355950	4.950990
H	5.843720	-0.770700	-1.513970	H	-11.765580	-2.835190	6.280340
H	7.281490	0.018190	-2.217590	H	-10.433090	-3.580780	5.801190
S	1.807710	-2.300080	-0.084810	S	5.886860	0.740190	-5.498190
S	3.132760	-0.879910	2.123430	S	8.014380	2.585060	-4.664200
S	4.434070	-3.304170	-1.234610	S	7.538590	-0.520600	-7.674330
S	5.924200	-1.651840	1.211890	S	9.901060	1.571500	-6.826410
C	-5.668160	-1.766610	-0.785200	C	-0.135420	2.035330	-0.079220
H	-5.088040	-1.843390	-1.702740	H	0.320420	2.649810	0.483460
C	-7.088750	-1.781660	-0.701060	C	-1.399400	1.460960	0.182310
H	-7.776440	-1.888150	-1.537670	H	-1.932680	1.619580	0.950740
C	-7.449490	-1.600030	0.664510	C	-1.739370	0.601260	-0.908240
H	-8.462190	-1.549390	1.059550	H	-2.540880	0.097430	-0.995020
C	-6.252040	-1.472560	1.422300	C	-0.660740	0.634130	-1.843010
H	-6.199380	-1.316770	2.497850	H	-0.614590	0.147280	-2.657380
C	-5.135320	-1.577370	0.530890	C	0.346180	1.534900	-1.336180
C	-3.708770	-1.452700	0.885270	C	1.639790	1.835160	-1.972280
C	-2.704780	-1.831990	-0.011800	C	2.153540	1.076300	-3.016430
H	-2.975390	-2.256330	-0.979740	H	1.635260	0.359930	-3.364880

Optimized molecular geometries of 5b and 5c in the neutral state and different conformations (ω B97XD/Def2-SVP)

<i>Cis-5a</i> (charge = +1, S = 2) <i>E</i> = -5760.187337 Hartree, <i>D</i> = 4.920 Debye				<i>Trans-5a</i> (charge = +1, S = 2) <i>E</i> = -5760.140430 Hartree, <i>D</i> = 0.000 Debye			
Fe	6.289930	-0.062220	0.026850	Fe	0.000000	0.000000	0.000000
S	-1.676130	2.162550	-0.135960	S	-5.940150	-0.664720	5.384480
S	-3.124220	0.640080	-2.131960	S	-7.939340	-2.754030	4.906410
S	-4.225770	3.283650	1.089410	S	-7.607790	0.738850	7.484450
S	-5.837620	1.544540	-1.131950	S	-9.874440	-1.603790	6.978790
C	5.818410	1.924260	-0.087990	C	-0.022870	-2.054880	-0.108420
H	5.316700	2.498530	0.687680	H	-0.619830	-2.611790	-0.828300
C	7.222370	1.762940	-0.205380	C	1.296750	-1.559950	-0.339810
H	7.969010	2.181930	0.465920	H	1.876800	-1.675540	-1.253900
C	7.482230	0.930610	-1.331190	C	1.696710	-0.831220	0.813550
H	8.462440	0.604030	-1.672090	H	2.636860	-0.296440	0.937720
C	6.240770	0.574270	-1.916880	C	0.624270	-0.879060	1.754770
H	6.120110	-0.062870	-2.790080	H	0.622260	-0.393060	2.728590
C	5.189590	1.195100	-1.157630	C	-0.448840	-1.654810	1.202210
C	3.753640	1.042960	-1.374900	C	-1.757800	-1.918450	1.815070
C	3.248160	0.210660	-2.392980	C	-2.195290	-1.196180	2.933440
H	3.935240	-0.326570	-3.047130	H	-1.558330	-0.427410	3.376950
C	1.889500	0.059490	-2.578100	C	-3.438430	-1.429200	3.503630
H	1.528290	-0.592380	-3.377180	H	-3.712070	-0.849420	4.383800
C	0.950720	0.733500	-1.758750	C	-4.310530	-2.407300	2.980910
C	1.463810	1.567030	-0.738040	C	-3.850100	-3.141600	1.866180
H	0.800410	2.101310	-0.059340	H	-4.487660	-3.922320	1.445580
C	2.821890	1.713930	-0.556290	C	-2.611770	-2.903500	1.294990
H	3.175310	2.362710	0.244380	H	-2.299980	-3.512090	0.443670
C	-0.437540	0.520590	-2.032890	C	-5.627550	-2.723610	3.507950
H	-0.637580	-0.166540	-2.861760	H	-6.104520	-3.594670	3.049080
C	-1.575970	1.057430	-1.464130	C	-6.355940	-2.100120	4.471930
C	-3.410580	2.242820	-0.057190	C	-7.431870	-0.573140	6.328220
C	-4.097790	1.524010	-1.008680	C	-8.349490	-1.541850	6.107900
C	-3.095150	3.263810	2.504280	C	-8.504650	1.953040	6.467460
H	-3.618940	3.811560	3.298820	H	-7.908590	2.249990	5.594520
H	-2.155450	3.787480	2.281420	H	-8.670070	2.829360	7.109090
H	-2.909290	2.233300	2.835460	H	-9.474910	1.547750	6.151100
C	-6.172070	0.126770	-2.205030	C	-10.739260	-2.974460	6.171370
H	-7.267170	0.070270	-2.260550	H	-10.909510	-2.780230	5.103630
H	-5.795570	-0.805600	-1.758880	H	-11.711660	-3.032000	6.678490
H	-5.779870	0.289300	-3.219000	H	-10.214550	-3.929180	6.314490
S	-1.833180	-2.146780	0.142150	S	5.940150	0.664720	-5.384480
S	-3.329140	-0.567680	2.117190	S	7.939340	2.754030	-4.906410
S	-4.376460	-3.342090	-1.040590	S	7.607790	-0.738850	-7.484450
S	-6.036770	-1.513920	1.101190	S	9.874440	1.603790	-6.978790
C	6.089110	-0.698520	1.967370	C	0.022870	2.054880	0.108420
H	5.972190	-0.058320	2.839040	H	0.619830	2.611790	0.828300
C	7.331450	-1.139360	1.435800	C	-1.296750	1.559950	0.339810
H	8.315810	-0.885600	1.823700	H	-1.876800	1.675540	1.253900
C	7.062110	-1.948750	0.296800	C	-1.696710	0.831220	-0.813550
H	7.804400	-2.419380	-0.344650	H	-2.636860	0.296440	-0.937720
C	5.653580	-2.004670	0.119910	C	-0.624270	0.879060	-1.754770
H	5.143030	-2.535760	-0.680640	H	-0.622260	0.393060	-2.728590
C	5.034180	-1.236080	1.161640	C	0.448840	1.654810	-1.202210
C	3.588450	-1.031250	1.353720	C	1.757800	1.918450	-1.815070
C	2.650770	-1.729450	0.581380	C	2.195290	1.196180	-2.933440
H	2.989750	-2.441780	-0.171620	H	1.558330	0.427410	-3.376950

<i>Cis-5a</i> (charge = +2, S = 1) <i>E</i> = -5759.865905 Hartree, <i>D</i> = 4.907 Debye				<i>Transs-5a</i> (charge = +2, S = 1) <i>E</i> = -5759.817874 Hartree, <i>D</i> = 0.000 Debye			
Fe	-6.182780	-0.000048	-0.000117	Fe	0.00000000	0.00000000	0.00000000
S	1.548360	-1.936450	0.243000	S	-6.05229190	-0.60355797	5.54437499
S	3.311980	-0.435940	1.992560	S	-8.04877156	-2.49990227	4.67023141
S	3.769960	-3.289340	-1.254460	S	-7.64692828	0.40110744	7.88206369
S	5.806310	-1.739400	0.851300	S	-9.97180126	-1.75718158	6.91741241
C	-6.004830	0.639480	1.943890	C	0.22786040	-2.00973104	0.33914890
H	-5.775060	1.656000	2.255770	H	-0.20010268	-2.80683929	-0.26423928
C	-7.306430	0.126560	1.724200	C	1.49498092	-1.42538832	0.13660298
H	-8.235550	0.683230	1.828910	H	2.20075674	-1.68887190	-0.64903462
C	-7.189810	-1.232290	1.312680	C	1.68623162	-0.40774898	1.12720015
H	-8.014720	-1.893340	1.054480	H	2.56172306	0.23220263	1.22109452
C	-5.816070	-1.567120	1.261860	C	0.53848092	-0.36254896	1.94480898
H	-5.418350	-2.543540	0.994870	H	0.38891023	0.31791975	2.77981748
C	-5.059680	-0.412000	1.681450	C	-0.39240846	-1.36158410	1.47152279
C	-3.613870	-0.314370	1.755250	C	-1.73346035	-1.58787447	1.96099553
C	-2.790590	-1.334710	1.222230	C	-2.24777103	-0.85023825	3.05916053
H	-3.246360	-2.202780	0.746010	H	-1.62111004	-0.10509840	3.54982778
C	-1.420330	-1.259400	1.291320	C	-3.51919375	-1.05822134	3.53566581
H	-0.845460	-2.090260	0.883480	H	-3.84813409	-0.46217523	4.38589975
C	-0.778390	-0.157020	1.911550	C	-4.37729230	-2.03162176	2.94574163
C	-1.606390	0.854360	2.461970	C	-3.85372391	-2.76655086	1.83848684
H	-1.145800	1.704910	2.970420	H	-4.48179409	-3.52361208	1.36395451
C	-2.980600	0.785400	2.372820	C	-2.58289791	-2.55554186	1.36718980
H	-3.581880	1.577570	2.819860	H	-2.22523942	-3.15199357	0.52763918
C	0.635340	-0.003220	2.036690	C	-5.69160818	-2.34394460	3.37222222
H	0.959210	0.789990	2.719870	H	-6.18923853	-3.12853794	2.79346861
C	1.672400	-0.747370	1.485090	C	-6.45944628	-1.83657205	4.41799101
C	3.245950	-2.204800	0.027200	C	-7.51816993	-0.64814879	6.47842374
C	4.082220	-1.516360	0.878640	C	-8.46373606	-1.55582435	6.07027620
C	4.021290	-4.846880	-0.341070	C	-8.73536322	1.71129467	7.23365884
H	4.779660	-4.723600	0.442240	H	-8.24928799	2.25331299	6.41284709
H	4.387310	-5.564190	-1.088110	H	-8.89625343	2.39641909	8.07699846
H	3.075190	-5.210660	0.078280	H	-9.70214492	1.29968698	6.91634215
C	6.380620	-0.560820	2.097670	C	-10.80943270	-3.02964653	5.94155781
H	6.133760	0.471890	1.810060	H	-11.00275782	-2.69305683	4.91335554
H	7.472840	-0.674990	2.111800	H	-11.77206904	-3.18304441	6.44718577
H	5.991700	-0.809590	3.095070	H	-10.25375405	-3.97786768	5.95346329
S	1.548640	1.936460	-0.243020	S	6.05229190	0.60355797	-5.54437499
S	3.312320	0.435730	-1.992380	S	8.04877156	2.49990227	-4.67023141
S	3.770240	3.289470	1.254350	S	7.64692828	-0.40110744	-7.88206369
S	5.806640	1.739350	-0.851210	S	9.97180126	1.75718158	-6.91741241
C	-5.815710	1.567230	-1.261690	C	-0.22786040	2.00973104	-0.33914890
H	-5.417950	2.543520	-0.994250	H	0.20010268	2.80683929	0.26423928
C	-7.189480	1.232550	-1.312800	C	-1.49498092	1.42538832	-0.13660298
H	-8.014360	1.893610	-1.054530	H	-2.20075674	1.68887190	0.64903462
C	-7.306160	-0.126190	-1.724660	C	-1.68623162	0.40774898	-1.12720015
H	-8.235310	-0.682750	-1.829700	H	-2.56172306	-0.23220263	-1.22109452
C	-6.004570	-0.639170	-1.944270	C	-0.53848092	0.36254896	-1.94480898
H	-5.774880	-1.655610	-2.256460	H	-0.38891023	-0.31791975	-2.77981748
C	-5.059360	0.412170	-1.681450	C	0.39240846	1.36158410	-1.47152279
C	-3.613540	0.314430	-1.755140	C	1.73346035	1.58787447	-1.96099553
C	-2.980310	-0.785570	-2.372330	C	2.24777103	0.85023825	-3.05916053
H	-3.581600	-1.577890	-2.819090	H	1.62111004	0.10509840	-3.54982778

<i>Cis-5a</i> (charge = +2, S = 3) <i>E</i> = -5759.867245 Hartree, <i>D</i> = 10.284 Debye				<i>Trans-5a</i> (charge = +2, S = 3) <i>E</i> = -5759.820183 Hartree, <i>D</i> = 0.000 Debye			
Fe	-6.291950	0.000021	-0.000008	Fe	0.000000	0.000000	0.000000
S	1.545080	-2.030230	0.325510	S	-6.170320	-0.605360	5.500550
S	3.331600	-0.460980	2.021520	S	-8.178250	-2.603710	4.810580
S	3.775750	-3.365050	-1.185760	S	-7.711770	0.497560	7.829420
S	5.824210	-1.739660	0.839240	S	-10.008270	-1.760670	7.096820
C	-5.968160	0.878840	1.836040	C	-0.024820	-2.053630	0.162260
H	-5.681650	1.920350	1.972350	H	-0.546640	-2.710120	-0.531840
C	-7.307550	0.401100	1.750040	C	1.313750	-1.586060	0.003880
H	-8.208660	1.008450	1.818840	H	1.982850	-1.825580	-0.820920
C	-7.256750	-1.004640	1.521000	C	1.601550	-0.707540	1.085590
H	-8.112120	-1.665670	1.390550	H	2.530110	-0.159710	1.237610
C	-5.886540	-1.391050	1.466670	C	0.441210	-0.634820	1.911460
H	-5.526240	-2.404320	1.297910	H	0.349020	-0.029370	2.811370
C	-5.070040	-0.230830	1.683120	C	-0.575740	-1.483410	1.358500
C	-3.602040	-0.185670	1.735350	C	-1.932960	-1.697720	1.888660
C	-2.826540	-1.227270	1.206390	C	-2.474580	-0.848040	2.864800
H	-3.305410	-2.076850	0.716650	H	-1.902130	0.005950	3.232680
C	-1.443380	-1.204200	1.290220	C	-3.742120	-1.063630	3.383580
H	-0.893500	-2.054030	0.887120	H	-4.109680	-0.364480	4.133460
C	-0.774790	-0.132150	1.911640	C	-4.530830	-2.150300	2.948910
C	-1.560440	0.910090	2.440900	C	-3.980450	-2.991430	1.957300
H	-1.073350	1.746500	2.946910	H	-4.559480	-3.845360	1.599430
C	-2.943200	0.889060	2.349240	C	-2.713660	-2.774050	1.441470
H	-3.513390	1.704360	2.797960	H	-2.322920	-3.472650	0.699600
C	0.668380	-0.037600	2.079610	C	-5.853160	-2.481300	3.445010
H	0.995650	0.742980	2.773970	H	-6.327110	-3.327240	2.937570
C	1.675210	-0.787420	1.536090	C	-6.593250	-1.930410	4.456020
C	3.255730	-2.267610	0.085510	C	-7.605860	-0.633190	6.488550
C	4.092190	-1.550860	0.899700	C	-8.544400	-1.582310	6.172560
C	4.099590	-4.888580	-0.239770	C	-8.858690	1.737260	7.144550
H	4.877360	-4.721210	0.516120	H	-8.421350	2.230840	6.267600
H	4.462100	-5.619460	-0.975160	H	-9.000740	2.475760	7.945120
H	3.178070	-5.264190	0.222060	H	-9.827630	1.284440	6.897650
C	6.400000	-0.552210	2.076810	C	-10.868780	-3.096630	6.233000
H	6.128130	0.475910	1.796680	H	-11.112360	-2.820280	5.197680
H	7.494250	-0.644800	2.068730	H	-11.804540	-3.236230	6.790280
H	6.035290	-0.809250	3.080960	H	-10.295250	-4.033400	6.269390
S	1.545110	2.030240	-0.325500	S	6.170320	0.605360	-5.500550
S	3.331620	0.460990	-2.021520	S	8.178250	2.603710	-4.810580
S	3.775820	3.365060	1.185750	S	7.711770	-0.497560	-7.829420
S	5.824260	1.739630	-0.839250	S	10.008270	1.760670	-7.096820
C	-5.886510	1.391050	-1.466720	C	0.024820	2.053630	-0.162260
H	-5.526230	2.404330	-1.297970	H	0.546640	2.710120	0.531840
C	-7.256730	1.004650	-1.521050	C	-1.313750	1.586060	-0.003880
H	-8.112090	1.665680	-1.390630	H	-1.982850	1.825580	0.820920
C	-7.307540	-0.401100	-1.750050	C	-1.601550	0.707540	-1.085590
H	-8.208640	-1.008440	-1.818870	H	-2.530110	0.159710	-1.237610
C	-5.968140	-0.878840	-1.836030	C	-0.441210	0.634820	-1.911460
H	-5.681640	-1.920360	-1.972320	H	-0.349020	0.029370	-2.811370
C	-5.070020	0.230830	-1.683140	C	0.575740	1.483410	-1.358500
C	-3.602020	0.185670	-1.735330	C	1.932960	1.697720	-1.888660
C	-2.943170	-0.889070	-2.349210	C	2.474580	0.848040	-2.864800
H	-3.513360	-1.704370	-2.797920	H	1.902130	-0.005950	-3.232680

5a (charge = +3, S = 2)				5a (charge = +3, S = 4)			
<i>E</i> = -5759.492246 Hartree, <i>D</i> = 1.919 Debye				<i>E</i> = -5759.481659 Hartree, <i>D</i> = 1.118 Debye			
Fe	-6.319970	0.006140	-0.000392	Fe	0.000011	-0.407200	-0.000095
S	1.784590	2.447160	0.041500	S	-8.598760	0.926660	0.664480
S	3.232980	0.747680	-1.857630	S	-9.900370	-0.951700	-1.139690
S	4.370060	3.589420	1.150240	S	-11.084660	2.138760	1.696010
S	5.928370	1.746660	-0.910200	S	-12.660620	-0.009520	-0.343200
C	-6.168440	1.081450	-1.797730	C	-0.930190	-1.573930	1.427010
H	-6.055550	0.638090	-2.785680	H	-1.164830	-2.632850	1.329330
C	-7.409740	1.399060	-1.195550	C	0.287600	-1.041680	1.940920
H	-8.392450	1.219110	-1.630720	H	1.144080	-1.620370	2.283230
C	-7.154070	1.935330	0.092200	C	0.200890	0.379190	1.894910
H	-7.905860	2.254610	0.813110	H	0.980480	1.080030	2.189570
C	-5.745380	1.961250	0.287360	C	-1.072130	0.723700	1.353590
H	-5.249020	2.328880	1.183450	H	-1.419960	1.737240	1.158950
C	-5.112820	1.440210	-0.894460	C	-1.794730	-0.483930	1.074310
C	-3.661970	1.301790	-1.129650	C	-3.171620	-0.589840	0.551140
C	-2.734300	1.787210	-0.195780	C	-4.078910	0.464390	0.728010
H	-3.074470	2.285260	0.712430	H	-3.766630	1.383660	1.226430
C	-1.369880	1.654660	-0.404110	C	-5.397590	0.350970	0.306480
H	-0.699860	2.030770	0.369450	H	-6.055400	1.208280	0.452620
C	-0.873180	1.024280	-1.559180	C	-5.859080	-0.826220	-0.311820
C	-1.808550	0.541280	-2.495370	C	-4.930380	-1.867990	-0.519390
H	-1.459000	0.055800	-3.409410	H	-5.252710	-2.788040	-1.011720
C	-3.171870	0.680280	-2.287720	C	-3.618400	-1.756560	-0.088060
H	-3.856340	0.300160	-3.047350	H	-2.936650	-2.593000	-0.255050
C	0.535880	0.804110	-1.850400	C	-7.228070	-1.057140	-0.751520
H	0.716740	0.142670	-2.704980	H	-7.350800	-1.912360	-1.424920
C	1.667620	1.281040	-1.262070	C	-8.391300	-0.408360	-0.428690
C	3.513020	2.551800	0.074410	C	-10.316930	1.013920	0.597360
C	4.204440	1.733780	-0.833550	C	-10.945660	0.097410	-0.254300
C	3.066580	4.543910	1.960080	C	-11.974300	3.270250	0.576660
H	2.417470	3.899560	2.568710	H	-12.773380	2.765180	0.021490
H	2.492740	5.122010	1.222330	H	-11.270220	3.769950	-0.099520
H	3.599940	5.240320	2.621390	H	-12.421540	4.013280	1.250920
C	6.293050	0.611800	-2.268310	C	-12.936530	-1.351640	-1.521000
H	5.863810	0.979480	-3.211060	H	-14.028630	-1.448000	-1.586350
H	5.953970	-0.407150	-2.032670	H	-12.518060	-2.296920	-1.147000
H	7.388250	0.615490	-2.353140	H	-12.541840	-1.098260	-2.515010
S	1.797940	-2.455380	-0.038440	S	8.598690	0.926650	-0.664390
S	3.238100	-0.742990	1.857570	S	9.900370	-0.951660	1.139810
S	4.389910	-3.577340	-1.151650	S	11.084530	2.138710	-1.696060
S	5.938190	-1.719160	0.901860	S	12.660590	-0.009530	0.343190
C	-5.733570	-2.009850	-0.260450	C	1.072210	0.723840	-1.353610
H	-5.230890	-2.398320	-1.144550	H	1.420000	1.737360	-1.158850
C	-7.139750	-1.926140	-0.104270	C	-0.200780	0.379350	-1.895020
H	-7.881030	-2.249270	-0.834310	H	-0.980360	1.080200	-2.189670
C	-7.408140	-1.324940	1.157270	C	-0.287460	-1.041520	-1.941160
H	-8.392390	-1.124380	1.578420	H	-1.143920	-1.620190	-2.283570
C	-6.158080	-1.036100	1.776870	C	0.930310	-1.573790	-1.427230
H	-6.040280	-0.577920	2.757110	H	1.164960	-2.632720	-1.329630
C	-5.105640	-1.473280	0.905030	C	1.794810	-0.483800	-1.074390
C	-3.654720	-1.339340	1.140790	C	3.171670	-0.589760	-0.551140
C	-2.725870	-1.820480	0.205740	C	4.078900	0.464590	-0.727630
H	-3.063930	-2.314830	-0.705220	H	3.766590	1.383980	-1.225810

<i>Cis-5b</i> (charge = 0, S = 1) <i>E</i> = -5760.418181 Hartree, <i>D</i> = 2.941 Debye				<i>Trans-5b</i> (charge = 0, S = 1) <i>E</i> = -5760.399219 Hartree, <i>D</i> = 1.747 Debye			
Fe	4.520210	-1.518400	-0.116520	S	-7.04112400	-1.98916400	-0.02651300
C	6.038990	-0.160850	0.155160	S	-4.72304000	-0.23422000	0.32982200
C	2.571220	-2.030270	-0.506510	S	-6.25685900	2.30299900	-0.20542000
C	6.463970	-1.465270	0.536900	S	-8.94920300	0.27493900	-0.64011300
C	4.911170	0.198860	0.957410	S	7.00406600	0.46726600	-1.58497100
C	3.401800	-3.186630	-0.522550	S	4.33948700	-0.09746900	-0.51204200
C	3.041890	-1.120120	-1.504460	S	4.93231100	-2.96789500	0.15133200
C	5.602190	-1.921720	1.576130	S	8.04272900	-2.33097700	-1.08747900
C	4.643590	-0.901510	1.833110	C	-0.85461600	-2.17811800	0.72676500
C	4.394580	-2.998770	-1.527630	C	-0.21962100	-3.21446000	0.03556300
C	4.178360	-1.725800	-2.127740	C	-0.97807300	-4.17843400	-0.62964200
C	2.441720	0.185770	-1.841660	C	-2.36531500	-4.11054100	-0.62839900
C	3.233200	1.253890	-2.277210	C	-3.03000800	-3.06444300	0.03829000
C	2.649310	2.485940	-2.551880	C	-2.25345700	-2.12611800	0.72877200
C	1.278500	2.662690	-2.406160	C	-4.49317500	-2.98909900	-0.04595800
C	0.453080	1.603220	-1.992320	H	-5.00636700	-3.92962100	-0.27000200
C	1.062720	0.371540	-1.708190	C	-5.27465000	-1.89465000	0.06250600
C	-0.983780	1.859860	-1.872260	C	-6.23894100	0.54609500	-0.13300500
C	-2.014660	0.999050	-1.737230	C	-7.30864400	-0.26303500	-0.30129100
S	-3.667380	1.620760	-1.571190	C	-4.98958600	2.61968500	-1.47055700
C	-4.479240	0.060390	-1.569090	H	-5.25952100	2.13833900	-2.41972900
C	-3.690380	-1.034930	-1.603710	H	-3.99207200	2.29365600	-1.14640300
S	-1.947960	-0.763810	-1.712640	H	-4.97728700	3.70937100	-1.60911000
S	-4.216430	-2.720270	-1.608210	C	-9.24096000	-0.51914800	-2.24862800
S	-6.236590	-0.008260	-1.620870	H	-8.55464700	-0.12219400	-3.00837800
C	-4.944740	-2.882460	0.049390	H	-10.27402400	-0.26946300	-2.52649500
C	-6.699730	1.516320	-0.754920	H	-9.14060800	-1.61076300	-2.18254600
C	4.160400	1.468030	0.898670	C	1.66102100	3.27765800	-0.00611400
C	4.802580	2.672800	0.601700	C	2.78389600	2.60876400	-0.50841500
C	4.065250	3.854170	0.531350	C	4.05526600	3.19611500	-0.51999300
C	2.694950	3.841810	0.752070	C	4.17415100	4.51967000	-0.05569600
C	2.020340	2.643510	1.056260	C	3.06577900	5.19943100	0.43222900
C	2.781310	1.470720	1.127800	C	1.81396900	4.58360600	0.46784300
C	0.570290	2.702150	1.242950	C	5.26554800	2.49139100	-0.95940300
C	-0.323910	1.734060	1.535170	C	5.48364300	1.15999400	-0.99507900
S	-2.044250	2.122650	1.705800	C	5.51180600	-1.41440300	-0.43939600
C	-2.613450	0.475550	1.926740	C	6.74397100	-1.15484300	-0.93077800
C	-1.674580	-0.494390	1.990890	C	4.50357900	-2.55011700	1.86893800
S	0.004440	0.018840	1.818460	H	4.13717000	-3.48302600	2.31865100
S	-1.981870	-2.164560	2.448040	H	3.70666500	-1.79588800	1.92019000
S	-4.357060	0.245720	2.076380	H	5.39121100	-2.20792900	2.41699800
C	-1.242000	-3.111270	1.085710	C	9.33781200	-1.54890800	-0.08071800
C	-4.537650	0.258080	3.884500	H	9.01902100	-1.46345300	0.96660700
H	6.477530	0.449810	-0.632390	H	9.61439000	-0.56117500	-0.47299200
H	1.738070	-1.842380	0.168460	H	10.20895700	-2.21539900	-0.14117000
H	7.286440	-2.024280	0.094940	H	0.55634300	1.19994700	3.76915400
H	3.310870	-4.049410	0.134520	C	0.57141900	0.48982600	2.94478700
H	5.654970	-2.888080	2.073830	C	1.63389500	0.31076400	2.01250300
H	3.844030	-0.940790	2.570940	H	-1.43077700	-0.50734700	3.11468600
H	5.190650	-3.696500	-1.780260	H	2.56524200	0.87438000	1.97771100
H	4.766590	-1.287530	-2.931810	C	1.23841200	-0.69772600	1.08731300
H	4.314820	1.128690	-2.357540	H	1.81354100	-1.04393200	0.23044300
H	3.273890	3.324910	-2.865210	C	-0.07213100	-1.14844500	1.44047300

<i>Cis-5c</i> (charge = 0, S = 1) <i>E</i> = -5760.411763 Hartree, <i>D</i> = 2.216 Debye				<i>Trans-5c</i> (charge = 0, S = 1) <i>E</i> = -5760.388375 Hartree, <i>D</i> = 0.643 Debye			
Fe	-4.002750	-0.350770	-1.586430	S	5.934570	-1.589470	-1.467700
S	1.268190	0.299640	-1.505890	S	4.823540	-0.812950	1.147210
S	1.367180	2.505680	0.443130	S	6.393480	1.744260	1.320580
S	3.870050	3.718670	-0.755540	S	7.700500	0.816530	-1.730070
S	3.797640	1.019130	-2.904060	S	-5.830220	0.058580	1.755200
S	1.716060	-3.339480	0.025860	S	-4.942080	1.202430	-0.809510
S	1.450210	-1.187730	2.012580	S	-6.201550	-0.955750	-2.479410
S	4.243780	-0.179060	1.683240	S	-7.254570	-2.272920	0.525790
S	4.620680	-2.735500	-0.554790	C	1.688700	-2.134770	0.959770
C	-3.746500	1.534310	-0.754450	C	0.720600	-2.491740	1.911560
C	-3.131510	1.459690	-2.048920	H	-0.016290	-1.743150	2.210360
H	-2.082130	1.642810	-2.266890	C	0.657580	-3.771210	2.448040
C	-4.128370	1.126450	-3.006520	H	-0.112230	-4.016910	3.182640
H	-3.962050	0.987590	-4.073000	C	1.569130	-4.739920	2.028240
C	-5.369190	0.983230	-2.323250	H	1.524720	-5.754240	2.430310
H	-6.321710	0.706650	-2.770890	C	2.543790	-4.401330	1.098420
C	-5.135100	1.228670	-0.941910	H	3.273360	-5.149950	0.779680
H	-5.883900	1.172660	-0.153730	C	2.638850	-3.104540	0.567050
C	-3.387720	-1.780940	-0.230480	C	3.732490	-2.828820	-0.394530
C	-2.563340	-1.810960	-1.406730	H	3.798460	-3.483590	-1.270250
H	-1.488150	-1.656150	-1.446670	C	4.675980	-1.881630	-0.253760
C	-3.389850	-2.067950	-2.535100	C	6.009940	0.271990	0.427080
H	-3.052780	-2.128430	-3.567910	C	6.529650	-0.088070	-0.766360
C	-4.730190	-2.205910	-2.076880	C	5.084360	2.822310	0.664300
H	-5.604540	-2.395370	-2.696330	H	4.100920	2.352600	0.802790
C	-4.731230	-2.030270	-0.666410	H	5.261580	3.028370	-0.399600
H	-5.605280	-2.078720	-0.020030	H	5.129760	3.759240	1.236170
C	-3.148170	1.939710	0.540410	C	9.194830	0.645360	-0.712770
C	-3.958100	2.625940	1.453670	H	9.071440	1.168480	0.244480
H	-4.985140	2.866890	1.172650	H	10.007370	1.114590	-1.284560
C	-3.482440	3.029280	2.698220	H	9.431990	-0.414050	-0.549370
H	-4.141360	3.566070	3.384100	C	-1.992640	2.647950	0.087410
C	-2.169320	2.743950	3.059280	C	-1.193740	3.660490	-0.467010
H	-1.786760	3.036320	4.039360	H	-0.413740	3.377400	-1.177140
C	-1.343290	2.073480	2.163110	C	-1.348020	4.993890	-0.110780
H	-0.325900	1.809950	2.461410	H	-0.706170	5.755780	-0.558320
C	-1.802230	1.677790	0.899930	C	-2.312650	5.347740	0.832530
C	-0.914240	0.978740	-0.032450	H	-2.437780	6.389860	1.133830
H	-1.377160	0.187400	-0.618990	C	-3.123470	4.362120	1.380370
C	0.377930	1.238140	-0.293020	H	-3.895030	4.634740	2.104710
C	2.686810	2.413330	-0.736050	C	-2.999910	3.012910	1.009420
C	2.647910	1.388270	-1.615020	C	-3.934110	2.039170	1.622240
C	4.664550	3.496250	0.864220	H	-3.978020	2.016710	2.716560
H	5.169390	2.522750	0.919890	C	-4.765660	1.224750	0.949420
H	3.938380	3.585280	1.683680	C	-5.900790	-0.273500	-0.880180
H	5.403950	4.303980	0.952160	C	-6.319300	-0.793120	0.293970
C	5.338310	0.773570	-1.975190	C	-4.722760	-2.004610	-2.619800
H	5.694360	1.728870	-1.568550	H	-4.718060	-2.410080	-3.640840
H	6.065400	0.391350	-2.705320	H	-4.772190	-2.827530	-1.894510
H	5.197100	0.035570	-1.173740	H	-3.816510	-1.405670	-2.455710
C	-3.008250	-1.507510	1.176950	C	-8.864260	-1.776540	-0.152060
C	-3.937940	-0.850570	1.995220	H	-8.786800	-1.590480	-1.231220
H	-4.886800	-0.533350	1.559880	H	-9.246250	-0.889150	0.369380

Optimized molecular geometries of the 1:1 inclusion complexes of 5a and g-CD (by GFN2-xTB). This caption will be on the top

Fc-inclusion complex (charge = 0, S = 1) <i>E</i> = -423.691823586856 Hartree				DTF-inclusion complex (charge = 0, S = 1) <i>E</i> = -423.680922536727 Hartree			
Fe	-6.4444	0.02257	0.09304	Fe	8.88853	4.60177	-2.28457
S	1.64679	-1.8614	0.30608	S	16.43479	0.90113	-3.57083
S	2.9496	-0.00868	2.19048	S	18.23895	3.11497	-4.30517
S	4.3211	-2.95288	-0.66963	S	18.4771	-1.2225	-4.29362
S	5.74559	-0.95524	1.42407	S	20.50751	1.21811	-5.04804
C	-6.31141	-0.95786	1.92027	C	9.92282	4.6197	-0.48436
H	-6.22432	-0.51823	2.89684	H	10.50782	5.40313	-0.03917
C	-7.51955	-1.32951	1.30143	C	8.56329	4.34551	-0.23209
H	-8.50453	-1.20035	1.71159	H	7.91166	4.90075	0.41355
C	-7.21077	-1.92733	0.05847	C	8.21422	3.17594	-0.94093
H	-7.9202	-2.31266	-0.64964	H	7.24423	2.71258	-0.95226
C	-5.81081	-1.9493	-0.08454	C	9.35891	2.71286	-1.62062
H	-5.2782	-2.36687	-0.9185	H	9.41462	1.83556	-2.2372
C	-5.23167	-1.34947	1.07126	C	10.43256	3.60171	-1.34261
C	-3.82748	-1.07178	1.28896	C	11.77751	3.55665	-1.88831
C	-2.82126	-1.72765	0.57521	C	12.43522	2.35625	-2.15512
H	-3.09072	-2.48115	-0.14855	H	11.93602	1.42127	-1.9502
C	-1.49143	-1.43722	0.78208	C	13.71898	2.34714	-2.65901
H	-0.74436	-1.96398	0.20929	H	14.20101	1.40102	-2.84836
C	-1.09809	-0.47357	1.71495	C	14.39998	3.53941	-2.92163
C	-2.1107	0.20034	2.41236	C	13.72139	4.74388	-2.67932
H	-1.83879	0.96797	3.12296	H	14.21769	5.67904	-2.89755
C	-3.43641	-0.088	2.2024	C	12.44318	4.75158	-2.17509
H	-4.19536	0.46392	2.73401	H	11.92065	5.68273	-2.01965
C	0.26821	-0.13366	2.01752	C	15.74952	3.61689	-3.42502
H	0.38592	0.63463	2.77311	H	16.11186	4.62528	-3.58908
C	1.42458	-0.62525	1.53652	C	16.63447	2.64507	-3.71247
C	3.40976	-1.82552	0.32046	C	18.04629	0.47869	-4.15308
C	4.00716	-0.98578	1.18472	C	18.86407	1.48712	-4.499
C	3.20217	-3.1529	-2.09339	C	19.45972	-1.43323	-2.76924
H	2.9659	-2.17669	-2.50453	H	18.83265	-1.22816	-1.90725
H	2.30444	-3.67282	-1.77417	H	20.3177	-0.76992	-2.80315
H	3.74864	-3.74907	-2.81638	H	19.78189	-2.46879	-2.76595
C	5.99042	0.69697	2.1415	C	20.95988	2.85408	-5.69528
H	5.46498	0.76023	3.08975	H	20.95202	3.58116	-4.8888
H	5.64502	1.45525	1.44551	H	20.26918	3.13672	-6.48348
H	7.06003	0.79251	2.29579	H	21.9633	2.74255	-6.09369
S	1.58334	2.38905	-0.26633	S	1.8722	1.40274	-4.26881
S	2.97332	0.62145	-2.17173	S	-0.30972	1.92764	-2.3509
S	4.19931	3.64826	0.66741	S	0.18252	-0.43071	-5.97302
S	5.7164	1.72818	-1.43514	S	-2.27145	0.15955	-3.85289
C	-5.84944	2.00279	0.2708	C	8.3113	4.29163	-4.21522
H	-5.33515	2.42388	1.11518	H	8.17772	3.33851	-4.69049
C	-7.24885	1.96292	0.11622	C	9.50696	5.03543	-4.21634
H	-7.96843	2.36088	0.80764	H	10.43464	4.73885	-4.67008
C	-7.53949	1.35202	-1.12467	C	9.26829	6.2487	-3.53393
H	-8.51863	1.20265	-1.54156	H	9.97848	7.04441	-3.40186
C	-6.32181	0.99966	-1.73564	C	7.92277	6.26288	-3.11969
H	-6.22319	0.5432	-2.70403	H	7.43347	7.07864	-2.62862
C	-5.25261	1.41719	-0.8857	C	7.31142	5.04533	-3.52946

C	-3.84014	1.2189	-1.13072	C	5.97732	4.59539	-3.18212
C	-2.86493	1.89444	-0.39119	C	5.61323	3.25871	-3.36584
H	-3.16809	2.58966	0.37666	H	6.34034	2.56016	-3.74694
C	-1.52316	1.69974	-0.63086	C	4.35252	2.80734	-3.04758
H	-0.80105	2.23494	-0.03411	H	4.12069	1.7602	-3.17692
C	-1.08663	0.81968	-1.62512	C	3.3981	3.67644	-2.51211
C	-2.06705	0.13333	-2.35574	C	3.78446	4.9972	-2.25565
H	-1.75731	-0.55558	-3.1295	H	3.07287	5.67361	-1.8035
C	-3.40575	0.32409	-2.11501	C	5.03989	5.45081	-2.59455
H	-4.13198	-0.23034	-2.68848	H	5.29911	6.48054	-2.40187
C	0.29296	0.57631	-1.95871	C	2.04271	3.26152	-2.21475
H	0.44764	-0.17226	-2.72762	H	1.53526	3.79416	-1.42115
C	1.42254	1.13911	-1.49287	C	1.33932	2.31513	-2.85894
C	3.3446	2.46621	-0.30954	C	0.33009	0.6093	-4.55835
C	3.98138	1.66167	-1.17899	C	-0.65616	0.81982	-3.67427
C	3.07182	3.80481	2.08998	C	-0.77343	0.67591	-7.05964
H	3.587	4.43576	2.8064	H	-1.00565	0.09981	-7.94786
H	2.1491	4.27453	1.76417	H	-1.6868	0.97298	-6.55393
H	2.88573	2.82182	2.51082	H	-0.1673	1.53885	-7.31791
C	6.04574	0.08504	-2.14036	C	-2.6951	-0.16519	-2.11577
H	5.74479	-0.68492	-1.4363	H	-1.95365	-0.83559	-1.69295
H	5.51927	-0.01427	-3.08502	H	-2.73723	0.77208	-1.56872
H	7.11802	0.04563	-2.30056	H	-3.67128	-0.63882	-2.12985
O	-10.3069	3.69574	-3.29932	O	0.91276	8.48975	-7.74298
H	-10.8472	3.90234	-2.52397	H	0.37013	8.90831	-7.05867
O	-10.2179	1.68566	-5.91495	O	0.37814	6.70228	-10.0879
H	-10.1849	2.1992	-5.08875	H	0.61199	7.15549	-9.25686
O	-9.0261	-0.92259	-5.76439	O	0.62466	3.84756	-10.0788
H	-9.96642	-0.68898	-5.75507	H	-0.1678	4.40477	-10.0636
O	-7.46026	-2.80583	-7.15698	O	1.31526	0.96878	-10.8074
H	-8.05318	-2.16467	-6.71438	H	1.14278	1.86317	-10.4606
O	-7.79372	-4.92239	-5.35073	O	1.80826	-1.05387	-8.81764
H	-8.24876	-4.70454	-6.1799	H	1.04614	-0.94384	-9.4034
O	-9.07948	-5.53175	-2.9245	O	2.7769	-3.10097	-6.83522
H	-8.73094	-5.36247	-3.81931	H	2.41745	-2.33139	-7.31396
O	-9.36043	-5.74064	-0.12254	O	2.50162	-2.86643	-4.02641
H	-10.0372	-5.52119	-0.77817	H	1.97292	-3.35235	-4.67911
O	-9.34422	-6.0597	2.79406	O	1.45006	-1.17906	-1.99064
H	-9.27489	-5.81457	1.8516	H	1.67996	-1.80337	-2.7038
O	-8.91417	-3.94165	4.6305	O	1.48273	0.67054	0.15604
H	-9.73498	-4.35673	4.32496	H	0.74308	0.50069	-0.4448
O	-8.2397	-2.50393	6.99647	O	1.63691	3.04967	1.62069
H	-8.44396	-2.92473	6.13782	H	1.66587	2.28128	1.01754
O	-8.05062	0.30538	6.68253	O	2.79474	5.52413	1.23694
H	-8.78773	-0.2456	6.98626	H	1.88107	5.19933	1.28094
O	-7.72708	3.11853	6.36593	O	3.84022	7.77101	2.46837
H	-7.82311	2.14946	6.29532	H	3.42927	6.9791	2.0619
O	-9.85319	5.66548	-1.29019	O	1.67112	10.47118	-5.82789
H	-9.34843	6.17647	-0.63289	H	2.23742	10.50544	-5.03948
O	-6.99491	5.52849	-1.60533	O	4.32284	9.60453	-5.60407
O	-8.08555	3.02143	-4.79762	O	2.95549	7.1846	-9.07959
O	-6.27738	-0.96456	-5.16703	O	3.18326	2.81555	-9.84953
O	-6.3494	-4.66703	-2.83977	O	4.04221	-0.62113	-7.20552
O	-6.98996	-5.58238	1.34068	O	4.14407	-0.86932	-2.74997
O	-6.30017	-2.99025	4.92215	O	4.04825	1.6318	0.85109
O	-5.75186	1.29615	5.38792	O	5.66465	5.67903	1.32616

C	-3.84014	1.2189	-1.13072	C	5.97732	4.59539	-3.18212
C	-2.86493	1.89444	-0.39119	C	5.61323	3.25871	-3.36584
H	-3.16809	2.58966	0.37666	H	6.34034	2.56016	-3.74694
C	-1.52316	1.69974	-0.63086	C	4.35252	2.80734	-3.04758
H	-0.80105	2.23494	-0.03411	H	4.12069	1.7602	-3.17692
C	-1.08663	0.81968	-1.62512	C	3.3981	3.67644	-2.51211
C	-2.06705	0.13333	-2.35574	C	3.78446	4.9972	-2.25565
H	-1.75731	-0.55558	-3.1295	H	3.07287	5.67361	-1.8035
C	-3.40575	0.32409	-2.11501	C	5.03989	5.45081	-2.59455
H	-4.13198	-0.23034	-2.68848	H	5.29911	6.48054	-2.40187
C	0.29296	0.57631	-1.95871	C	2.04271	3.26152	-2.21475
H	0.44764	-0.17226	-2.72762	H	1.53526	3.79416	-1.42115
C	1.42254	1.13911	-1.49287	C	1.33932	2.31513	-2.85894
C	3.3446	2.46621	-0.30954	C	0.33009	0.6093	-4.55835
C	3.98138	1.66167	-1.17899	C	-0.65616	0.81982	-3.67427
C	3.07182	3.80481	2.08998	C	-0.77343	0.67591	-7.05964
H	3.587	4.43576	2.8064	H	-1.00565	0.09981	-7.94786
H	2.1491	4.27453	1.76417	H	-1.6868	0.97298	-6.55393
H	2.88573	2.82182	2.51082	H	-0.1673	1.53885	-7.31791
C	6.04574	0.08504	-2.14036	C	-2.6951	-0.16519	-2.11577
H	5.74479	-0.68492	-1.4363	H	-1.95365	-0.83559	-1.69295
H	5.51927	-0.01427	-3.08502	H	-2.73723	0.77208	-1.56872
H	7.11802	0.04563	-2.30056	H	-3.67128	-0.63882	-2.12985
O	-10.3069	3.69574	-3.29932	O	0.91276	8.48975	-7.74298
H	-10.8472	3.90234	-2.52397	H	0.37013	8.90831	-7.05867
O	-10.2179	1.68566	-5.91495	O	0.37814	6.70228	-10.0879
H	-10.1849	2.1992	-5.08875	H	0.61199	7.15549	-9.25686
O	-9.0261	-0.92259	-5.76439	O	0.62466	3.84756	-10.0788
H	-9.96642	-0.68898	-5.75507	H	-0.1678	4.40477	-10.0636
O	-7.46026	-2.80583	-7.15698	O	1.31526	0.96878	-10.8074
H	-8.05318	-2.16467	-6.71438	H	1.14278	1.86317	-10.4606
O	-7.79372	-4.92239	-5.35073	O	1.80826	-1.05387	-8.81764
H	-8.24876	-4.70454	-6.1799	H	1.04614	-0.94384	-9.4034
O	-9.07948	-5.53175	-2.9245	O	2.7769	-3.10097	-6.83522
H	-8.73094	-5.36247	-3.81931	H	2.41745	-2.33139	-7.31396
O	-9.36043	-5.74064	-0.12254	O	2.50162	-2.86643	-4.02641
H	-10.0372	-5.52119	-0.77817	H	1.97292	-3.35235	-4.67911
O	-9.34422	-6.0597	2.79406	O	1.45006	-1.17906	-1.99064
H	-9.27489	-5.81457	1.8516	H	1.67996	-1.80337	-2.7038
O	-8.91417	-3.94165	4.6305	O	1.48273	0.67054	0.15604
H	-9.73498	-4.35673	4.32496	H	0.74308	0.50069	-0.4448
O	-8.2397	-2.50393	6.99647	O	1.63691	3.04967	1.62069
H	-8.44396	-2.92473	6.13782	H	1.66587	2.28128	1.01754
O	-8.05062	0.30538	6.68253	O	2.79474	5.52413	1.23694
H	-8.78773	-0.2456	6.98626	H	1.88107	5.19933	1.28094
O	-7.72708	3.11853	6.36593	O	3.84022	7.77101	2.46837
H	-7.82311	2.14946	6.29532	H	3.42927	6.9791	2.0619
O	-9.85319	5.66548	-1.29019	O	1.67112	10.47118	-5.82789
H	-9.34843	6.17647	-0.63289	H	2.23742	10.50544	-5.03948
O	-6.99491	5.52849	-1.60533	O	4.32284	9.60453	-5.60407
O	-8.08555	3.02143	-4.79762	O	2.95549	7.1846	-9.07959
O	-6.27738	-0.96456	-5.16703	O	3.18326	2.81555	-9.84953
O	-6.3494	-4.66703	-2.83977	O	4.04221	-0.62113	-7.20552
O	-6.98996	-5.58238	1.34068	O	4.14407	-0.86932	-2.74997
O	-6.30017	-2.99025	4.92215	O	4.04825	1.6318	0.85109
O	-5.75186	1.29615	5.38792	O	5.66465	5.67903	1.32616

C	-8.09791	-6.17723	-2.15694	C	3.84785	-2.69025	-6.03447
H	-8.32117	-7.25579	-2.09523	H	4.40011	-3.59878	-5.76395
C	-6.67768	-6.0295	-2.72923	C	4.79265	-1.72238	-6.77469
H	-6.62421	-6.52081	-3.70939	H	5.26297	-2.2326	-7.62567
C	-4.08819	-4.91679	4.39598	C	6.13898	-0.54291	1.00975
H	-3.34414	-5.38922	3.74394	H	6.99213	-1.05812	0.5556
H	-3.77921	-3.88736	4.61993	H	6.45069	0.44762	1.36721
C	-5.41804	-4.86115	3.63931	C	5.07556	-0.34675	-0.07447
H	-5.31825	-4.17736	2.78405	H	5.45719	0.34787	-0.83701
C	-6.53951	-4.33332	4.55189	C	3.80303	0.2732	0.52765
H	-6.59066	-4.97221	5.44211	H	3.51774	-0.29641	1.41924
C	-7.87328	-4.41493	3.80592	C	2.65882	0.2264	-0.48639
H	-7.81227	-3.80183	2.89441	H	2.90895	0.89575	-1.31941
C	-8.10378	-5.88231	3.41762	C	2.48429	-1.18845	-1.03841
H	-8.12054	-6.49466	4.32755	H	2.22515	-1.86633	-0.20789
C	-6.92774	-6.32894	2.52731	C	3.82733	-1.65343	-1.62448
H	-7.00406	-7.40352	2.31468	H	3.75008	-2.71156	-1.90568
C	-3.22606	-0.24185	5.99742	C	6.96975	3.696	3.16868
H	-2.47281	-0.97108	5.67828	H	7.41222	2.72218	3.39978
H	-3.11056	0.6833	5.41818	H	7.7029	4.31025	2.63091
C	-4.608	-0.82612	5.69175	C	5.76884	3.44826	2.24884
H	-4.71273	-0.94448	4.605	H	6.13159	3.15516	1.25409
C	-5.70977	0.12727	6.19169	C	4.92923	4.73256	2.08031
H	-5.49397	0.38942	7.23433	H	4.6918	5.13011	3.07339
C	-7.07818	-0.5559	6.1368	C	3.62818	4.38971	1.35033
H	-7.32997	-0.78698	5.091	H	3.86955	4.01648	0.3449
C	-6.99509	-1.87033	6.92242	C	2.91192	3.29085	2.14771
H	-6.6907	-1.65919	7.95441	H	2.77356	3.63709	3.18152
C	-5.91159	-2.73606	6.25025	C	3.83271	2.05991	2.17088
H	-5.77999	-3.67438	6.80458	H	3.38351	1.25943	2.77401
C	-2.85848	3.97766	3.72565	C	8.7453	8.06455	-0.21224
H	-2.08841	3.29644	4.10374	H	9.42445	7.37819	0.29871
H	-2.78219	4.04797	2.63204	H	8.90555	7.99157	-1.29337
C	-4.22407	3.37972	4.07754	C	7.32301	7.59579	0.11373
H	-4.39241	2.48761	3.45807	H	7.0987	6.70442	-0.4863
C	-5.35497	4.3859	3.78934	C	6.27572	8.67856	-0.21765
H	-5.14593	5.3086	4.34231	H	6.58958	9.62653	0.23242
C	-6.67747	3.80109	4.28894	C	4.91393	8.28176	0.35911
C	-6.51937	3.52813	5.79299	C	5.07673	7.99896	1.85583
H	-6.23792	4.46521	6.29119	H	5.50429	8.87868	2.35241
C	-5.37535	2.51447	5.97919	C	6.09183	6.84353	2.00222
H	-5.17011	2.37665	7.04918	H	6.26055	6.62648	3.06598
C	-6.49276	5.52141	-5.77945	C	5.4099	8.86824	-9.68907
H	-5.73326	6.30028	-5.65133	H	6.42119	9.20822	-9.43825
H	-6.03112	4.61733	-6.19591	H	5.45002	7.84086	-10.073
C	-7.04668	5.19768	-4.38679	C	4.57816	8.87147	-8.40338
H	-6.3058	4.60063	-3.83456	H	4.96373	8.10219	-7.71928
C	-8.34444	4.37184	-4.46105	C	3.10436	8.5383	-8.69244
H	-9.01812	4.8291	-5.19649	H	2.73758	9.20579	-9.48161
C	-9.05552	4.31426	-3.10677	C	2.26032	8.75175	-7.43291
H	-8.44215	3.71855	-2.41454	H	2.60627	8.06362	-6.64729
C	-9.19636	5.72662	-2.52989	C	2.45831	10.19771	-6.95542
H	-9.78694	6.34369	-3.22658	H	2.14275	10.87708	-7.75957
C	-7.78559	6.33001	-2.44283	C	3.9521	10.41615	-6.68379
H	-7.84105	7.35989	-2.06756	H	4.12737	11.47672	-6.45412
H	-6.88007	2.85638	3.76295	H	4.56577	7.36367	-0.13724

O	-7.73135	4.70626	4.05504	O	3.97737	9.31625	0.14218
H	-8.41558	4.52413	4.71831	H	3.3274	9.27109	0.861
C	-6.23073	6.19538	-0.61598	C	5.268	10.1548	-4.69613
C	-6.14767	6.89505	1.77731	C	5.61595	11.06617	-2.40989
O	-4.24738	5.77101	0.79194	O	7.28573	9.6493	-3.43377
C	-4.97354	5.9112	1.96984	C	6.69705	9.97662	-2.21254
C	-4.98888	5.33262	-0.34065	C	6.38812	9.14327	-4.41668
C	-7.04864	6.33853	0.67242	C	4.56698	10.51316	-3.38215
H	-5.73459	7.86069	1.4621	H	6.10024	11.94318	-2.85674
H	-5.33638	4.30233	-0.18972	H	5.92748	8.2178	-4.05009
H	-7.4006	5.33988	0.9743	H	4.12889	9.60213	-2.94559
H	-5.91849	7.18517	-0.96987	H	5.70789	11.06969	-5.11259
H	-4.26598	6.32092	2.70283	H	7.50917	10.36821	-1.58655
O	-8.16037	7.18465	0.4497	O	3.54802	11.45085	-3.64908
H	-8.4089	7.55827	1.31009	H	3.37948	11.93905	-2.82926
O	-6.87173	7.14281	2.94942	O	5.0324	11.51129	-1.21983
H	-7.19222	6.29204	3.31476	H	4.64214	10.74724	-0.74695
C	-4.02563	5.3566	-1.52962	C	7.21588	8.80711	-5.67513
H	-3.14695	4.76175	-1.25914	H	8.20039	8.48034	-5.33531
H	-4.53108	4.88605	-2.38339	H	6.72508	7.9765	-6.1959
O	-3.6692	6.68488	-1.83256	O	7.43854	9.881	-6.5482
H	-2.86504	6.68194	-2.36402	H	6.61009	10.1041	-7.00316
O	-5.44201	4.64881	2.40168	O	6.14797	8.81494	-1.62546